# Modeling and evaluating the thermal conductivity of porous thermal barrier coatings at elevated temperatures for industrial applications

By

**Moteb Alotaibi**

Thesis submitted to the Faculty of Graduate and Postdoctoral Studies in partial fulfilment of the requirements for the degree of

**M.Sc. in Physics**

Ottawa Carleton Institute of Physics

Department of Physics

University of Ottawa

Ottawa, Canada

**Supervisor: Dr. Chen Kuiyng**

# Abstract

The thermal conductivity of various porous thermal barrier coating (TBC) systems used in elevated temperature for industrial applications has been evaluated using a proposed six-phase model. These porous TBC systems rely on microstructural properties and yield different types of porosity. These microstructural properties can influence the thermal conductivity of TBC systems. The purpose of this thesis is to assess the thermal conductivity of TBC systems based on microstructural attributes, particularly the effect of different types of porosity. Thus, the first component of this thesis investigates the microstructural characterization of various TBC systems using image analysis (IA) technique. In this technique, scanning electron microscopy (SEM) and light optical microscopy (LOM) micrographs were used to measure the porosity level of different TBC materials. The volumetric fraction of porosity along with orientation, shape, and morphology have a considerable impact on the total thermal conductivity of TBCs.

The second component of this thesis evaluates the thermal conductivity of these porous TBC systems by taking into account the effect of the heat treatment process. The IA results reveal that as long as the porosity content increases, the thermal conductivity decreases for all of the TBC materials studied in this thesis. Further, while the content of microcracks and non-flat porosity play a crucial role in reducing the thermal conductivity of TBC materials, the other types of porosity (open randomly oriented, penny-shaped, and interlamellar) exert less impact on the thermal conductivity of TBCs. Comparing the results of the proposed six-phase model to experimental values and finite element analysis (FEA) values showed a relatively good agreement.

The proposed six-phase model can predict the thermal conductivity of porous microstructure of TBC systems close to real measured values; therefore, the proposed six-phase model may be utilized to fabricate the porous microstructure of TBCs.

# Acknowledgment

First of all, I thank God Almighty for giving me the strength, patience, ability, and blessing to finalize this thesis work at a university, one of the best universities worldwide. Without His mercies, it would not have been possible for me to successfully complete this thesis work.

To my kind father, Alotaibi Qahess, I greatly appreciate your endless support and advice. I have learned so much from you. Without you, my studies and my life would not be as wonderful as it is now. I am very proud to be your son.

To my beloved mother, Alotaibi Shaba, you are the light of my life and everything to me. I am very grateful for your honest prayers that positively reflect upon my life. Words cannot express my feelings towards you! You are an amazing, lovely, and kind mother.

To my supervisor, Dr. Chen Kuiying, many thanks for your endless help, guidance, and patience. Thanks for being my supervisor and for giving me this great opportunity. Without your support, my thesis work would not be finished. I very much appreciate the academic advice and ideas you have generously provided. I am super lucky to have a supervisor who continuously guides me when I deviate from the path.

I dedicate this thesis work to my brothers and sisters, especially to my elder brother, Khalid, who just passed away a couple of months ago. You always called me ‘doctor.’

Special thanks to my lovely wife, Alosaimi Rehab, who stands beside me and who has always encouraged me during my academic journey. I love you more than you imagine, sweetheart. To my little boy, Abdulrahman, you were born when your father started this study. You are such an adorable honey boy who makes my life very sweet.

To Dr. Alosaimi Mishary, Dean of the Preparatory Year at Prince Sttam bin Abdulaziz University, thank you very much for your advice and support during my study. Everything you have done for me is highly appreciated.

To my best friend, Alotaibi Abdulrahman, you are not just a friend; you are my brother! I will never ever forget your first invitation for dinner. I am more than proud to have you in my life.

I am grateful to all of my friends in Canada, Saudi Arabia, and The United Kingdom for their encouragement and support. Warm thanks to my closest friends at University of Ottawa Abo Baker, Mohammad Asiri, Aldaeefi N. Fahad, Guri, Ratan, and Tej for always standing beside me and bringing joy to my life in Canada.

To Professor Bela Joos, course director of the Physics Department, I would like to thank you for your guidance and your nice chats regarding the requirements for obtaining the degree. You are a kind person who looks after his students while making sure that everything is on the right track.

I would like to thank the Saudi Arabian Cultural Bureau in Canada for supporting me financially throughout the duration of my studies.

# Table of Contents

**Abstract** ..... **i**
**Acknowledgment** ..... **ii**
**Table of Contents** ..... **iv**
**List of Figures** ..... **vi**
**List of Tables** ..... **viii**
**List of Abbreviations** ..... **ix**
**Chapter 1 Introduction to Thermal Barrier Coatings** ..... **1**
**Chapter 2 Literature Review of Thermal Barrier Coatings** ..... **6**
2.1 Thermal barrier coatings (TBCs) ..... 6
2.2 Coating deposition methods of TBCs ..... 10
2.2.1 Electron beam physical vapour deposition (EB-PVD) ..... 10
2.2.2 Atmospheric plasma spray (APS) ..... 14
2.3 Thermal conductivity of coatings ..... 17
2.4 Techniques for calculating thermal conductivity ..... 19
2.5 Mechanisms of heat transfer ..... 21
2.6 Impact of different parameters on thermal conductivity of TBCs ..... 26
2.6.1 Thermal conductivity affected by yttria content ..... 26
2.6.2 The thermal conductivity of coatings affected by impurities ..... 27
2.6.3 Effect of layering on EB-PVD TBCs ..... 29
2.6.4 Thermal conductivity affected by interface ..... 31
**Chapter 3 Numerical and Analytical Models for Thermal Conductivity** ..... **33**
3.1 Numerical Models ..... 34
3.2 Analytical Models ..... 35
**Chapter 4 Six-phase Model for Evaluating Thermal Conductivity of TBCs** ..... **40**
4.1 Determining different parameters used in the model ..... 52
**Chapter 5 TBCs' Microstructural Characterization and Thermal Conductivity** ..... **57**
5.1 Principle of image analysis method ..... 58
5.2 Results and discussions ..... 59
5.2.1 Microstructural investigation and porosity analysis ..... 59
5.2.1.1 Image analysis procedure and results ..... 60

5.2.2 Thermal conductivity evaluations and heat treatment effect.....79
**Chapter 6 Conclusion.....89**
**References.....91**
**Appendix.....101**

# List of Figures

Fig. 1 Progress in elevated temperature super-alloys and cooling technology for fifty years [6]. . 2
Fig. 2 Cross-sectional image of scanning electron microscopy (SEM) of EB-PVD TBC representing the four-layer [15]. ..... 3

Fig. 2- 1 Typical structure of an EB-PVD TBC [27]..... 7
Fig. 2- 2 Schematic representation of the temperature distribution of TBC's layers. ..... 8
Fig. 2- 3 Aluminum's outward and Oxygen's inward diffusion from bond coat [35]..... 10
Fig. 2- 4 Micrograph of scanning electron microscopy of TBC applied by EB-PVD [41]. ..... 12
Fig. 2- 5 Schematic representation of coating prepared by EB-PVD. ..... 13
Fig. 2- 6 Schematic representation of the procedure of EB-PVD [38]. ..... 14
Fig. 2- 7 Schematic representation of the APS process [46]. ..... 15
Fig. 2- 8 Schematic representation of splat of APS. ..... 16
Fig. 2- 9 SEM micrograph of APS morphology [39]. ..... 16
Fig. 2- 10 Comparison of thermal conductivity of bulk, EB-PVD and APS [53]. ..... 19
Fig. 2- 11 Thermal conductivity of YSZ as a function of temperature [60]. ..... 22
Fig. 2- 12 Schematic illustration of the mechanisms of heat transfer of APS-TBCs [64]..... 23
Fig. 2- 13 Impact of different yttria content on thermal conductivity of YSZ ceramics [70]. ..... 27
Fig. 2- 14 Schematic diagram of (a) pure crystal lattice (b) lattice with defect (anion) (c) lattice with defect (cation) [74]..... 28
Fig. 2- 15 Phase diagram of $ZrO2$ representing the effect of yttria on different phases of zirconia (Tetragonal, T, cubic, F and monoclinic, m) [75]..... 29
Fig. 2- 16 Schematic representation of EB-PVD TBC [79]. ..... 30
Fig. 2- 17 The effect of interfacial thermal resistance [52]. ..... 32

Fig. 4- 1 Representation of spheroidal shape used in modelling defects. ..... 45
Fig. 4- 2 Shape factor (F) values corresponding to aspect ratio a/c [102]. ..... 46
Fig. 4- 3 Relationship between X factor and aspect ratio for various shapes [102]. ..... 47
Fig. 4- 4 Flowchart representing the procedure for determining total thermal conductivity of TBCs. ..... 48
Fig. 4- 5 Representation of the angle of revolution. ..... 52

Fig. 5- 1 The menu of (Fiji Is Just) ImageJ software. ..... 58
Fig. 5- 2 SEM micrographs of $SrZrO3$ coating after heat treatment at 1400 °C for different times: (a) 0 h, (b) 5 h, (c) 10 h, (d) 20 h, (e) 100 h, (f) 230 h, and (g) 360 h [103]. ..... 61
Fig. 5- 3 Sample of (IA) process for segmenting microstructure of defects..... 62
Fig. 5- 4 Porosity of $SrZrO3$ for different times after heat treatment at 1400 °C performed by (IA)..... 63
Fig. 5- 5 Optical images of different as-sprayed coating materials: (a) 8YPSZ, (b) 25CSZ and (c) 22MSZ [104]..... 65
Fig. 5- 6 Sample of (IA) process for segmenting microstructure of defects..... 66
Fig. 5- 7 Porosity measurements of different as-sprayed coating materials performed by (IA). . 67
Fig. 5- 8 Classification of porosities present in coating materials. ..... 69

Fig. 5- 9 SEM images of various as-sprayed powder coating materials and annealed at 1200 °C for 225 h [67]. ..... 70
Fig. 5- 10 Sample of (IA) process for segmenting microstructure of defects..... 71
Fig. 5- 11 Porosity measurements of various as sprayed and annealed powder coating materials performed by (IA). ..... 72
Fig. 5- 12 Classification of porosities present in various powder coating materials. ..... 74
Fig. 5- 13 SEM micrographs of agglomerated and sintered powder annealed at 1250 °C for different times: (a) 0h, (b) 5h, (c) 15h, (d) 50h and (e) 200h [105]. ..... 75
Fig. 5- 14 Sample of (IA) process for segmenting microstruure of defects. ..... 76
Fig. 5- 15 Porosity measurements of agglomerated and sintered powder coating material annealed at 1250 °C for different times performed by (IA)..... 77
Fig. 5- 16 Classification of porosities present in agglomerated and sintered powder coatings material annealed at 1250 °C for different times performed by (IA). ..... 79
Fig. 5- 17 Comparison of predicted and experimental thermal conductivity of $SrZrO3$ coating. 81
Fig. 5- 18 Comparison of calculated six-phase model and measured thermal conductivity of different coating materials. ..... 83
Fig. 5- 19 Comparison of simulated six-phase, FEA models, and experimental thermal conductivity of various powder coating materials. ..... 85
Fig. 5- 20 Comparison of computed six-phase model and measured thermal conductivity of agglomerated and sintered powder coating material annealed at 1250 °C for different times. .... 87

# List of Tables

Table 2- 1 Comparison of properties of EB-PVD and APS coating..... 17

Table 4- 1 Nomenclature of the six-phase model. ..... 49
Table 4- 2 Different equations for different functions in terms of X factor used in modeling..... 54
Table 4- 3 Values of different aspect ratio, shape factor (F) and X factor for each defect shape used in modelling. ..... 55

Table 5- 1 Porosity content of $SrZrO3$ coating sample annealed at 1400 °C for different times performed by (IA). ..... 64
Table 5- 2 Porosity measurements and its components of as-sprayed 8YPSZ, 22MSZ and 25CSZ coating samples performed by (IA). ..... 68
Table 5- 3 Porosity evaluations of the three as-sprayed and annealed powder coating materials performed by (IA). ..... 73
Table 5- 4 Porosity measurements of agglomerated and sintered powder coating material annealed at 1250 °C performed by (IA). ..... 78
Table 5- 5 Comparison between experimental and predicted thermal conductivity values of $SrZrO3$ sample (bulk value = 2.08 [W/m K]). ..... 80
Table 5- 6 Thermal conductivity differences between predicted and experimental values. ..... 82
Table 5- 7 Comparison between the experimental and calculated thermal conductivity of three different as-sprayed coating samples 8YPSZ, 22MSZ and 25CSZ (bulk value of 8YPSZ and 25CSZ=2.8 [W/m K] and bulk value of 22MSZ=2.2 [W/m K]). ..... 82
Table 5- 8 Thermal conductivity difference between calculated six-phase model and experimental values. ..... 84
Table 5- 9 Comparison between experimental, calculated six-phase, and FEA model thermal conductivity values (bulk value = 2.5 [W/m K]). ..... 84
Table 5- 10 Thermal conductivity difference between calculated six-phase model, FEA model, and experimental values. ..... 86
Table 5- 11 Comparison between the experimental and computed thermal conductivity of agglomerated and sintered sample annealed at 1250 °C for different times..... 86
Table 5- 12 Thermal conductivity differences between the computed six-phase model and experimental values. ..... 88

# List of Abbreviations

| Abbreviation | Definition |
|---|---|
| APS | Atmospheric plasma spray |
| BC | Bond coat |
| CSZ | Ceria-stabilized zirconia |
| EB-PVD | Electron beam-physical deposition |
| FEM | Finite element method |
| FEA | Finite element analysis |
| IA | Image analysis |
| LOM | Light optical microscopy |
| LFA | Laser flash analysis |
| MIP | Mercury intrusion porosimetry |
| MSZ | Magnesia-stabilized zirconia |
| NIH | National institute of health |
| SANA | Small angle neutron scattering |
| SEM | Scanning electron microscopy |
| TBC | Thermal barrier coating |
| TC | Topcoat |
| TGO | Thermally grown oxide |
| YPSZ | Yttria partially-stabilized zirconia |
| YSZ | Yttria-stabilized zirconia |

# Chapter 1 Introduction to Thermal Barrier Coatings

The standard design and production of the modern-day turbine engine are the results of improvements made to the high-temperature alloys used in engineering. According to the laws of thermodynamics, increasing the inlet operating temperature will optimize the efficiency and performance of an engine [1]. Thus, improving the efficiency and power of the system makes it environmentally friendly and economical.

Turbine engine constituents are exposed to a corrosive and oxidative gaseous environment, as well as high temperatures. In some situations, during operation high-velocity foreign particles have a considerable impact on turbine engine components [2]. Thus, a base alloy or metal needs to have properties such as proper stress relaxation, high-temperature strength, excellent resistance to oxidation and hot corrosion in order to operate for longer time [3]. In most cases, super-alloys work very well as a substrate material [4]. With the number of design specifications always on the rise, as well as the continued advancements in technology, it should not be long before these super-alloys reach their theoretical design limit.

From the mid-1900s onwards there were little improvements made to engine design. However, this is largely due to the remarkable improvements made previously, as well as the standard of engine produced [5]. The developmental stages and evolution of super-alloys from 1965 to 2015 are demonstrated below in Figure 1. It is clear that since 2008, that progress has been relatively stable. Due to the advancements in cooling technologies and high-temperature capability, these super-alloys are now able to withstand higher temperatures than previously [6].

To further improve efficiency and design, turbine engines now use ceramic coated components [7]. These components, also known as Thermal Barrier Coatings (TBCs), are designed

for use at high temperatures. TBCs serve as protection for the base metals and super-alloy components by preventing them from experiencing high-temperature degradation [8]. They also increase the efficiency and lifetime of the component, as well as providing creep resistance, thermal shock resistance, strain tolerance, stability to the substrate at higher temperatures, and protection against hot corrosion [9].

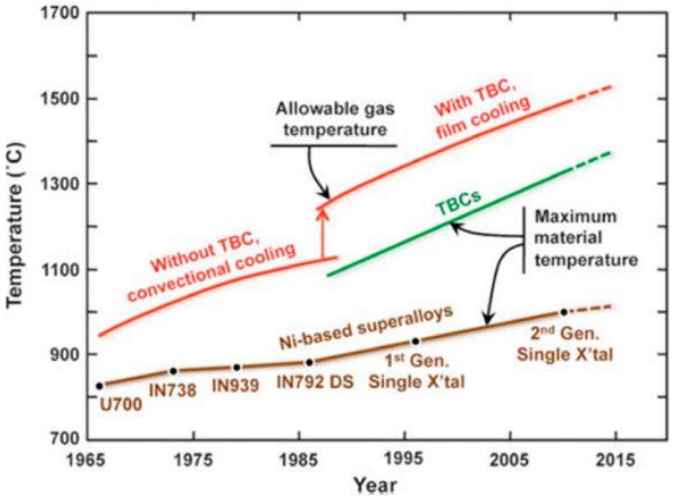


Fig. 1 Progress in elevated temperature super-alloys and cooling technology for fifty years [6].

TBCs improve efficiency and increase the operational lifetime of turbine engines; consequently, TBCs are now a major part of gas turbine engines [10]. A typical TBCs' system is comprised of four main layers: topcoat (TC); bond coat (BC); thermally grown oxide (TGO) (usually $\alpha - Al_2O_3$) that is created between the surface of the bond coat and topcoat. These desired layers are being designed to provide good thermal insulation and long-life for the material [11].

Reducing the temperature of the metal is one objective of the top ceramic coating. The functions of the metallic bond coat are to optimize the bonding between the underlying super-alloy and the topcoat, and protect the super-alloy from hot corrosion and oxidation [12]. A state-of-the-

art TBC, yttria-stabilized zirconia [YSZ], is composed of 6-8% $Y_2O_3$ [8]. The bond coat is made up of $MCrAlY$, where $M = Ni, Co$ or $NiCo$, [13].

The major properties of YSZ TBC include phase compatibility with alpha alumina, high melting point, low thermal conductivity, corrosion resistance, and protection from the negative effect of large particle impacts [14]. A summary of the use of these TBCs in high-pressure turbine aero engines is provided in Figure 2 below.

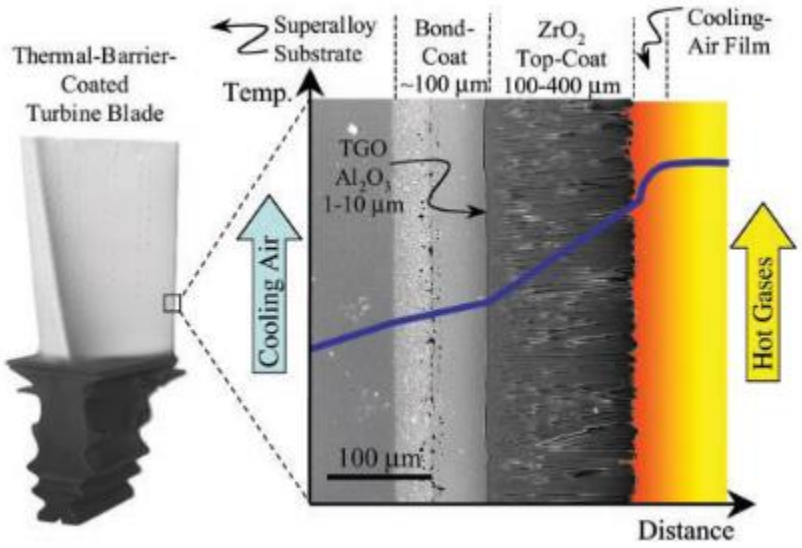


Fig. 2 Cross-sectional image of scanning electron microscopy (SEM) of EB-PVD TBC representing the four-layer [15].

The ceramic coatings' microscopic structure is very inhomogeneous, containing defects such as voids, pores, and vacancies, as well as cracks of various sizes and shapes. Generally, the presence of imperfections [16] and spraying parameters [17] influences the thermal conductivity of the coating. The degree of change in the mechanical-thermal properties is dependent on the size, amount, and morphology of the defects which are present in the coating.

The coating's mechanical and thermal properties dictate how long it will last, which is why the service life of the coated part highly depends on the density of the defects noticed. Defects reduce the thermal conductivity of the material. The implication is that the service life becomes

longer, as there is a reduction of the heat transfer to the substrate. Lower heat transfer to the substrate means that any damage to the coating interface, where many of the failures take place, will be minimal [12].

To attain superior strain tolerance, lower values for thermal conductivity, and longer lifespan, there must be an optimized distribution of pores and cracks in the coating [18]. Hence, it is crucial to understand the basic microscopic structural properties of the TBC to manufacture an optimized coating.

The TBCs' metallic-ceramic multi-layer is deposited using several techniques. For example, Electron-Beam Physical Vapour Deposition (EB-PVD) and Air Plasma Spray (APS) are the techniques most likely techniques used in depositing TBCs. These techniques are preferred as they produce material with low thermal conductivity. The former technique has a higher thermal compared to the latter. TBCs prepared by APS has the characteristic of a lamellar film structure, whereas TBCs fabricated by EB-PVD exhibit columnar defects [19].

There have been intensive models used for calculating the thermal conductivity of porous composites. In particular, in the late $19^{th}$ century, the pioneering analytical model by Maxwell was the first calculation expressed for determining the effective thermal conductivity of a heterogeneous system. However, Maxwell's model was limited by a higher volume of defects present in the porous materials.

In this study, Bruggeman's two-phase model was used as a reference to measure the thermal conductivity of heterogeneous mediums. It is widely believed that this model is well-suited to provide a better estimation of thermal properties of the porous materials as it can be used to

cover a wide range of defects. This model, along with other similar models, will be briefly discussed in Chapter 3.

The morphology of porosity was also investigated in this thesis, in relation to the estimation of the thermal conductivity of porous TBCs. This investigation of porosity was performed by the quantitative study of the pores' morphology via image analysis software (i.e. [Fiji Is Just] ImageJ). Additionally, in this thesis, a modified analytical model (i.e. six-phase model) was proposed for the prediction of the overall thermal conductivity of porous TBCs; with the contribution of more types of porosity with different shapes and orientation. This model will be discussed in detail in Chapter 4. The results of this proposed model were then compared to existing measured results and a previous finite element analysis (FEA) model in an attempt to validate the results calculated using the six-phase model. The details of these comparisons will be presented in Chapter 5. The work in this thesis will be submitted to a journal for publications.

# Chapter 2 Literature Review of Thermal Barrier Coatings

## 2.1 Thermal barrier coatings (TBCs)

TBCs are made up of different materials and are designed to minimize the transfer of heat from hot gases to the metallic substrate. The structure of the TBCs comprises a ceramic topcoat layer that provides insulation, as well as a layer of an intermediate bond coat on top of the substrate of a super-alloy. A single-crystal superalloy substrate is a great choice for optimizing ductility, high-temperature strength, hot-corrosion and oxidation resistance, as it contains the Ni-base element [20].

Vanes and blades are made to go through high stresses and high centrifugal loads. Thus, it is essential for the superalloy utilized for these to be creep resistant [21]. Vanes or blades are usually made of superalloys that have a high percentage of nickel. These super-alloys have the properties needed in the material. Cool air is used to cool these structures internally using internal serpentine cooling passages [22]. When the cool air passes through the small holes, a thin air film is formed on the surface of the blade.

The components of the gas turbine are protected from harsh thermal environments by the TBC; consequently, this boosts its efficiency and reduces undesired emissions. The temperatures of the turbine entry gas can ascend to over 1500 °C. However, the use of TBCs can reduce the temperature by 200-300°C across the coating's thickness [23]. The equation below represents the efficiency (ε) of a TBC [24]:

$$\varepsilon = \frac{T_2 - T_1}{T_2} \tag{2.1}$$

where $T_1$ and $T_2$ are the sink temperature and the operating temperature, respectively. As a result, increasing $T_2$ (turbine entrance temperature) will increase efficiency.

TBCs have low thermal conductivity, which helps to reduce heat transfer to the super-alloy substrate of the turbine blade from the hot combustion gases [25]. When TBCs are combined with the blade's internal cooling system, the gas turbine engine can function at a higher temperature than the temperature at which would cause some super-alloys to melt [1]. The challenge becomes evident with the higher ceramic layer as when the surface temperature of the ceramic layer gets high, it is hard to put in check the sintering resistance and the high-temperature phase stability [26].

Figure 2-1 represents a schematic diagram of a simple EB-PVD TBC system comprised of a bond coat, topcoat, substrate, and TGO. Each element has various materials with unique properties and functions.

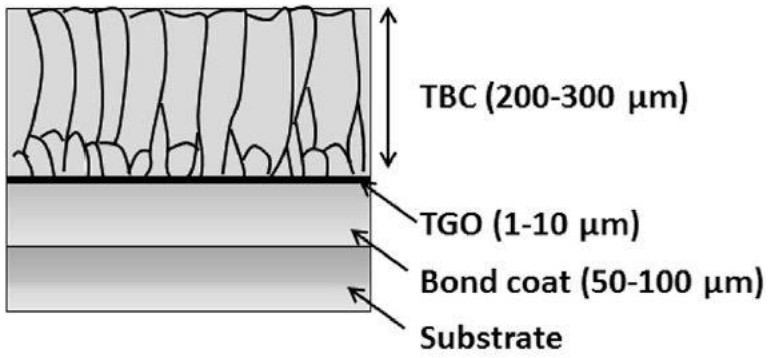


Fig. 2- 1 Typical structure of an EB-PVD TBC [27].

While the TGO is created on the outer side of the bond coat, the bond coat layer is put on the substrate of the superalloy. Also, the topcoat is put on the TGO covered with the bond coat [28]. Typically, there are two types of bond coats, either the $MCrAlY$ overlays (where $M$ could be $Co$, $Ni$, or $NiCo$) [23], or the platinum-modified nickel aluminide ($NiAl + Pt$) [29]. The bond coat oxidizes the aluminum and other reactive metals like $Y$ or $Cr$ in order to protect the oxidation of the substrate. A protective TGO layer, which sticks to the bond coat, is formed by the $MCrAlY$

overlays. Moreover, $\alpha - Al_2O_3$ is the most common oxide layer that crystallizes during the deposition of the topcoat or its service life [30]. Figure 2-2 shows the distribution of temperature across the various layers of TBCs.

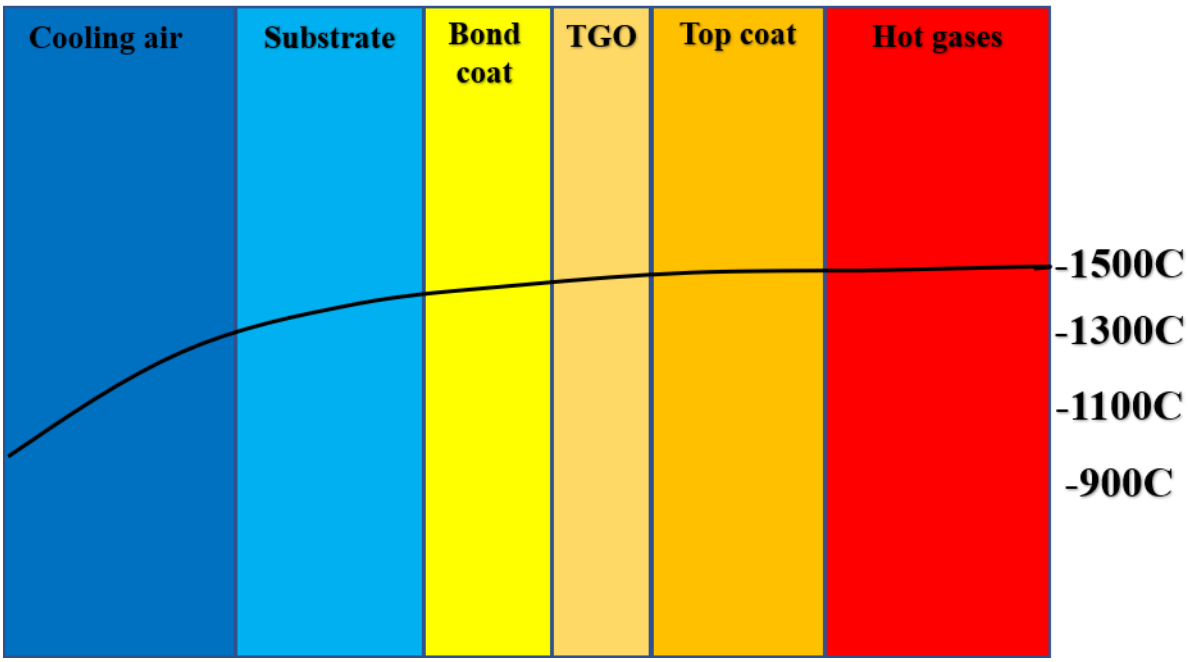


Fig. 2- 2 Schematic representation of the temperature distribution of TBC's layers.

Improving the TBC's performance is a crucial factor in the development of gas turbine applications [31]. One key of these applications is to optimally decrease the temperature all over the topcoat, hence permitting higher engine efficiencies and higher turbine entry temperatures [32]. As a result, it is essential that the thermal conductivity of the topcoat of ceramic be reduced and that the value stay low when exposed to service conditions for a long time. When the thermal conductivity is reduced, this produces a countereffect on some other properties, like sintering resistance (avoiding the agglomeration of particles) [33] and high-temperature phase stability [26], which help to prolong the service life of a coating.

The oxidation of $Cr, Al, Y,$ or other metals affects the growth rate of the TGO layer. The (TGO) layer is shaped between the bond coat and the topcoat when oxygen enters the coating. The interconnected porosity in the topcoat layer allows for easy diffusion of oxygen from the engine environment to the bond coat. In $ZrO_2$-based ceramics, the ionic diffusivity of oxygen is very high. Even dense topcoats are made "oxygen-transparent" as a result of this diffusivity [28].

The parabolic growth equation of the TGO growth rate is given by [34]:

$$h^2 = 2k_p t \tag{2.2}$$

where $t$ is time (sec), $h$ is the thickness (μm), and $k_p$ is a parabolic rate constant. TGO grows by counter-diffusing aluminium and oxygen across the grain boundaries of $\alpha - Al_2O_3$. The outward diffusion of aluminum and the inward diffusion of oxygen from the bond coat are shown in Figure 2-3. The parabolic TGO growth rate and diffusion flux are affected by the grain size of $\alpha - Al_2O_3$ [35]. It is generally expected that transient metastable alumina (theta and gamma) will form at the initial oxidation stage and then will change to a stable $\alpha - Al_2O_3$ [36]. The new $\alpha - Al_2O_3$ forms at the interface of the bond coat (when there is a rapid inward diffusion of oxygen) or at the TGO surface (when there is a faster outward diffusion of aluminum).

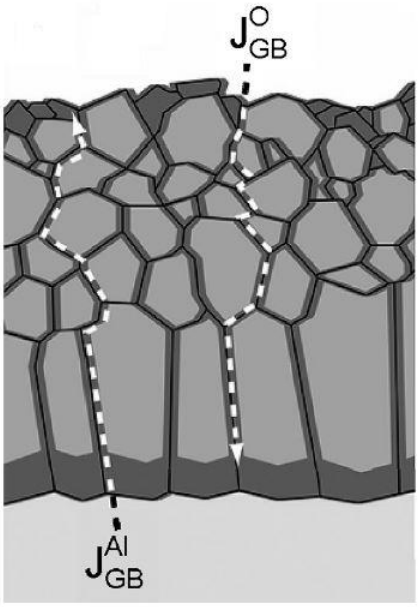


Fig. 2- 3 Aluminum's outward and Oxygen's inward diffusion from bond coat [35].

## 2.2 Coating deposition methods of TBCs

A coating's thermal conductivity depends on the technique employed during the deposition of the coating layer. In addition, various coating methods can affect the microstructural properties. Currently, there are many deposition techniques; nonetheless, only EB-PVD and APS techniques will be discussed in this study. The two techniques mentioned above are mainly used for aero engines and land-based turbine engines, respectively. New techniques are usually based on these two methods of coating.

### 2.2.1 Electron beam physical vapour deposition (EB-PVD)

EB-PVD is a well-known method used for processing ceramic topcoats. Here, the coatings are produced by vapour condensation and have a columnar microstructure. The coating contains defects, such as cracks and grain boundaries that are perpendicular to the interface between the metal and ceramic [37]. To produce the vapours, the ceramic placed in a crucible under the workpiece and is melted and evaporated using an electron beam. EB-PVD is carried out in a vacuum chamber.

Vacuum chambers prevent the contamination of the vapour phase of the condensate (coating) and/or the molten material in the crucible. Preferably, the different ceramic columns are not bonded well to the adjacent columns. However, the bonding between the underlying substrate and the coating is very strong [38].

The very fine columnar structure of EB-PVD can tolerate the introduced strains while the underlying substrate is being expanded [39]. In this process, to heat and vapourize the ceramic feedstock, a high-energy electron beam is utilized. The vapour moves at ninety degrees to the substrate in which it condenses atom by atom [40]. During the processing of zirconia-yttria ceramics, the low partial pressure of oxygen is kept constant so as to maintain the stoichiometry of zirconia. For EB-PVD, the bond coat/topcoat interface is flat when compared to coatings that are sprayed with plasma.

Figure 2-4 illustrates the structure of EB-PVD. EB-PVD's microstructure coatings yield better resistance to thermal shock and optimized strain tolerance which boosts their lifetime significantly. The EB-PVD TBC can be utilized without breaking under the stress of the components of the gas turbine engine that have greater thermal gradients or higher operating temperatures. It is believed that the columnar growth can minimize the elastic modulus in the coating's plane to nearly zero.

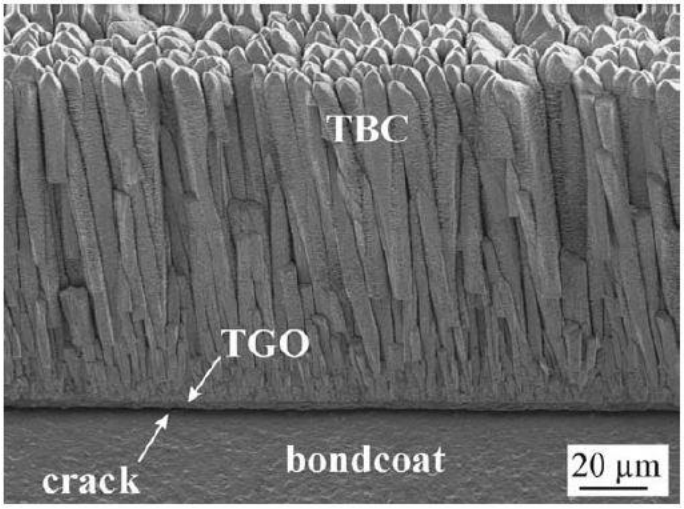


Fig. 2- 4 Micrograph of scanning electron microscopy of TBC applied by EB-PVD [41].

The operating temperature is likely to range between room temperature and over 1200℃ [42]. The coating's thickness, the flow rate of the internal coolant and cooling efficiency, and heat flux of the impinging hot gases are all factors that influence the thermal protection. In general, the use of thicker coatings is preferred for a higher thermal flux in order to reach the stated difference in temperature, $\Delta T$ [13].

One of the unfavourable factors of EB-PVD associated with its microstructure is that the TBCs fabricated by EB-PVD frequently yield the characteristics of columnar grain structure. This is where the pore channel between the columnar grains is usually parallel to the direction of the heat flux. A schematic representation of EB-PVD coating can be seen in Figure 2-5. As a result, this leads to an effective thermal conductivity, which is usually high in comparison to APS-TBCs [43].

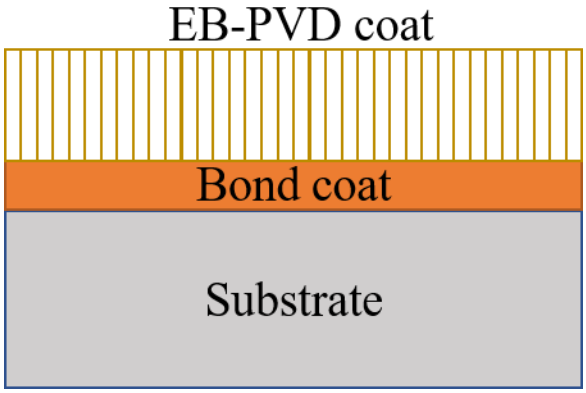


Fig. 2- 5 Schematic representation of coating prepared by EB-PVD.

There are certain properties of EB-PVD TBC that are better, in contrast to plasma-sprayed TBC. For instance, the finishing of the surface of the EB-PVD coatings is far better than that of APS coatings. The columnar structure of EB-PVD coatings has excellent strain tolerance properties. Furthermore, EB-PVD coatings are erosion-resistant because of their ability to withstand stress at higher temperatures. The microstructure of the coating plays a crucial role in the behaviour determination of the coating during its service life.

With the EB-PVD process, it is easy to control the mechanical and thermal properties of coatings. Vapour is produced during the EB-PVD process by using a beam of electrons to heat the source material, thereby leaving the evaporated atoms to slowly condense on the substrate. The nuclei of the crystal form at desired locations and grow along the thickness and laterally to shape the different columns, which produce a high intercolumnar porosity [44]. Figure 2-6 below presents a diagram of the process of EB-PVD coating

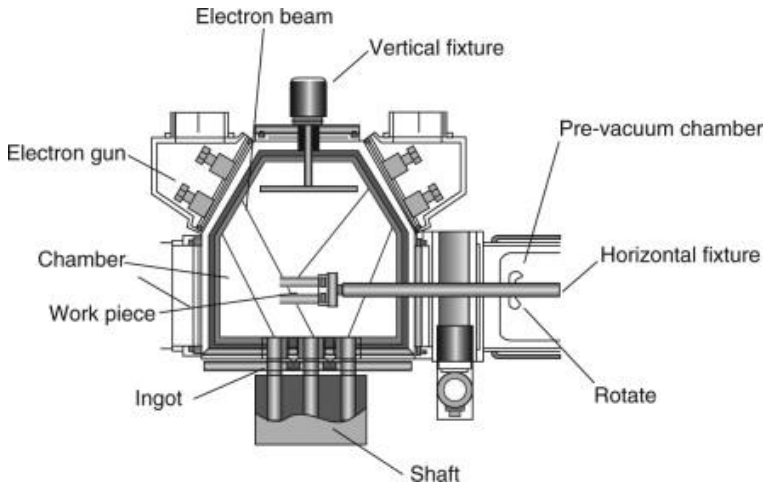


Fig. 2- 6 Schematic representation of the procedure of EB-PVD [38].

Nonetheless, APS-TBCs usually have a lamellar structure with many ellipsoid pore structures. As a result, the effective thermal conductivity is often lower when compared to a perfect TBC. Thus, it is crucial to have the spatial distribution, pore volume fraction, morphology, and orientation under control in order to produce TBCs with reduced or optimized thermal conductivity. The porous, micro-cracked columnar EB-PVD ceramic structures ensure that the coating is durable [45].

### 2.2.2 Atmospheric plasma spray (APS)

APS is used for depositing ceramic TBCs. In turn, TBCs are then used to protect and insulate hot-section metallic components in gas turbine and diesel engines. This method is less expensive compared to EB-PVD [6]. APS has a very high-temperature plasma jet. This allows materials to melt (given its high melting point) and produce an effective thermal spray. $Ar–He$ or $Ar–H_2$ hot plasma jet at high speed can melt the ceramic and metallic feedstock powder, allowing it to move at a high velocity.

Figure 2-7 presents a schematic diagram of the APS coating technique. Due to its quick solidification, the spray produces a coating on the substrate's clean surface. "Splats" are created by the plasma spray. These splats are the flattened particle boundaries that are in parallel to the interfaces between the ceramic and the metal.

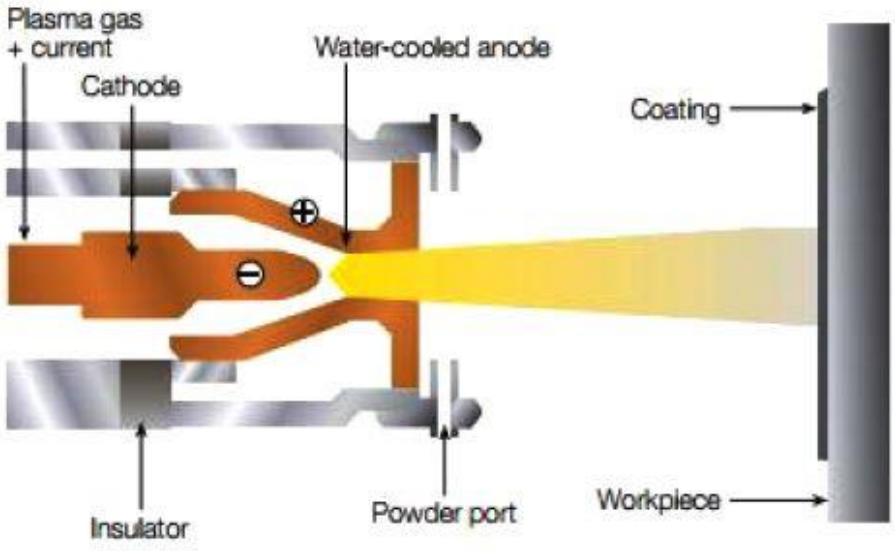


Fig. 2- 7 Schematic representation of the APS process [46].

An illustration of the APS splats is shown in Figure 2-8. Some spaces are left between the boundaries of the splat during the coating process. This is the result of the incomplete bonding between splats caused by the relaxation of residual stresses when the splat is being cooled, by trapped gases, or lack of adhesion. Only approximately 20% of the actual contact area between the different types of splats can be improved with the help of modern techniques [47], [48]. Thus, these splats affect the coating's properties, such as its thermal, electrical, and mechanical properties. These properties are not the same as the sprayed bulk material.

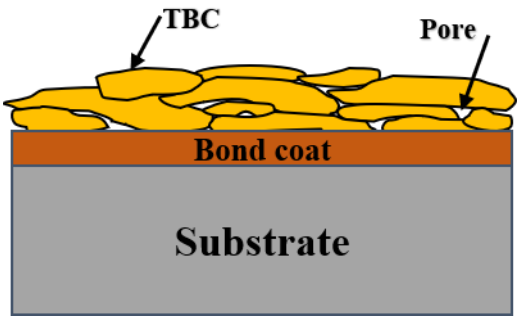


Fig. 2- 8 Schematic representation of splat of APS.

Besides the roughness of the substrate and its temperature, such as velocity and how the incident particles are distributed based on size, other factors have a huge impact on the coating's structure. This method of coating is commonly used for commercial purposes. The micro-cracks that run roughly parallel to the interface between metal and ceramic in APS-TBCs and the splat boundaries can efficiently reduce the thermal conductivity of APS-TBCs. Nonetheless, weakness can be introduced through the micro-cracks and splat boundaries in APS-TBCs. This affects the coatings' service life and can result in early spallation. Figure 2-9 presents a representation of the APS morphology.

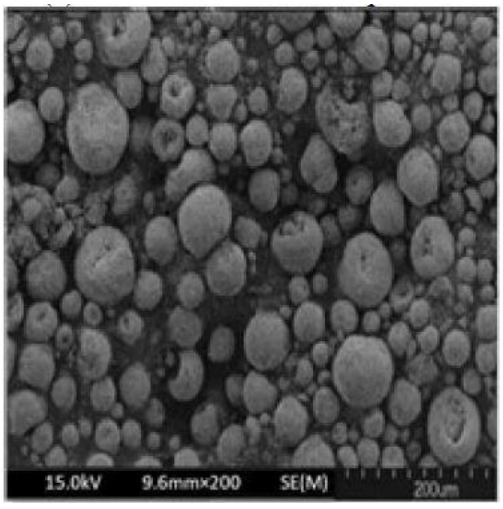


Fig. 2- 9 SEM micrograph of APS morphology [39].

The type of interaction between the ceramic feedstock and the plasma gas is essential for determining the properties of TBC applied by APS. This is because the TBC is produced by many solidifying particles per $mm^3$ after passing through a hot plasma region [50]. The APS-TBCs' thermal conductivity can reach up to 0.8-1.1 [W/m K] [51]. Furthermore, the structure of the porous APS TBCs, which consists of its cracks, pores, crack/coating interface, pore/coating interface, and layer interface, affects its effective thermal conductivity. Apart from the scattering effect at the interfaces and/or defects, another essential element which influences the final effective thermal conductivity of the APS-TBCs is the interfacial thermal resistance (ITR) [52].

Table 2-1 illustrates a comparison between EB-PVD and APS. Seven features of the two TBCs deposition techniques are compared. The areas where the coatings produce more benefits are defined by these features.

Table 2- 1 Comparison of properties of EB-PVD and APS coating.

| **Properties** | **EB-PVD** | **APS** |
|---|---|---|
| ***Microstructure*** | Columnar | Lamellar |
| ***Thermal conductivity [W/mK]*** | 1.5 | 0.8 |
| ***Surface roughness (µm)*** | 1 | 10 |
| ***Bonding mechanism*** | Chemical | Chemical and mechanical |
| ***Typical thickness (µm)*** | 100-300 | 200-400 |
| ***Lifetime*** | very long | short |
| ***Cost*** | Very expensive | Cheap |

## 2.3 Thermal conductivity of coatings

Thermal conductivity is the ability of a material to transfer heat; it can be defined as the rate of heat transfer through a particular material. With materials have a low thermal conductivity,

heat is conducted at a lower rate. The technique of applying a coating affects the thermal conductivity of the coating [16]. This is because the microstructure alters based on the technique of coating deposition. EB-PVD and APS techniques are the most-used methods for applying coatings. The thermal conductivity of coatings is adversely affected by some microstructural properties; these include: grain size, micro-cracks, pores and their distribution, voids, and impurities.

Currently, APS TBCs produce a thermal conductivity between 0.8 and 1.1 [W/m K]. However, the thermal conductivity produced by EB-PVD coatings is between 1.5 and 1.9 [W/m K]. The two techniques yield a thermal conductivity much lower than that of the bulk YSZ (2.2-2.5) [W/m K] [53]. EB-PVD coatings are less porous than APS coatings. As a result, this helps to minimize the thermal conductivity of APS coatings [54]. Figure 2-10 compares the thermal conductivity of EB-PVD, bulk zirconia, and APS coating. A porous ceramic layer's thermal conductivity is dependent on the intrinsic thermal conductivity of the bulk ceramic, which is connected to its structure, composition, and the architecture of the porous structure (i.e. distribution, geometry, and pore volume fraction) [41].

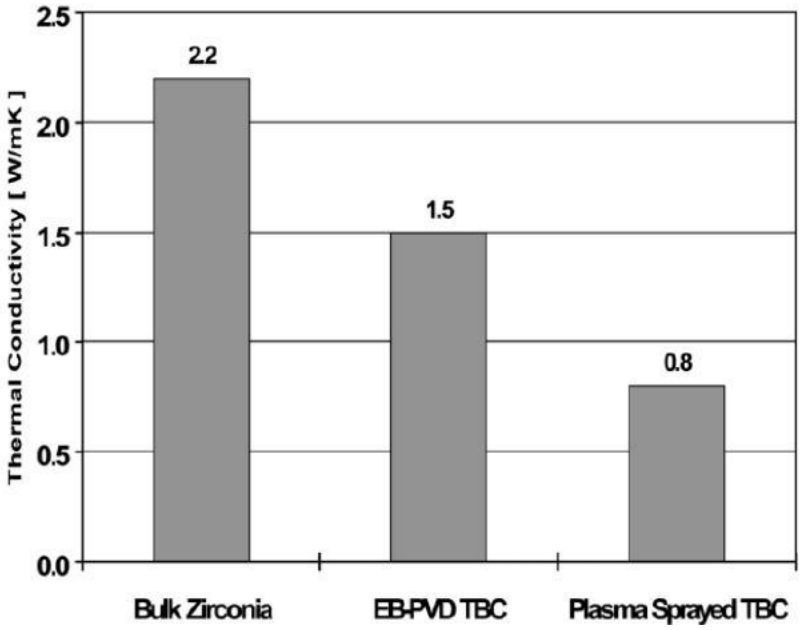


Fig. 2- 10 Comparison of thermal conductivity of bulk, EB-PVD and APS [53].

## 2.4 Techniques for calculating thermal conductivity

Various material properties such as thermal conductivity can be used to evaluate the design of a TBC. Lower thermal conductivity is suitable for high-temperature protective coating, along with a higher stability of the coating. Many techniques are used to measure these properties. The simplest and most common way of calculating the thermal conductivity of unknown material is discussed below.

The guarded heat plate method is used to calculate the thermal conductivity of materials [55]. This technique involves placing a sample between two plates, with one of the plates being the heat source, while the other plate is the heat sink. Heat transfer through a material with a cross-sectional area $A$ and thickness $L$ can be measured. The equation below is used to calculate thermal conductivity:

$$k = \frac{Q.L}{A.\Delta T} \tag{2.3}$$

where $L$ $(m)$ is the sample length, $Q$ $(W)$ is the heat load on the sample, $A$ $(m^2)$ is the cross-sectional area to which the heat is applied, and $\Delta T$ $(K)$ is the difference in temperature across the bottom and top of the sample. In this process, a Vernier caliper is used to measure the cross-sectional area. *Q*, the heat load, is calculated by using the voltage measurement across the sample. A copper sample holder is used to clamp down the sample. Varnish is used to place temperature sensors on the sample. To ensure better thermal conductance to the sensor, a dual-twist phosphor/bronze lead wire is wrapped around the sample. Heat moves from the top to the bottom of the material. To prevent heat leaks, testing is usually conducted in a vacuum. The voltage and current of heater coils and each sensor's temperature are recorded. Thermal conductivity is calculated using these measurements.

For cold samples, the guarded heat plate method is the most appropriate. Nonetheless, when it comes to thermal coatings, it is crucial to calculate thermal conductivity at high temperatures. As a result, an entirely different method is used. One method, which is used to determine TBCs' thermal conductivity at all temperatures is the Laser Flash Analysis (LFA) method [56]. Here, the substrate face of the sample is shot by a laser pulse, and an infrared detector is used to measure the resulting temperature rise on the other face of the sample.

The formula below is used to calculate thermal diffusivity after normalizing the signal:

$$\alpha = (0.1388L^2)/t_{0.5} \tag{2.4}$$

where $L$ $(m)$ is the sample's thickness, $\alpha$ $(m^2/sec)$ is the thermal diffusivity, and $t_{0.5}$ $(sec)$ is the time it takes the sample's rear face to reach half of its maximum rise.

Once the specific heat capacity $C_p$of the coating and density ($\rho$) are known, the thermal conductivity $k$ [W/m K] can be calculated using the following equation:

$$k = \alpha \rho C_p \tag{2.5}$$

This method does not have many requirements for measuring the thermal conductivity of YSZ coatings. One requirement is that a thin layer of graphite or gold must be used to coat the zirconia. This is because zirconia allows light in the operating wavelength of the laser to pass through it [57]. This coating does not allow the laser to pass through the zirconia ceramic layer. One considerable disadvantage here is that measurement on a real component is impossible, as only small, flat samples can be used to take measurements [58].

## 2.5 Mechanisms of heat transfer

Thermal conductivity is the results of coatings heat transfer property. This property is an essential factor in determining the performance of the coating and a major design parameter for TBCs [59]. The thermal conductivity of ceramic coatings is heavily affected by the extrinsic characteristics (oxidation, microstructural defects, and temperature) and the intrinsic properties of the material [60].

The changes in temperature in the material impact its thermal conductivity [61]. There is a change in the mechanism that is mostly used for heat transport which takes place at elevated temperatures for a material like YSZ. The thermal conductivity of YSZ decreases from room temperature to approximately 800 °C. This is because at high temperatures, the phonons' density

rises and they crash into other phonons and decrease the mean-free path. As a result, the scattering of phonons is more noticeable with increasing temperatures, especially for zirconia.

The interaction between the phonons increases when the temperature of zirconia coatings becomes high. As a result, the phonons are deflected from straight paths and as the temperature increases, the mean-free path is reduced. Additionally, the thermal conductivity of zirconia coatings reduces as the mean-free path reduces. The intrinsic phonon scattering scales limit the thermal conductivity as 1/T [62]. At elevated temperatures, photon conduction (radiation) is essential and can quickly increase the thermal conductivity (proportional to $T^3$) — especially for zirconia coatings [63]. Figure 2-11 illustrates the relationship between the thermal conductivity of YSZ and temperature

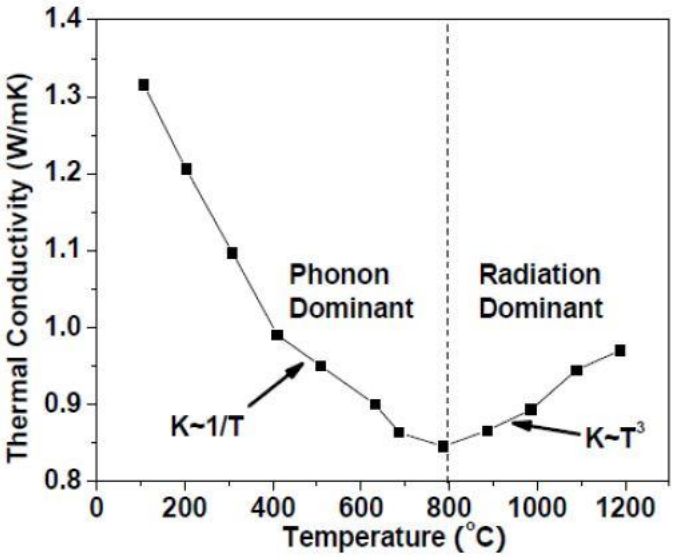


Fig. 2- 11 Thermal conductivity of YSZ as a function of temperature [60].

The underlying mechanisms of conduction, transfer of energy by phase change, and radiation are used to categorize heat transfer. These mechanisms depend on the photons and phonons and how they interact with their surroundings. The thermal conductivity of the as-sprayed

TBCs (mostly for APS) depends on specific molecular interactions. Figure 2-12 shows five types of interactions.

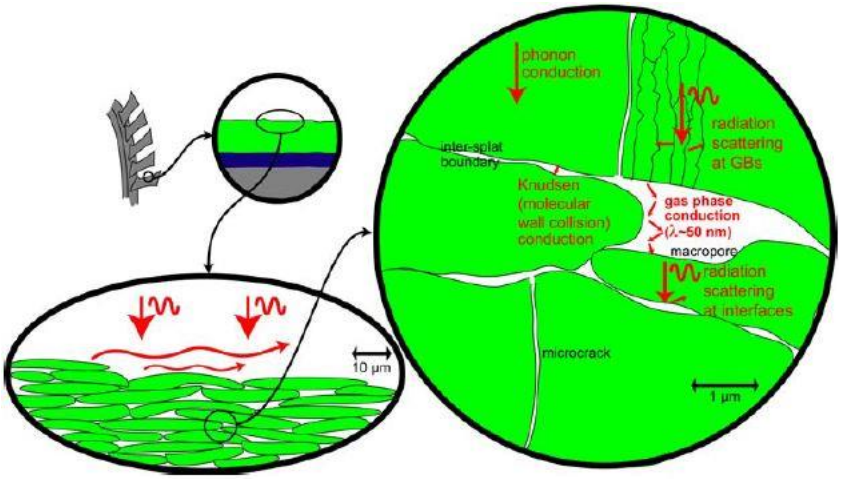


Fig. 2- 12 Schematic illustration of the mechanisms of heat transfer of APS-TBCs [64].

- The crystal lattice vibration causes phonon conduction
- The radiation scattering at grain-boundaries
- Knudsen conduction, which is induced in the inter-splat interface
- Gas phase conduction
- Radiation scattering at any type of interfaces, such as splat interfaces and the interfaces between the coating and defects

These interactions may not appear in every type of coating. The heat transfer mechanism is affected by the microstructure of a coating. Alloys of zirconia serve as electronic insulators because they do not have enough free electrons. Electrons have no effect on the overall thermal conductivity of the system. This is because radiation (photons) or lattice vibrations (phonons) control the transfer of heat in the case of zirconia. Phonon conduction plays a powerful role in the transfer of heat. The overall thermal conductivity ($k$) of ceramic materials [65], which is the summation of three parts, is given by the general equation:

$$k = 1/3 \sum_{j=1}^{N} C_{pj} v_j l_j \quad (2.6)$$

where $l_j$ is the corresponding mean-free path, $N$ is the overall number of the carriers of energy, $C_p$ is the specific heat at constant pressure, and $v$ is the velocity of the carrier. If the carrier is a wave, this is called group velocity. There are two parts of the electron mean-free path. One part is the intrinsic mean-free path which corresponds to the electrons scattering by lattice vibrations. The other part is the residual mean-free path, which corresponds to the electrons scattering by defects. The intrinsic mean-free path is directly proportional to temperature while the residual mean-free path does not depend on temperature. The contribution to thermal conductivity ($k_p$) from the lattice vibration is as follows [66]:

$$k_p = 1/3 \int C_v \rho v l_p \quad (2.7)$$

where $v$ is the speed of phonon, $\rho$ is the density, $l_p$is the mean-free path for the scattering of phonons, and $C_v$ is the specific heat capacity.

The thermal conductivity of ceramics rises with an increase in temperature due to the heat transfer of photons (radiation conduction). The following equation shows the thermal conductivity as a result of radiation effect [67]:

$$k_r = 16/3\pi\sigma n^2 T^3 l_r \quad (2.8)$$

where $\sigma$ is the Stephen-Boltzmann constant, $k_r$ is the thermal conductivity as a result of radiation, $T$ is the absolute temperature, $l_r$ is the mean-free path for photon scattering, and $n$ is the refractive index. It can be seen from the equation that the thermal conductivity of ceramics at elevated temperature is dependent on $T^3$. The overall theoretical thermal conductivity of zirconia-based

systems equals the addition of the thermal conductivity by phonon transport and the thermal conductivity by photon transport, which is written as:

$$k = k_r + k_p \tag{2.9}$$

Below 1200 °C, heat conduction through zirconia is governed by phonon transport. However, when the temperature increases, increased radiation is felt at 1250 °C when a 10% contribution is expected [66]. In real crystal structures, phonon scattering takes place when phonons interact with lattice imperfections. These imperfections incorporate vacancies, ions, dislocations, grain boundaries, voids, and atoms whose ionic radius differ or atoms with differing masses and other phonons [68]. When the bond length is locally distorted, scattering occurs, thereby introducing elastic strain fields into the lattice. The quantification of the effects of these imperfections can be done via their impact on the phonon mean-free path ($l_p$). The phonon mean-free path is given by the equation below [66]:

$$\frac{1}{l_p} = \frac{1}{l_i} + \frac{1}{l_{vac}} + \frac{1}{l_{gb}} + \frac{1}{l_{strain}} \tag{2.10}$$

where $l_i, l_{vac}, l_{gb}\ and\ l_{strain}$ are the contributions of the mean-free path as a result of interstitials, vacancies, grain boundaries, and lattice strain, respectively. In nanostructured coatings, the effect of grain boundaries can be high [18]. The strain fields and the intrinsic lattice structure significantly affect both coated structures and conventional materials.

## 2.6 Impact of different parameters on thermal conductivity of TBCs

Thermal conductivity is a major material property that could be affected by even small changes in the microstructure of material or composition. The effect of some of these factors on the thermal conductivity of coatings is considered in this section.

### 2.6.1 Thermal conductivity affected by yttria content

Microstructural properties have a great effect on the thermal conductivity of zirconia-based coatings [69]. Changes, which occur at the micro-level, are caused by the process parameters utilized in the various coating methods. These processes significantly affect the structure and morphology of the coating. The EB-PVD coating is columnar in structure, whereas the structure of APS coatings is represented by a splat-like structure. When the process parameters are optimized, the coatings deposited can have a thermal conductivity that is lower than that of the thermal conductivity of bulk materials.

The range of the thermal conductivity of bulk zirconia is between 2.2 and 2.8 [W/m K]. Conversely, however, the thermal conductivity of YSZ based coatings is lower, within the range of 0.8-1 [W/m K] [62]. The percentage of yttria in the coatings, as well as additional parameters such as heat treatment or deposition technique, affects this change in thermal conductivity. The thermal conductivity is reduced when yttria is added, as this corresponds to a shorter intrinsic mean-free path as a result of the introduction of local strain fields and vacancies generated by incorporating large dopant atoms and the local modifications of the lattice structure. The role of vacancies and strain fields is to scatter the phonons, directly raising the dispersion of the phonon in the lattice. When dispersion is increased, it is likely that there will be interactions between

phonons, which further reduce the mean-free path. The thermal conductivity of the coating decreases with an increased yttria content [68].

According to Srinivasan et al., at a given temperature, the decrease in thermal conductivity with increased yttria content is consistent with oxygen vacancies that significantly affect phonon scattering [69]. The impacts of yttria content on the thermal conductivity are described in Figure 2-13 which shows that there is a significant change in thermal conductivities in the case of 12YSZ and 14YSZ. On the other hand, in the case of 16YSZ, 18YSZ, and 20YSZ, the change in thermal conductivities is small compared to the first case. Thus, a further increase in yttria content has no effect the thermal conductivity of ceramic [70].

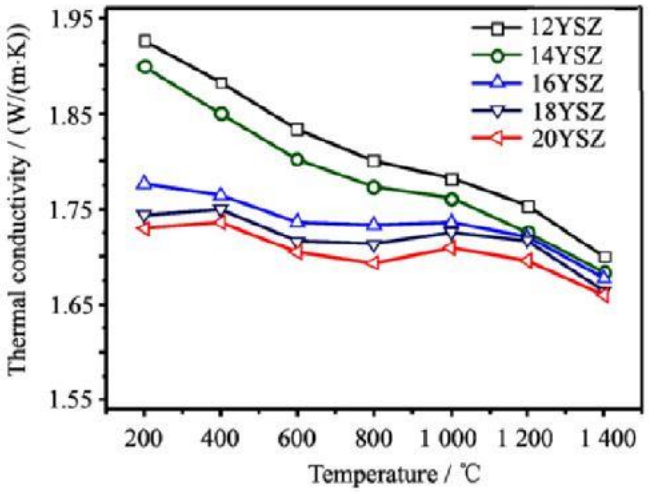


Fig. 2- 13 Impact of different yttria content on thermal conductivity of YSZ ceramics [70].

## 2.6.2 The thermal conductivity of coatings affected by impurities

The reduction in the thermal conductivity of an insulator can be done efficiently by adding structural defects that are obstacles to the phonons' propagation [71]. Various types of defects are likely to be predicted such as voids, vacancies, pores, interfaces (grain boundaries), substitution

ions, cracks, and dislocations, etc. The function of vacancies is crucial when it comes to zirconia-based materials [72]. Phonon scattering is improved greatly since nanostructured TBCs have numerous grain boundaries. Additionally, the presence of micron and nano pores, solute atomic point defects, and oxygen vacancies in the TBCs' nanostructure can lead to enhancing the effect of phonon-scattering, which in turn significantly optimizes the insulation effect of the TBCs' nanostructure [73].

A 'vacancy' is considered to be a complete disappearance of mass, which is one type of lattice defect, and a discrepancy in volume on the crystalline sites, including the neighbouring chemical bonds as can be seen in Figure 2-14 below. This vacancy results in the strongest lattice distortion and phonon scattering. Consequently, the distortion results in additional scattering. When the concentration of the vacancies increases, the thermal conductivity is lowered.

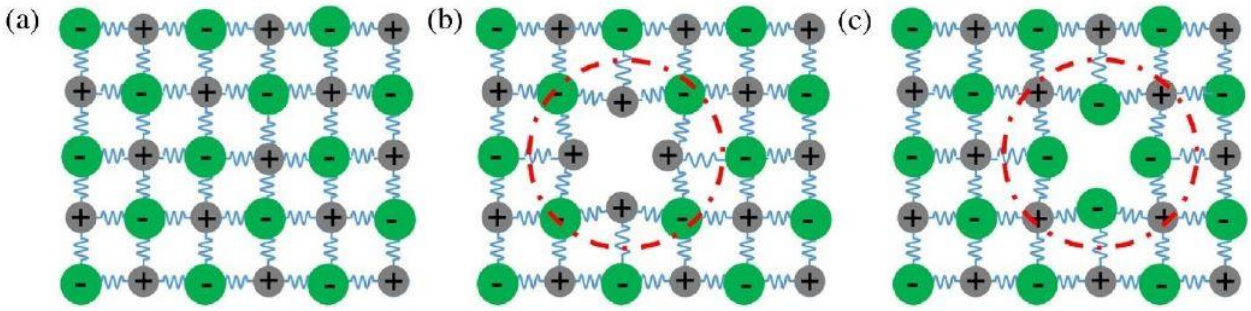


Fig. 2- 14 Schematic diagram of (a) pure crystal lattice (b) lattice with defect (anion) (c) lattice with defect (cation) [74].

The unwanted transformation of pure zirconia at higher temperatures of approximately 1100 °C means that this is not utilized. The addition of hetero elements such as $Mg$, $Y$, or $Ca$ is used to fully or partially stabilize zirconia, which then stabilizes the cubic or the tetragonal form. To fully stabilize the cubic phase of zirconia, a 20 wt.% of $Y_2O_3$ is added to the zirconia. Furthermore, to achieve the metastable t' phase, a 6 to 8 wt.% of $Y_2O_3$ can be added. Figure 2-15

shows the phase diagram of the different phases. To maintain the electrical neutrality of the ionic lattice, hetero elements and vacancies are introduced. The thermal conductivity of zirconia can be minimized by the addition of hetero elements like $Ca$, $Mg$, or $Y$.

.

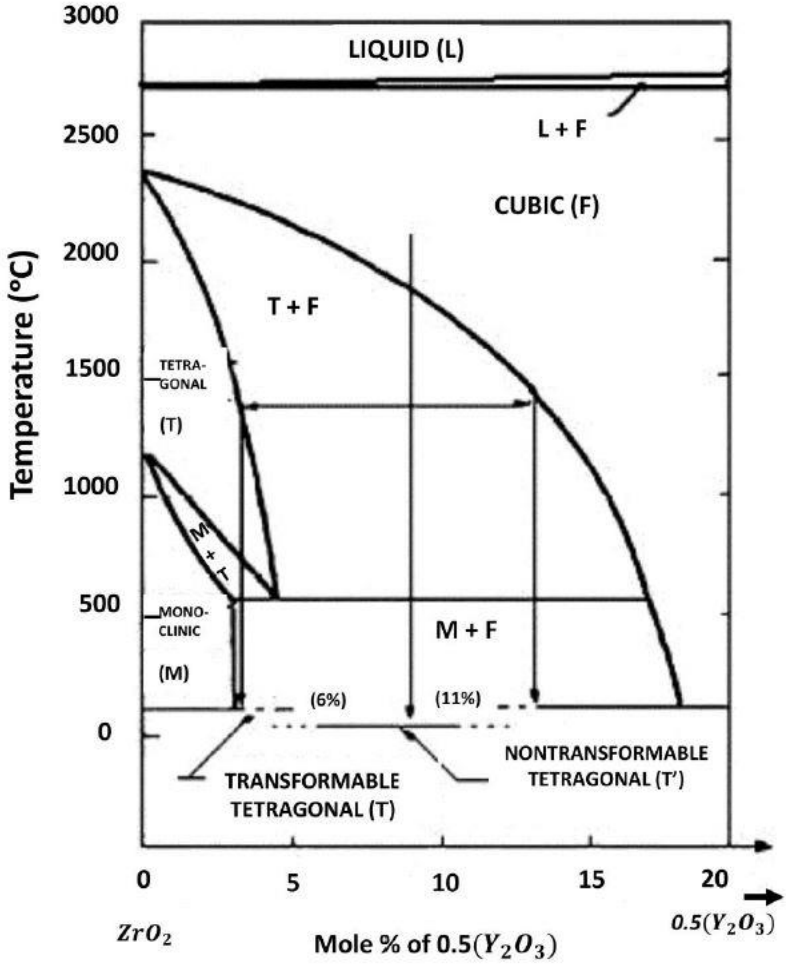


Fig. 2- 15 Phase diagram of $ZrO_2$ representing the effect of yttria on different phases of zirconia (Tetragonal, T, cubic, F and monoclinic, m) [75].

## 2.6.3 Effect of layering on EB-PVD TBCs

Researchers have implemented various techniques to reduce thermal conductivity. One of these techniques involves introducing extra phonon scattering centres in the coating so as to lower

the thermal conductivity of EB-PVD TBCs [66]. The dispersion of photons and phonons influences heat transfer [76] and the scattering of heat carriers in between the layers at the interface is then feasible. Thus, adding a layer to the topcoat can be efficiently used to counter thermal transfer [77].

Different layers are combined to act as one component in order to lower the thermal conductivity of coatings. To fully understand this effect, one needs to contemplate a TBC that is made up of many nanolayers of various materials such as alumina and zirconia [78], with the added benefit of heat resistance at interfaces/boundaries. The possibility of scattering by heat carriers increases as the number of interfaces increases.

In the ceramic coating, layering raises the areas of scattering, which in turn leads to decreased thermal conductivity. An overview of the layering method is shown in Figure 2-16 which shows an increase in the number of inner zones present in the layered coatings, as well as a corresponding decrease in thermal conductivity in comparison to a single layer.

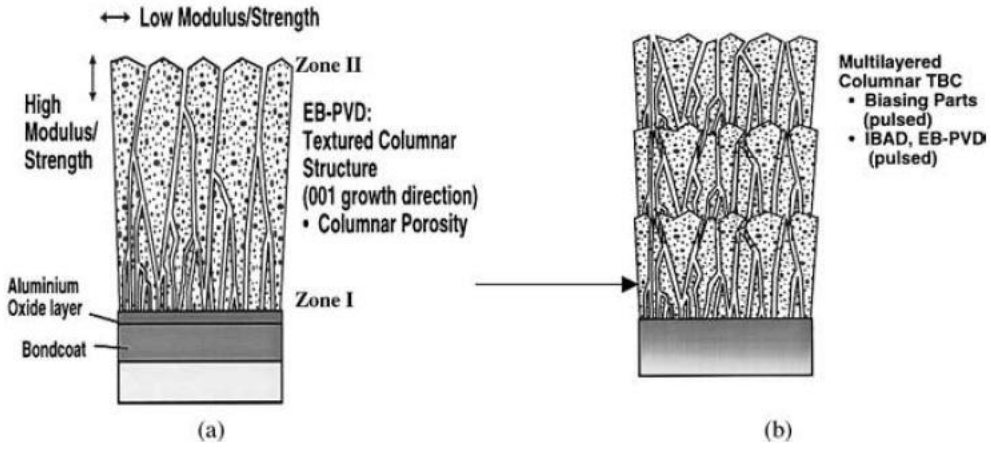


Fig. 2- 16 Schematic representation of EB-PVD TBC [79].

The thermal conductivities of these coatings differ due to the microstructures created within the coatings. It is widely believed that the presence of defects such as porosities and cracks

in the coating decreases the thermal conductivity. During the design of the topcoat layer there will be an increase in the coating's density and thus, there may be premature delamination if the layers are very distinct [79].

### 2.6.4 Thermal conductivity affected by interface

One of the essential structures in TBCs is the interface. When there is a heat flow between two adjacent layers or the interface of two distinct materials (phases), there is a temperature decrease at the interface. This rapid temperature change, even for a thin coating is due to the ITR which can be explained by the following equation [52]:

$$R = \Delta T / J \tag{2.11}$$

Where $R$ is the interfacial thermal resistance's value; $J$ is the density's heat flux, the heat flow per unit area per second; and $\Delta T$ is the difference in temperature between the two opposite interfaces. In 1941, when ITR was discovered, the temperature drop was at the solid-liquid interface [80]. Due to the temperature fluctuations at the interfaces, the composite materials exhibit a decrease in thermal conductivity because of the existence of the ITR. Figure 2-17 shows the reduction in temperature as a function of dislocation with the presence of ITR. The decrease in temperature at the bond coat/topcoat interface results from boundary changes. These changes are the result of the difference in the properties of the material of bond coat and topcoat.

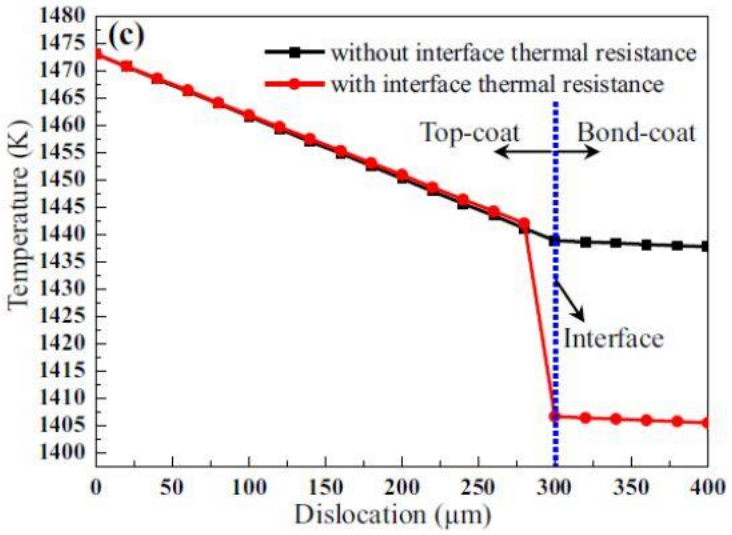


Fig. 2- 17 The effect of interfacial thermal resistance [52].

As-sprayed TBCs' effective thermal conductivity can be influenced by the roughness of the interface of the topcoat and the bond coat [81]. As the amplitude of the interface increases, the effective thermal conductivity increases, taking into account the interfacial thermal resistance. Nevertheless, this tendency may not be seen without considering the ITR.

# Chapter 3 Numerical and Analytical Models for Thermal Conductivity

Modelling and predicting the thermal conductivity of TBCs is research currently in progress. Modelling uses previous data to develop either a numerical model or an analytical model. An estimation of the coatings that, can be produced with altered properties, can be provided by these pre-existing models.

First and foremost, a short introduction of thermal conductivity is presented herein. Thermal conductivity ($k$) is the measure of the transfer of heat from the first surface to the second surface with a cross-sectional area *A* and with the distance between surfaces as *L*. Numerous equations can be used to estimate the thermal conductivity ($k$) based on the coatings and its parameters. In this case, the determination of the thermal conductivity of free-standing materials is given by [82]:

$$k = \rho . \alpha . C_p \tag{3.1}$$

where $C_p$ is the materials' heat capacity at constant pressure ($J/kg.K$), $\alpha$ is the rate of thermal diffusion ($m^2/\mathrm{sec}$), and $\rho$ is the free-standing materials' density ($kg/m^3$).

When the thermal conductivity is modelled before the fabrication of the coating is done, it helps to establish a superior understanding and predict the properties of modified or new coatings [83]. In most cases, these models yield calculated results that can be compared to the measured results [84]. Modelling ensures cost reduction and predicts the ideal potential combination of parameters for production out of many potential combinations, thereby improving efficiency.

Models produced from previous research work can be utilized for the prediction of thermal conductivity. The following section will discuss and summarize these existing models.

## 3.1 Numerical Models

The influence of powder morphology on the properties of YSZ coatings sprayed with plasma was examined by Kulkarni et al. [85]. The coating microstructure was represented using a two-dimensional finite element model. Three classifications of voids, namely: globular pores, intra-splat cracks, and interlamellar pores, were taken into consideration. The thermal conductivity values they predicted were higher than the ones from the experiment. The reason for this was that they did not have reference information for pore and splat size distribution.

Bartsch et al. [86] did a comparison of the results from the finite element simulations and the finite difference (Tbctool) to assess the thermal response from white and black images of EB-PVD TBC microstructures. As the mesh size continued to decrease and the image area became larger, the results became more accurate.

The finite element method (FEM) was used by Wang et al. [52] to simulate the behaviour of TBCs with various interfacial characteristics during heat transfer based on various ITR models. The results of the simulation revealed that the heat flux around the interface has a significant changing characteristic and that TBCs' thermal insulation effect could be improved by increasing the interface's area. It was found that the roughness of the interface (amplitude) also has a significant impact on the effective thermal conductivity of the as-sprayed TBCs.

Using SEM images of coating microstructure, Tan et al. [67] were able to produce a 2D finite element mesh. Moreover, when using a commercial finite element code for some ceramic coatings, they were also able to predict the thermal conductivity. For YSZ coatings, the thermal conductivity values obtained from the Laser Flash Analysis (LFA) were lower than the values of the predicted results.

## 3.2 Analytical Models

One of the best approaches to minimize the thermal conductivity of TBCs is to use the porous microscopic structure [87]. To evaluate the overall thermal conductivity of the ceramic coatings deposited by different deposition methods, a substantial number of analytical models have been developed [88]. Modelling can also be used to enhance the understanding of the impact of shape, pore size, pore morphology, and orientation. The majority of the models are in the form of randomly distributed, non-interacting pores of spheroidal shapes or ellipsoids, and some with periodical forms.

In the late 19$^{th}$ century, Maxwell-Eucken developed one of the early models [63]. It was assumed that the 'dispersed phase' was made up of non-interacting, randomly distributed, and alike spheres. The equation below describes this model, as follow [89]:

$$\frac{k_{tot}}{k_d} = \frac{1-P}{1+{}^{1}/_{2}P} \tag{3.2}$$

where $k_d$ is the dense material's thermal conductivity, $k_{tot}$ is the total thermal conductivity of a porous material, and $P$ is the porosity's fraction. The thermal conductivity of pores was assumed to be small or negligible in this model.

Klemens developed another model which applies to randomly distributed, non-spherical pores. This model is given by [90]:

$$\frac{k_{tot}}{k_d} = 1 - \frac{4}{3}.P \tag{3.3}$$

where $k_d$, $k_{tot}$, and $P$ are as defined above.

Another model that computed the impact of cracks with different orientations on the thermal conductivity of solid materials was developed by Hasselman [91]. This model's conclusion was that cracks which are parallel to the heat flow direction have less impact on thermal conductivity. In contrast, the maximum thermal resistance is acquired with cracks that are aligned perpendicularly to the heat flow direction.

An excellent model was developed by Bruggeman to estimate the thermal conductivity of porous materials. Bruggeman was able to apply the Maxwell model to systems that have a random distribution of spherical particles of various sizes. For his proposed model, he believes that if a somewhat large spherical particle is dropped into a dispersion that contains many smaller particles, the disturbance of the field around the large sphere will most likely be negligible as a result of the small spheres. Using this model, he demonstrated that he could remove the limitation on the volume fraction of dilute dispersion. An extension of Maxwell's model is written as follows [92]:

$$\frac{k-k_m}{k+2k_m} = f\frac{k_d-k_m}{k_d+2k_m} \tag{3.4}$$

A change in the volumetric fraction of dispersed phase, with the change in conductivity, $dM$, can be described as follows:

$$\frac{dM}{3M} = \frac{dP}{1+P}\left(\frac{k_d - M}{k_d + 2M}\right) \tag{3.5}$$

The integration of both sides of the equation (i.e. $M$ from $k_m$ to $k$ and $P$ from zero to $\frac{f}{1+f}$) leads to the two-phase model of Bruggeman, which is written as follows [93]:

$$(1-f) = \left(\frac{{}^{k}/_{k_m} - {}^{k_d}/_{k_m}}{\left({}^{k}/_{k_m}\right)^{\frac{1}{3}}\left(1 - {}^{k_d}/_{k_m}\right)}\right) \tag{3.6}$$

where $f$ is the volume fraction of the $i_{th}$ phase, $k$ is the composite's thermal conductivity, $k_d$ is the dispersed phase's thermal conductivity, and $k_m$is the matrix's thermal conductivity.

An analytical model was developed by McPherson to predict the thermal conductivity of ceramic coatings sprayed with plasma that included areas of good and insufficient contact between lamellae where the areas of insufficient contact behave as thermal insulations. This model is described as follows [94]:

$$\frac{k_{tot}}{k_d} = \frac{2.\delta.f}{\pi.a} \tag{3.7}$$

where $f$ is the true contact's fraction, $\delta$ is the thickness of lamellae, and $a$ is the radius of each single contact area.

A further model was proposed by Sevostianov et al. [95] to supply an enhanced connection between the thermal conductivities and microscopic structure parameters. It was assumed that the microstructure comprises two classes of horizontal and vertical penny-shaped cracks. The following equation describes the thermal conductivity in the direction horizontally aligned to the material:

$$\frac{k_{tot}}{k_d} = 1 - \frac{8\alpha_v}{3(1-P)} \tag{3.8}$$

where $\alpha_v$ is the component of crack density tensor in the direction horizontally aligned to the material, and $P$ is the density.

A model was suggested by Lu et al. [96], which incorporates various types of pore morphologies including, aligned but spatially random pores, randomly oriented pores, zigzag pores, and periodic pores. The thermal conductivity of zigzag pores was calculated using the Finite Element Method (FEM). The model was extended to TBCs deposited by EB-PVD. For zigzag pores, the effective thermal conductivity $k$ is given by:

$$k = \frac{\bar{q}}{(T_{bottom} - T_{top})/\lambda} \tag{3.9}$$

where $T_{bottom}, T_{top}$ are the bottom and top surfaces' temperatures respectively, and $q = q_z$ is the heat flux in the $z$-direction averaged in $x$ over the top (or bottom) surface.

A model was presented by Wei et al. [97] to study the impact of imperfections on the thermal conductivity and compute the effective thermal conductivity. They suggested an independent variable, $C_k$, which is mainly influenced by the nonlinear region around the imperfection. Their conclusion was that this variable does not depend on the thermal gradient. Increase in temperature does not significantly affect the value of $C_k$. The effective thermal conductivity of defects consisting of $n$ pores which are not influenced by each other is given by:

$$K_{eff} = K_o(1 - \rho - \frac{\alpha \sum_{i=1}^{n} a_i^2}{hl}) \tag{3.10}$$

where $K_o$ is the non-defective bulk material's intrinsic thermal conductivity; $\alpha$ is considered a numerical value that equals 3.06; $l$ and $h$ are the model's width and height, respectively; and $a$ is the radius of the pore.

# Chapter 4 Six-phase Model for Evaluating Thermal Conductivity of TBCs

As mentioned earlier in Section 2.6, the way that TBCs perform under high temperature is significantly affected by their microstructural attributes [61]. The mechanical and thermal properties of ceramic coatings are equally affected by the process parameters and the type of deposition method used, as well as the coatings' intrinsic thermal attributes [98]. These elements can affect the size, shape, and morphology of the ceramic coating's porosity.

The TBCs' complex structure can be explained more clearly and in more detail, using analytical models [99]. The thermal conductivity of dense coatings is greatly affected by the defects present [97]. Generally, these defects are also known as pores. There are different types of pores, such as randomly oriented pores, vertical or horizontal pores, and open pores [100]. The best shape for modelling is the spheroidal shape, as it can cover many types of pores or actual cracks, orientation, or shape. Two classifications of models are used for pore distribution, asymmetrical models and symmetrical models. The schematization of pores either by distributing pores symmetrically into the whole matrix or by dispersing the unique grains into the continuous matrix, has resulted in this type of classification.

The TBC's performance is linked to its porosity. Thus, it has become crucial to design the thermal properties of these materials using a modelling approach before real manufacturing is applied.

The way the porosity is distributed in the analytical model can be accurately presented; nevertheless, one has to take into account various conditions, such as ensuring that the

microstructural details of the model are enough to represent the material's properties [101]. The smallest of details must be considered when it comes to the microstructural attributes of the coating in order for the real properties to be precisely modelled.

There are many developed analytical models, some of which were discussed in Chapter 3. Models that are a hybrid combination of both symmetrical and asymmetrical models can predict the thermal conductivity more accurately. The Bruggeman asymmetrical model is one model that can yield a better evaluation of the thermal conductivity of a coating [93].

As stated in Chapter 1, the proposed model in this thesis (i.e. six-phase model) is based on Bruggeman's two-phase model. In this section, the details of Bruggeman's model will be reviewed. The following are some of the assumptions in this thesis:

- The impact of connected pores is negligible.
- The thermal conductivity of the defects or the dispersed phase is insignificant, and it is neglected.
- Heat exchange can only take place along the thickness of the coating (or at right angles to the interface between the bond coat and the substrate). There is no assumption that lateral heat transfer takes place.
- The relationship between thermal conductivity and porosity is linear.

In Bruggeman's model, many spheres are introduced into a dilute dispersion consisting of infinite values for different sizes; furthermore, each sphere is part of the continuous matrix. Bruggeman was able to eliminate the constraint on the volumetric fraction of the dilute dispersion, which was impossible in respect to other models ($0 \leq f < 1$). The model was designed by

Bruggeman for a porous TBC system. His model considered just one type of defect that has a single orientation (i.e. spherical particles).

A simple case of Bruggeman's model can be described by equation (3.6), where $f$ is the volumetric fraction of the $i_{th}$ phase, $k$ is the composite's thermal conductivity, $k_m$ is the matrix's thermal conductivity, and $k_d$ is the thermal conductivity of the dispersed phase.

For further simplification of Bruggeman's two-phase model, it is assumed that the thermal conductivity of defects/pores is negligible; i.e. $k_d$ = 0. Under the condition of non-radiating pores, equation (3.6) is minimized to:

$$(1-f)^{\frac{3}{2}} = \frac{k}{k_m} \tag{4.1}$$

This equation is applicable, especially when the pores have a spherical shape. The ellipsoid of revolution is the basis for Bruggeman's model. More generally, the Bruggeman's model is an alteration of equation (4.1) for the dispersion of an ellipsoid, written as [102]:

$$\psi(f_1) = (1-f)^X = \frac{k}{k_m} \tag{4.2}$$

where the value of X is dependent on factors such as the ellipsoid's shape factor (F), and $\alpha$ is the angle between the axis of revolution and the heat flux, given by the following equation [102]:

$$X = \frac{1-cos^2\alpha}{1-F} + \frac{cos^2\alpha}{2F} \quad (4.3)$$

The value of X is described as follows: When there are just spherical pores in a continuous matrix, X is assigned to the value of 1.5. Up to a specific temperature limit, the assumption of non-conducting defects/pores is valid. Nevertheless, its primary role is to simplify the model. Realistically, coatings are composed of various types of defects [97]. Thus, the superposition of the impacts of the various types of defects on the overall thermal conductivity is necessary for coatings to be realistically modelled. The two-phase model by Bruggeman can be iterated to higher levels of defects. This method is described extensively in the following paragraphs.

The Bruggeman two-phase model is comprised of spherical pores and a binary mixture of dense material. A two-phase model can be used iteratively to generate a three-phase model for composites. This can be achieved via the following two steps. First, the type 1 porosity is assumed to be embedded in a continuous matrix in order to obtain the average thermal conductivity of a binary mixture. For the second step, the binary mixture is seen as a continuous matrix. At a later stage, a type 2 porosity is embedded into a continuous matrix in a similar process.

If $f_1$ and $f_2$ are the final percentages of type 1 and type 2 porosity, respectively, then the coating's overall porosity can be described by $f_{tot}$, which is the sum of the various types of porosities. Thus, $f_{tot}$=$f_1 + f_2$. In a continuous matrix, there are two ways to add the defects. First, consider that the first type of porosity $f_1$ is embedded into a continuous matrix. Next, consider that

the second type of porosity $f_2$ is embedded into a continuous matrix. This will produce the equation below:

$$\{\phi\left[\frac{f_2}{1-f_1}\right]\psi(f_1)\} \tag{4.4}$$

However, if type 2 porosity is embedded first in the continuous matrix and then type 1 is embedded later, this will produce the following formula:

$$\{\psi\left[\frac{f_1}{1-f_2}\right]\phi(f_2)\} \tag{4.5}$$

The proposed model is an average of the different values of the constituents that make up the composite material. As a result, taking an average of the two possible cases will produce the thermal conductivity of the three-phase mixture as [102]:

$$k = \frac{k_o}{2}\{\psi\left[\frac{f_1}{1-f_2}\right]\phi(f_2) + \phi\left[\frac{f_2}{1-f_1}\right]\psi(f_1)\} \tag{4.6}$$

where $k_o$ is the matrix's thermal conductivity, and the functions $\psi$ and $\phi$ describe the impacts of defects on the coating's thermal conductivity. The averaging technique is another name for this process. The equation is symmetrical about the product of $\psi$ and $\phi$ in order to comply with the dilution process' commutative properties. A unique solution is produced with the help of this property.

To model the different types of defects, spheroids (ellipsoids that have a revolution axis corresponding to the ellipsoid axis '$a$' and whose two other axes are equal, i.e. $b=c$) are selected for the purpose of this thesis. Spheroids can be employed to explain a wide range of real circumstances by defining the revolution angle ($\alpha$) between the dispersed particle and the heat flux and by adjusting the axes ratio $a/c$. Figure 4-1 represents a spheroidal shape. When the ratio between the axes of the spheroid is varied, this shape can be modelled into spheres, lamellas, spheroids, and cylinders.

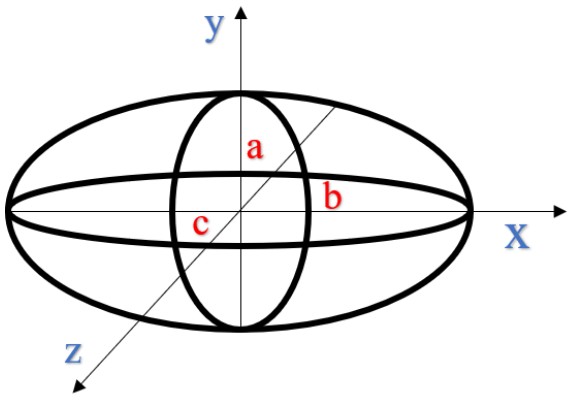


Fig. 4- 1 Representation of spheroidal shape used in modelling defects.

For equation (4.3), the shape factor ($F$) has different values for the various shapes that are being considered. The ratio of axes $a/c$ affects the shape factor ($F$). The software (Fiji Is Just) ImageJ is used to obtain the values of aspect ratios. Figure 4-2 shows a graphical representation of the shape factor ($F$) as a function of aspect ratio $a/c$.

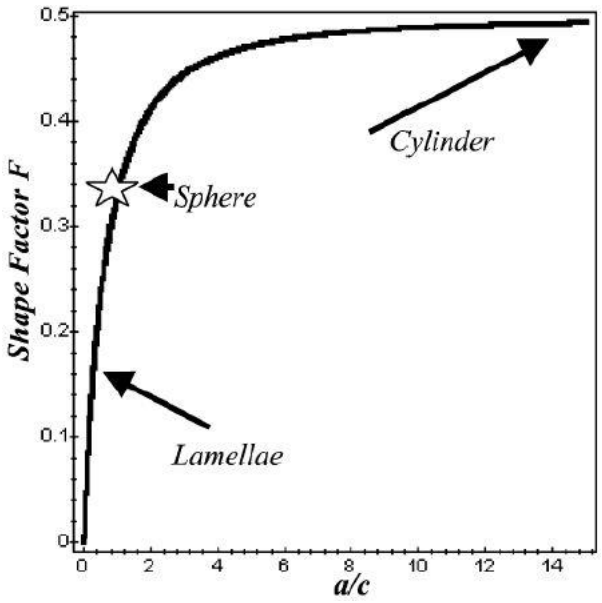


Fig. 4- 2 Shape factor (F) values corresponding to aspect ratio a/c [102].

For defects that are sphere-shaped, this case is considered where the minor and major axis are equal ($a = c$). The value of the shape factor ($F$) is equal to 0.33333. This value corresponds to a sphere-shaped spheroid. When axes $b$ and $c$ are bigger than '$a$' axis (i.e. ($c > a$)), the spheroid is horizontally stretched to form the shape of an oblate spheroid. For oblate pores (lamellas), the shape factor ($F$) falls between 0 and 0.3. When the pores are stretched vertically, a prolate-shaped spheroid is obtained. For prolate pores, the shape factor ($F$) falls between 0.3 and 0.5.

A representation of the graph of the X factor as a function of aspect ratio $a/c$ is presented in Figure 4-3.

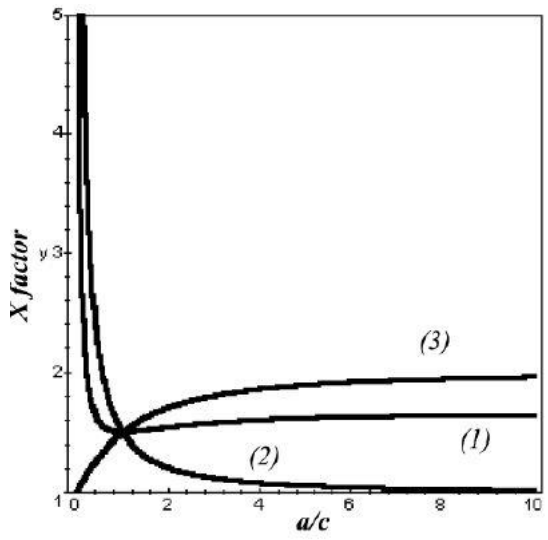


Fig. 4- 3 Relationship between X factor and aspect ratio for various shapes [102].

The curve labelled as (1) is the X factor values for randomly oriented spheroid pores. Curve (2) is the values of the X factor for a spheroid oriented horizontal to the heat flux and with revolution axis '$a$', while curve (3) represents the X factor values for the spheroids oriented vertically to the heat flux and with the revolution axis '$a$'. The point where all three curves meet is the X factor value for a sphere-shaped spheroid. At this point, the value X factor is equal to 3/2, and this corresponds to a value of aspect ratio $a/c$ =1. Figure 4-4 represents the flow process for this model.

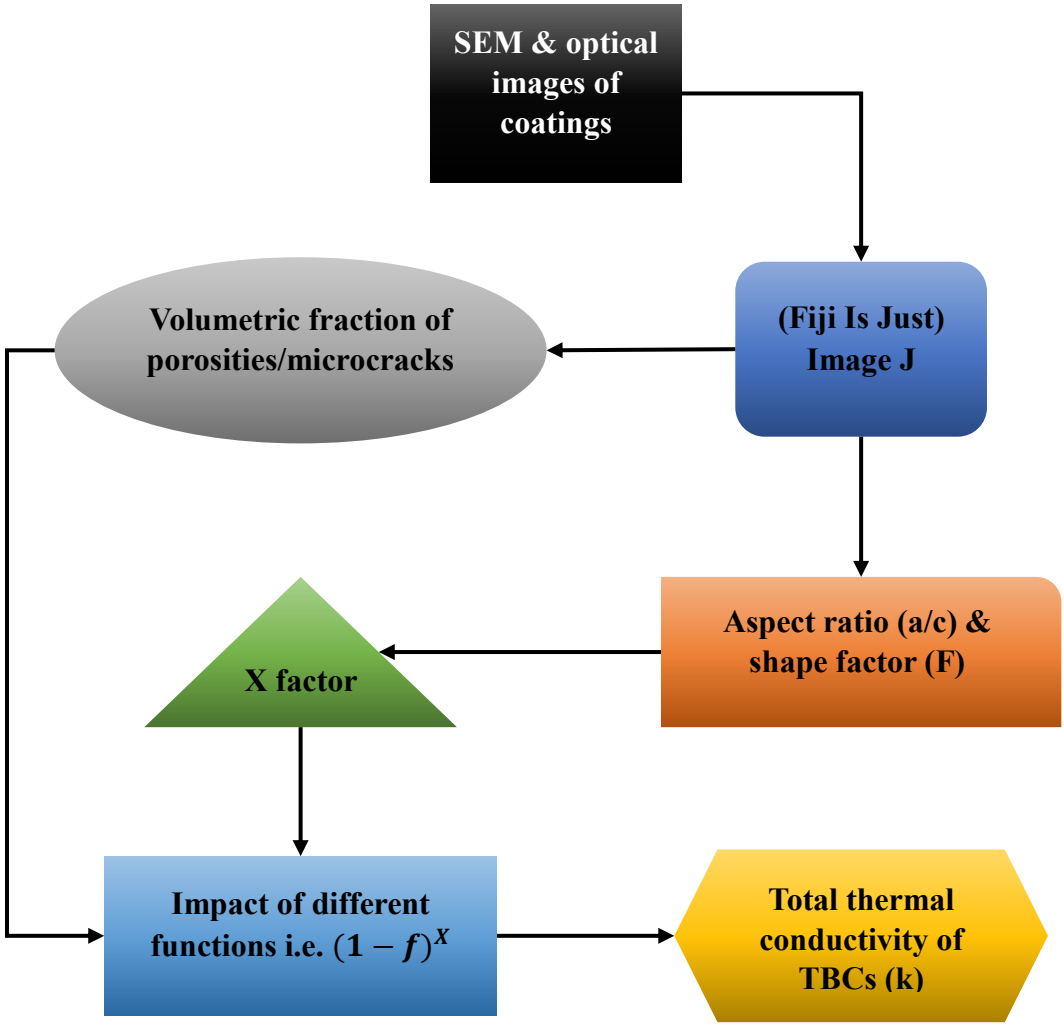


Fig. 4- 4 Flowchart representing the procedure for determining total thermal conductivity of TBCs.

Bruggeman's two-phase model was used as a reference model in this thesis work. A six-phase model was optimized by using iteration (the averaging method). The aim of this thesis work is to improve the analytical model in order to make a better prediction of a ceramic coating's final thermal conductivity by making use of a six-phase mixture. In the modified model that was proposed, it was assumed that five types of defects were added into a continuous matrix. As a result, this model is now a six-phase model for porous composites. It is still assumed that there is no heat transfer within these pores. Thus, $k_d$ = 0 ($k_d$ is the pores' thermal conductivity). The current model's nomenclature is explained in Table 4-1.

Table 4- 1 Nomenclature of the six-phase model.

| | |
|---|---|
| **Spheroid** | Ellipsoid having a revolution axis corresponding to ellipsoid axis a and the other two axes are equal i.e. b=c. |
| **Shape factor (F)** | A numerical value related to the shape of a spheroid. |
| **X factor** | A numerical value considering both orientation and shape of spheroid with respect to heat flux. |
| $\boldsymbol{f_1, f_2, f_3, f_4}$ **and** $\boldsymbol{f_5}$ | Volumetric fraction of porosity corresponding to $\psi, \phi, \theta, \beta$ and $\chi$ respectively. |
| $\boldsymbol{\psi, \phi, \theta, \beta}$ **and** $\boldsymbol{\chi}$ | Functions each describing the impact of various types of porosity on thermal conductivity. |
| $\boldsymbol{k_o}$ | The thermal conductivity of the bulk material. |
| $\boldsymbol{k}$ | The thermal conductivity of the composite material. |

The total porosity ($f_{tot}$) is the sum of contributions from the different types of porosities. Hence, $f_{tot} = f_1 + f_2 + f_3 + f_4 + f_5$. The values of the different functions $\psi, \phi, \theta, \beta,$ and $\chi$ are provided in equation (4.2). The values of the different types of porosities are acquired by image analysis (IA) using (Fiji Is Just) ImageJ. Next, these values are compared to previous works [103], [104], [102], [105].

The proposed iterative method allows for the simultaneous addition of the five various types of defects into a continuous matrix performed by the averaging technique. This leads to the equation of a six-phase porous composite material that has up to 120 equations. Thus, the equation of the six-phase model is separated into five sections in order to understand this better. This

equation is not affected in any way by this process, as all five sections are simply summed to produce the equation. The six-phase model is described by the following equation:

$$k = \frac{k_o}{120}(A + B + C + D + E) \qquad (4.7)$$

Where *A*, *B*, *C*, *D*, and *E* are the five sections of the equation. The formula takes an average of all the possible conditions in which the five kinds of defects can be summed up in various sequences. The values of *A*, *B*, *C*, *D*, and *E* are written as follow:

$$\begin{aligned}
A = \psi\left[\frac{f_1}{1-(f_2+f_3+f_4+f_5)}\right][\,&\phi\left[\frac{f_2}{1-(f_3+f_4+f_5)}\right]\{\theta\left[\frac{f_3}{1-(f_4+f_5)}\right]\left\{\beta\left[\frac{f_4}{1-f_5}\right]\chi(f_5)+\chi\left[\frac{f_5}{1-f_4}\right]\beta(f_4)\right\}\\
&+\beta\left[\frac{f_4}{1-(f_3+f_5)}\right]\left\{\theta\left[\frac{f_3}{1-f_5}\right]\chi(f_5)+\chi\left[\frac{f_5}{1-f_3}\right]\theta(f_3)\right\}+\chi\left[\frac{f_5}{1-(f_3+f_4)}\right]\left\{\theta\left[\frac{f_3}{1-f_4}\right]\beta(f_4)+\beta\left[\frac{f_4}{1-f_3}\right]\theta(f_3)\right\}\}\\
&+\theta\left[\frac{f_3}{1-(f_2+f_4+f_5)}\right]\{\phi\left[\frac{f_2}{1-(f_4+f_5)}\right]\left\{\beta\left[\frac{f_4}{1-f_5}\right]\chi(f_5)+\chi\left[\frac{f_5}{1-f_4}\right]\beta(f_4)\right\}+\beta\left[\frac{f_4}{1-(f_2+f_5)}\right]\left\{\phi\left[\frac{f_2}{1-f_5}\right]\chi(f_5)\right)\\
&+\chi\left[\frac{f_5}{1-f_2}\right]\phi(f_2)\}+\chi\left[\frac{f_5}{1-(f_2+f_4)}\right]\left\{\phi\left[\frac{f_2}{1-f_4}\right]\beta(f_4)+\beta\left[\frac{f_4}{1-f_2}\right]\phi(f_2)\right\}\}\\
&+\beta\left[\frac{f_4}{1-(f_2+f_3+f_5)}\right]\{\phi\left[\frac{f_2}{1-(f_3+f_5)}\right]\left\{\theta\left[\frac{f_3}{1-f_5}\right]\chi(f_5)+\chi\left[\frac{f_5}{1-f_3}\right]\theta(f_3)\right\}\\
&+\theta\left[\frac{f_3}{1-(f_2+f_5)}\right]\left\{\phi\left[\frac{f_2}{1-f_5}\right]\chi(f_5)+\chi\left[\frac{f_5}{1-f_2}\right]\phi(f_2)\right\}+\chi\left[\frac{f_5}{1-(f_2+f_3)}\right]\left\{\phi\left[\frac{f_2}{1-f_3}\right]\theta(f_3)+\theta\left[\frac{f_3}{1-f_2}\right]\phi(f_2)\right\}\}\\
&+\chi\left[\frac{f_5}{1-(f_2+f_3+f_4)}\right]\left\{\phi\left[\frac{f_2}{1-(f_3+f_4)}\right]\left\{\theta\left[\frac{f_3}{1-f_4}\right]\beta(f_4)+\beta\left[\frac{f_4}{1-f_3}\right]\theta(f_3)\right\}\right.\\
&\left.+\theta\left[\frac{f_3}{1-(f_2+f_4)}\right]\left\{\phi\left[\frac{f_2}{1-f_4}\right]\beta(f_4)+\beta\left[\frac{f_4}{1-f_2}\right]\phi(f_2)\right\}+\beta\left[\frac{f_4}{1-(f_2+f_3)}\right]\left\{\phi\left[\frac{f_2}{1-f_3}\right]\theta(f_3)+\theta\left[\frac{f_3}{1-f_2}\right]\phi(f_2)\right\}\right\}]
\end{aligned}$$

$$\begin{aligned}
B = \phi\left[\frac{f_2}{1-(f_1+f_3+f_4+f_5)}\right]\{\psi\left[\frac{f_1}{1-(f_3+f_4+f_5)}\right]\{[\theta\left[\frac{f_3}{1-(f_4+f_5)}\right]\{\beta\left[\frac{f_4}{1-f_5}\right]\chi(f_5)+\chi\left[\frac{f_5}{1-f_4}\right]\beta(f_4)\}]+[\beta\left[\frac{f_4}{1-(f_3+f_5)}\right]\{\theta\left[\frac{f_3}{1-f_5}\right]\chi(f_5)\\
+\chi\left[\frac{f_5}{1-f_3}\right]\theta(f_3)\}]+[\chi\left[\frac{f_5}{1-(f_3+f_4)}\right]\{\theta\left[\frac{f_3}{1-f_4}\right]\beta(f_4)+\beta\left[\frac{f_4}{1-f_3}\right]\theta(f_3)\}]\}\\
+\theta\left[\frac{f_3}{1-(f_1+f_4+f_5)}\right]\{[\psi\left[\frac{f_1}{1-(f_4+f_5)}\right]\{\beta\left[\frac{f_4}{1-f_5}\right]\chi(f_5)+\chi\left[\frac{f_5}{1-f_4}\right]\beta(f_4)\}]+[\beta\left[\frac{f_4}{1-(f_1+f_5)}\right]\{\psi\left[\frac{f_1}{1-f_5}\right]\chi(f_5)\\
+\chi\left[\frac{f_5}{1-f_1}\right]\psi(f_1)\}]+[\chi\left[\frac{f_5}{1-(f_1+f_4)}\right]\{\psi\left[\frac{f_1}{1-f_4}\right]\beta(f_4)+\beta\left[\frac{f_4}{1-f_1}\right]\psi(f_1)\}]\}\\
+\beta\left[\frac{f_4}{1-(f_1+f_3+f_5)}\right]\{[\psi\left[\frac{f_1}{1-(f_3+f_5)}\right]\{\theta\left[\frac{f_3}{1-f_5}\right]\chi(f_5)+\chi\left[\frac{f_5}{1-f_3}\right]\theta(f_3)\}]+[\theta\left[\frac{f_3}{1-(f_1+f_5)}\right]\{\psi\left[\frac{f_1}{1-f_5}\right]\chi(f_5)\\
+\chi\left[\frac{f_5}{1-f_1}\right]\psi(f_1)\}]+[\chi\left[\frac{f_5}{1-(f_1+f_3)}\right]\{\psi\left[\frac{f_1}{1-f_3}\right]\theta(f_3)+\theta\left[\frac{f_3}{1-f_1}\right]\psi(f_1)\}]\}\\
+\chi\left[\frac{f_5}{1-(f_1+f_3+f_4)}\right]\{[\psi\left[\frac{f_1}{1-(f_3+f_4)}\right]\{\theta\left[\frac{f_3}{1-f_4}\right]\beta(f_4)+\beta\left[\frac{f_4}{1-f_3}\right]\theta(f_3)\}]+[\theta\left[\frac{f_3}{1-(f_1+f_4)}\right]\{\psi\left[\frac{f_1}{1-f_4}\right]\beta(f_4)\\
+\beta\left[\frac{f_4}{1-f_1}\right]\psi(f_1)\}]+[\beta\left[\frac{f_4}{1-(f_1+f_3)}\right]\{\psi\left[\frac{f_1}{1-f_3}\right]\theta(f_3)+\theta\left[\frac{f_3}{1-f_1}\right]\psi(f_1)\}]\}\}
\end{aligned}$$

$$C = \theta\left[\frac{f_3}{1-(f_1+f_2+f_4+f_5)}\right]\{\psi\left[\frac{f_1}{1-(f_2+f_4+f_5)}\right]\{[\phi\left[\frac{f_2}{1-(f_4+f_5)}\right]\{\beta\left[\frac{f_4}{1-f_5}\right]\chi(f_5)+\chi\left[\frac{f_5}{1-f_4}\right]\beta(f_4)\}]+[\beta\left[\frac{f_4}{1-(f_2+f_5)}\right]\{\phi\left[\frac{f_2}{1-f_5}\right]\chi(f_5)$$
$$+\chi\left[\frac{f_5}{1-f_2}\right]\phi(f_2)\}]+[\chi\left[\frac{f_5}{1-(f_2+f_4)}\right]\{\phi\left[\frac{f_2}{1-f_4}\right]\beta(f_4)+\beta\left[\frac{f_4}{1-f_2}\right]\phi(f_2)\}]\}$$
$$+\phi\left[\frac{f_2}{1-(f_1+f_4+f_5)}\right]\{[\psi\left[\frac{f_1}{1-(f_4+f_5)}\right]\{\beta\left[\frac{f_4}{1-f_5}\right]\chi(f_5)+\chi\left[\frac{f_5}{1-f_4}\right]\beta(f_4)\}]+[\beta\left[\frac{f_4}{1-(f_1+f_5)}\right]\{\psi\left[\frac{f_1}{1-f_5}\right]\chi(f_5)$$
$$+\chi\left[\frac{f_5}{1-f_1}\right]\psi(f_1)\}]+\chi\left[\frac{f_5}{1-(f_1+f_4)}\right]\{\psi\left[\frac{f_1}{1-f_4}\right]\beta(f_4)+\beta\left[\frac{f_4}{1-f_1}\right]\psi(f_1)\}]\}$$
$$+\beta\left[\frac{f_4}{1-(f_1+f_2+f_5)}\right]\{[\psi\left[\frac{f_1}{1-(f_2+f_5)}\right]\{\phi\left[\frac{f_2}{1-f_5}\right]\chi(f_5)+\chi\left[\frac{f_5}{1-f_2}\right]\phi(f_2)\}]+[\phi\left[\frac{f_2}{1-(f_1+f_5)}\right]\{\psi\left[\frac{f_1}{1-f_5}\right]\chi(f_5)$$
$$+\chi\left[\frac{f_5}{1-f_1}\right]\psi(f_1)\}]+[\chi\left[\frac{f_5}{1-(f_1+f_2)}\right]\{\psi\left[\frac{f_1}{1-f_2}\right]\phi(f_2)+\phi\left[\frac{f_2}{1-f_1}\right]\psi(f_1)\}]\}$$
$$+\chi\left[\frac{f_5}{1-(f_1+f_2+f_4)}\right]\{[\psi\left[\frac{f_1}{1-(f_2+f_4)}\right]\{\phi\left[\frac{f_2}{1-f_4}\right]\beta(f_4)+\beta\left[\frac{f_4}{1-f_2}\right]\phi(f_2)\}]+[\phi\left[\frac{f_2}{1-(f_1+f_4)}\right]\{\psi\left[\frac{f_1}{1-f_4}\right]\beta(f_4)$$
$$+\beta\left[\frac{f_4}{1-f_1}\right]\psi(f_1)\}]+[\beta\left[\frac{f_4}{1-(f_1+f_2)}\right]\{\psi\left[\frac{f_1}{1-f_2}\right]\phi(f_2)+\phi\left[\frac{f_2}{1-f_1}\right]\psi(f_1)\}]\}$$

$$D = \beta\left[\frac{f_4}{1-(f_1+f_2+f_3+f_5)}\right]\{\psi\left[\frac{f_1}{1-(f_2+f_3+f_5)}\right]\{[\phi\left[\frac{f_2}{1-(f_3+f_5)}\right]\{\theta\left[\frac{f_3}{1-f_5}\right]\chi(f_5)+\chi\left[\frac{f_5}{1-f_3}\right]\theta(f_3)\}]+[\theta\left[\frac{f_3}{1-(f_2+f_5)}\right]\{\phi\left[\frac{f_2}{1-f_5}\right]\chi(f_5)$$
$$+\chi\left[\frac{f_5}{1-f_2}\right]\phi(f_2)\}]+[\chi\left[\frac{f_5}{1-(f_2+f_3)}\right]\{\phi\left[\frac{f_2}{1-f_3}\right]\theta(f_3)+\theta\left[\frac{f_3}{1-f_2}\right]\phi(f_2)\}]\}$$
$$+\phi\left[\frac{f_2}{1-(f_1+f_3+f_5)}\right]\{[\psi\left[\frac{f_1}{1-(f_3+f_5)}\right]\{\theta\left[\frac{f_3}{1-f_5}\right]\chi(f_5)+\chi\left[\frac{f_5}{1-f_3}\right]\theta(f_3)\}]+[\theta\left[\frac{f_3}{1-(f_1+f_5)}\right]\{\psi\left[\frac{f_1}{1-f_5}\right]\chi(f_5)$$
$$+\chi\left[\frac{f_5}{1-f_1}\right]\psi(f_1)\}]+[\chi\left[\frac{f_5}{1-(f_1+f_3)}\right]\{\psi\left[\frac{f_1}{1-f_3}\right]\theta(f_3)+\theta\left[\frac{f_3}{1-f_1}\right]\psi(f_1)\}]\}$$
$$+\theta\left[\frac{f_3}{1-(f_1+f_2+f_5)}\right]\{[\psi\left[\frac{f_1}{1-(f_2+f_5)}\right]\{\phi\left[\frac{f_2}{1-f_5}\right]\chi(f_5)+\chi\left[\frac{f_5}{1-f_2}\right]\phi(f_2)\}]+[\phi\left[\frac{f_2}{1-(f_1+f_5)}\right]\{\psi\left[\frac{f_1}{1-f_5}\right]\chi(f_5)$$
$$+\chi\left[\frac{f_5}{1-f_1}\right]\psi(f_1)\}]+[\chi\left[\frac{f_5}{1-(f_1+f_2)}\right]\{\psi\left[\frac{f_1}{1-f_2}\right]\phi(f_2)+\phi\left[\frac{f_2}{1-f_1}\right]\psi(f_1)\}]\}$$
$$+\chi\left[\frac{f_5}{1-(f_1+f_2+f_3)}\right]\{[\psi\left[\frac{f_1}{1-(f_2+f_3)}\right]\{\phi\left[\frac{f_2}{1-f_3}\right]\theta(f_3)+\theta\left[\frac{f_3}{1-f_2}\right]\phi(f_2)\}]+[\phi\left[\frac{f_2}{1-(f_1+f_3)}\right]\{\psi\left[\frac{f_1}{1-f_3}\right]\theta(f_3)$$
$$+\theta\left[\frac{f_3}{1-f_1}\right]\psi(f_1)\}]+[\theta\left[\frac{f_3}{1-(f_1+f_2)}\right]\{\psi\left[\frac{f_1}{1-f_2}\right]\phi(f_2)+\phi\left[\frac{f_2}{1-f_1}\right]\psi(f_1)\}]\}$$

$$E = \chi\left[\frac{f_5}{1-(f_1+f_2+f_3+f_4)}\right]\{\psi\left[\frac{f_1}{1-(f_2+f_3+f_4)}\right]\{[\phi\left[\frac{f_2}{1-(f_3+f_4)}\right]\{\theta\left[\frac{f_3}{1-f\_4)}\right]\beta(f_4)+\beta\left[\frac{f_4}{1-f_3}\right]\theta(f_3)\}]+\theta[\left[\frac{f_3}{1-(f_2+f_4)}\right]\{\phi\left[\frac{f_2}{1-f_4}\right]\beta(f_4)$$
$$+\beta\left[\frac{f_4}{1-f_2}\right]\phi(f_2)\}]+[\beta\left[\frac{f_4}{1-(f_2+f_3)}\right]\{\phi\left[\frac{f_2}{1-f_3}\right]\theta(f_3)+\theta\left[\frac{f_3}{1-f_2}\right]\phi(f_2)\}]\}$$
$$+\phi\left[\frac{f_2}{1-(f_1+f_3+f_4)}\right]\{[\psi\left[\frac{f_1}{1-(f_3+f_4)}\right]\{\theta\left[\frac{f_3}{1-f_4}\right]\beta(f_4)+\beta\left[\frac{f_4}{1-f_3}\right]\theta(f_3)\}]+[\theta\left[\frac{f_3}{1-(f_1+f_4)}\right]\{\psi\left[\frac{f_1}{1-f_4}\right]\beta(f_4)$$
$$+\beta\left[\frac{f_4}{1-f_1}\right]\psi(f_1)\}]+[\beta\left[\frac{f_4}{1-(f_1+f_3)}\right]\{\psi\left[\frac{f_1}{1-f_3}\right]\theta(f_3)+\theta\left[\frac{f_3}{1-f_1}\right]\psi(f_1)\}]\}$$
$$+\theta\left[\frac{f_3}{1-(f_1+f_2+f_4)}\right]\{[\psi\left[\frac{f_1}{1-(f_2+f_4)}\right]\{\phi\left[\frac{f_2}{1-f_4}\right]\beta(f_4)+\beta\left[\frac{f_4}{1-f_2}\right]\phi(f_2)\}]+[\phi\left[\frac{f_2}{1-(f_1+f_4)}\right]\{\psi\left[\frac{f_1}{1-f_4}\right]\beta(f_4)$$
$$+\beta\left[\frac{f_4}{1-f_1}\right]\psi(f_1)\}]+[\beta\left[\frac{f_4}{1-(f_1+f_2)}\right]\{\psi\left[\frac{f_1}{1-f_2}\right]\phi(f_2)+\phi\left[\frac{f_2}{1-f_1}\right]\psi(f_1)\}]\}$$
$$+\beta\left[\frac{f_4}{1-(f_1+f_2+f_3)}\right]\{[\psi\left[\frac{f_1}{1-(f_2+f_3)}\right]\{\phi\left[\frac{f_2}{1-f_3}\right]\theta(f_3)+\theta\left[\frac{f_3}{1-f_2}\right]\phi(f_2)\}]+[\phi\left[\frac{f_2}{1-(f_1+f_3)}\right]\{\psi\left[\frac{f_1}{1-f_3}\right]\theta(f_3)$$
$$+\theta\left[\frac{f_3}{1-f_1}\right]\psi(f_1)\}]+[\theta\left[\frac{f_3}{1-(f_1+f_2)}\right]\{\psi\left[\frac{f_1}{1-f_2}\right]\phi(f_2)+\phi\left[\frac{f_2}{1-f_1}\right]\psi(f_1)\}]\}$$

The six-phase equation was acquired only by taking the average of all the different possibilities of the summation of the defects. Every type of defect has its own X factor and shape factor ($F$). It is important to calculate these factors in order for the proposed model to work in the way that is expected. The following section explains how these calculations are obtained.

## 4.1 Determining different parameters used in the model

The size, shape, and orientation of the different types of defects/porosities affect the six-phase model for porous composite material. It is believed that the overall thermal conductivity is greatly affected by the orientation of the cracks and pores [19]. Different values for the thermal conductivity will be produced even with a slight change in the pores' axes; this also applies to materials with a similar structure [106]. As discussed previously in the section above, the values of X factor depend on the shape that is being considered. This section will discuss how to calculate the various values of X when it comes to different shapes and angles through equation (4.3).

For the model, the first step is to use (Fiji Is Just) ImageJ in order to gather the values of different axes of the defects of SEM and optical images. The shape factor ($F$) is then acquired from Figure 4-2 after having the values of aspect ratios $a/c$. There are different values of shape factor ($F$) depending on the type of shape. (Fiji Is Just) ImageJ is also used to obtain the orientation of the defects. Figure 4-5 shows the angle ($\alpha$), known as the orientation angle, between the revolution axis and the heat flux.

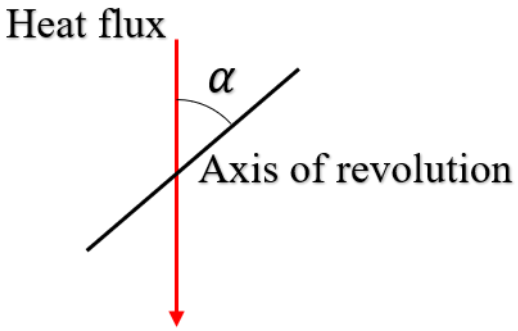


Fig. 4- 5 Representation of the angle of revolution.

The shape factor ($F$) value for the lamellae or the horizontal type of defects ranges from 0 and 0.3. It is clear that from work by Hasselman [136] that the pores which are at a right angle to the direction in which heat flows help to minimize the thermal conductivity in comparison to the pores which are positioned parallel to the direction of heat flux. Consequently, APS-TBC has a lower thermal conductivity than that of EB-PVD TBC because the splat structure (lamellae porosity) of APS coatings contributes to their low heat transfer [107].

Cylindrical defects or vertical defects have a shape factor (F) that ranges from 0.3 to 0.5. The cracks or pores that are more spread out in coatings are represented by the cylindrical shape. A sphere represents the small voids/pores. However, these pores mostly become elongated due to thermal stress and mismatch between the thermal expansion coefficient of various materials during thermal cycling [108].

Presently, the main method of identifying a thermally sprayed deposit microstructure is to evaluate the volumetric fraction of porosity of the coatings' materials. The six-phase model is used to compute the coating's thermal conductivity of porous composites by using equation (4.7). Equation (4.2) is used to define the values of the different functions (i.e. $\psi(f_1)$, $\phi(f_2)$, $\theta(f_3)$, $\beta(f_4)$, and $\chi(f_5)$). Table 4-2 illustrates the equations for each function with respect to their own X factor. The functions utilized on this table derive from equation (4.2).

Table 4- 2 Different equations for different functions in terms of X factor used in modeling.

| Equation illustration for each function | Different functions |
|---|---|
| $(\mathbf{1}-\boldsymbol{f_1})^{\boldsymbol{X_1}}$ | Open randomly oriented pores $\psi(f_1)$ |
| $(\mathbf{1}-\boldsymbol{f_2})^{\boldsymbol{X_2}}$ | Microcracks $\phi(f_2)$ |
| $(\mathbf{1}-\boldsymbol{f_3})^{\boldsymbol{X_3}}$ | Non-flat porosity $\theta(f_3)$ |
| $(\mathbf{1}-\boldsymbol{f_4})^{\boldsymbol{X_4}}$ | Penny-shaped porosity $\beta(f_4)$ |
| $(\mathbf{1}-\boldsymbol{f_5})^{\boldsymbol{X_5}}$ | Interlamellar porosity $\chi(f_5)$ |

In real coatings, only a few voids represent the shape of a sphere as a result of the elongation of the pores and cracks during thermal cycling [108]. Spheroids take into account the majority of the pores and cracks presented in elevated temperature coating materials [96]. Therefore, spheroids can be used to model a wide range of real pores or cracks.

The function $\psi(f_1)$ represents the open randomly oriented porosity. The value of aspect ratio $a/c$ of this kind of porosity is equal to 0.8, which corresponds to the shape factor ($F$) being equal to 0.3. It is assumed that the angle of revolution axis $\alpha$ is equal to $0^{\circ}$. Therefore, the calculated value of X factor equals 1.66 as stated by Schulz [102]. Further, the second type of modelled defects are microcracks. This type of defect is denoted by the function $\phi(f_2)$. The value of the aspect ratio $a/c$ of this type of porosity is equal to 0.07, which corresponds to the shape factor ($F$) being equal to 0.071429. In this case, the angle of revolution axis $\alpha$ is equal to $0^{\circ}$. Thus, the value of X factor is equal to 7 [109].

Additionally, non-flat porosity is the third type of modelled defect which is denoted by the function $\theta(f_3)$. For this type of defect, the value of aspect ratio is equal to 0.7, which corresponds to the shape factor ($F$) being equal to 0.294 with an angle of revolution $\alpha$ being equal to $0^{\circ}$. This leads to the X factor value for non-flat porosity, which is equal to 1.7 [102]. Furthermore, the fourth modelled porosity is penny-shaped. This type of porosity is represented by the function $\beta(f_4)$, and its aspect ratio value is equal to 10, which correlates with a value of shape factor ($F$) being equal to 0.496 with an angle of revolution $\alpha$ being equal to $90^{\circ}$. This gives the value of X=2 [102].

Lastly, interlamellar porosity may be represented by the function $\chi(f_5)$. Its aspect ratio is equal to 0.2 as described elsewhere [85]. The shape factor ($F$) is then obtained from Figure 4-2 that is equal to 0.12. The orientation angle $\alpha$ is $0^{\circ}$. By using equation 4-3, the X factor value was calculated and is equal to 4.16. This value is the model's fitting parameter. It can be concluded that all values of the X factor range from 1 to 10 for various types of pore orientations and shapes.

Table 4- 3 Values of different aspect ratio, shape factor (F) and X factor for each defect shape used in modelling.

| Shape of defect | Functions representation | Aspect ratio (a/c) | Shape factor (F) | X factor |
|---|---|---|---|---|
| **Open randomly oriented porosity** | $\psi(f1)$ | 0.8 | 0.3 | 1.66~ |
| **Microcracks** | $\phi(f2)$ | 0.07 | 0.07 | 7~ |
| **Non flat porosity** | $\theta(f3)$ | 0.7 | 0.294 | 1.7~ |
| **Penny shaped($\alpha = 90^{o}$)** | $\beta(f4)$ | 10 | 0.496 | 2~ |
| **Interlamellar porosity** | $\chi(f5)$ | 0.2 | 0.12 | 4.16# |

~ Obtained value from analysis and treated with the value from the reference.
# Obtained value during research work and treated as a model's fitting parameter.

Table 4-3 demonstrates the values of different aspect ratios $a/c$, shape factors ($F$), and X factors for each type of defect. These values are used in the proposed six-phase model to calculate the thermal conductivity of porous composite materials. These values are considered valid for all the various coating materials modelled in this thesis.

# Chapter 5 TBCs' Microstructural Characterization and Thermal Conductivity

TBC properties are considerably dependent on their microscopic structure and the imperfections of all the components such as cracks, pores, impurities, oxides, and further contaminations. A better consideration of the microstructure of coatings permits for a comprehensive examination of the electrical/dielectric behaviour, mechanical properties, and properties of thermal transport.

In the past, several methods were used to carry out the qualitative and quantitative analysis of the microstructural characteristics of the TBCs [110]. For instance, mercury intrusion porosimetry (MIP) [111], small angle neutron scattering method (SANS) [112], and IA (i.e. the software ImageJ) [113] can examine porosity levels or defects in the coatings. These techniques assist in evaluating the overall porosity in a coating that contains various pore types of various distribution and size. Furthermore, they could surprisingly establish the orientation of small-scale imperfections [114]. Among the above-mentioned techniques, IA has greater reliability for characterizing the microstructure of TBC substrates; as well, IA is considered to be a tool that is both robust and inexpensive [115].

To gather information about the cracks, pores, and additional defects with their orientation, cross-sectional images of the coating can be performed in ImageJ. The experimental instrumentations most frequently used to gain cross-sectional images that are of high quality are light optical microscopy (LOM) [116] along with scanning electron microscopy (SEM) [117].

## 5.1 Principle of image analysis method

Image analysis aims to extract essential details about a coating's microscopic structure. One of the most commonly used software packages developed for the evaluation of the porosity of materials is (Fiji Is Just) ImageJ. During the past three decades, this software has been at the forefront in the field of microstructural characterization. (Fiji Is Just) ImageJ has a simple, user-friendly structure with occasional updates to its plug-ins and tools. Figure 5-1 represents the structure of (Fiji Is Just) ImageJ. The software has become a modern image processing platform because of its core set of principles.

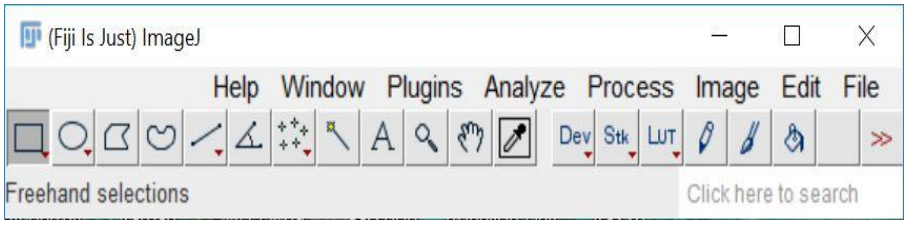


Fig. 5- 1 The menu of (Fiji Is Just) ImageJ software.

In this section, the use of (Fiji Is Just) ImageJ for IA (National Institute of Health (NIH), USA) is briefly described. A number of images are required besides the cross-section of the microstructure in order to capture the changes in the microstructure by IA methods. These digital images are made up of many pixels. These pixels are merely minute dots sequentially linked to one another to produce an output (image). (Fiji Is Just) ImageJ converts these images into a binary format. The data are affected by the magnification of the images. To obtain general information about the microstructure of coating, the magnification of images is set to a particular value. If the magnification value is too high, this will result in the loss of global data. On the other hand, if the magnification is too low, this will result in the depletion of even the smallest details about the

microscopic structure. Factors such as the location from where the image is captured, contrast, brightness, and operating mode can introduce error to the data.

Moreover, binary images and grey-scale images are the two types of images which (Fiji Is Just) ImageJ can analyze. The function of the software is to convert digital coloured images to grey-scale images. The value of defects or pores in the image can be represented by the threshold levels. The adjustment of the image scale is based on the magnification of the image. The details of each crack and pore can be gathered, and the conversion of raw data into numbers is also possible. The percentage area column provides the results for porosity. More information including average pore size, total area, solidity, circularity, Feret angle, and Feret diameter (a measure of an object size along a specified direction) can be obtained from this software.

## 5.2 Results and discussions

### 5.2.1 Microstructural investigation and porosity analysis

Before measuring the thermal conductivity of porous materials, characterizing the porosity of several coating materials was extensively investigated by (Fiji Is Just) ImageJ software. SEM and optical micrographs were collected from different references [103], [104], [67], [105]. The following coating materials are used in this thesis: strontium zirconate ($SrZrO_3$), yttria partially-stabilized zirconia (YPSZ) $8Y_2O_3 - ZrO_2$, magnesia-stabilized zirconia (MSZ) $22MgO - ZrO_2$, ceria-stabilized zirconia (CSZ) $25CeO_2 - 2.5Y_2O_3 - ZrO_2$, and three different powder coatings of yttria stabilized zirconia (YSZ), namely hollo sphere (HOSP), fused and crushed (F&C), and agglomerated and sintered (A&S). One of the powder coating materials (i.e. A&S) was evaluated

at different annealing temperatures for various times and the results yielded different values of thermal conductivity. These values are shown and discussed in Section 5.2.2.

#### 5.2.1.1 Image analysis procedure and results

Generally, five different regions of optical and SEM micrographs for each the as-sprayed and after heat treatment of several coating materials were analyzed by (Fiji Is Just) ImageJ software. The analyses of these five images were then averaged in order to obtain a representative value of porosity. The procedure of these analyses is explained below:

- Images were first converted into an 8bit format in order to apply a threshold criterion.
- The conversion of greyscale micrographs into binary micrographs (i.e. black and white) was implemented by applying the threshold criterion. The porosity was represented by the black pixels, and the white pixels were assigned to the matrix (i.e. ceramics). The threshold level yielded a percentage value, which corresponds to the total porosity value.
- Classification of total porosity to the different porosity shapes was performed on the binary micrographs through the 'opening filter' which only exhibits non-flat porosity and eliminates the remaining types of porosity. Further, microcracks were evaluated by implementing the 'skeletonize filter' which also removes large pores and retains only microcracks. By using 'morphology operation; horizontal & vertical' on a produced image with small pores, the values of both interlamellar (horizontal) and penny-shaped (vertical) porosity were separately extracted and obtained. Next, the threshold criterion was applied in order to acquire the volumetric fractions for each shape. It was difficult to distinguish the content of open randomly-oriented porosity by ImageJ due to a software limitation that has been described elsewhere [115]. Consequently, the remnant value from the total value

of porosity was treated as open randomly-oriented porosity. It is worth mentioning that the procedure explained above was used for and applied to all of the different coating materials studied in this thesis.

For reference, Figure 5-2 presents SEM micrographs of $SrZrO_3$ annealed at 1400 °C for different times.

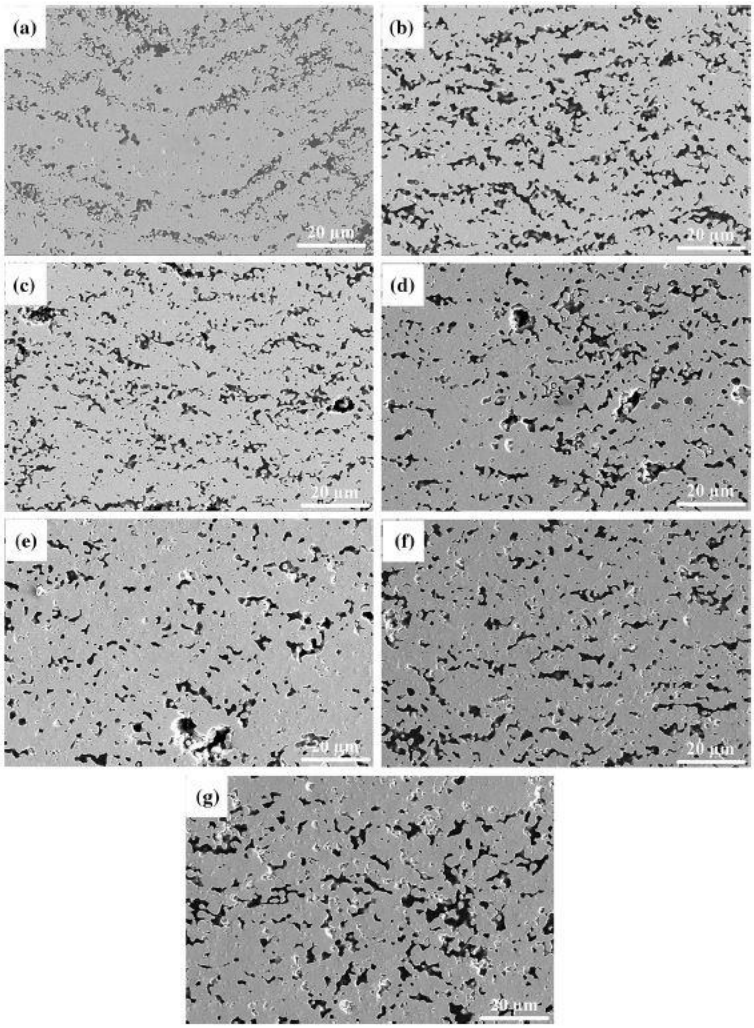


Fig. 5- 2 SEM micrographs of $SrZrO_3$ coating after heat treatment at 1400 °C for different times: (a) 0 h, (b) 5 h, (c) 10 h, (d) 20 h, (e) 100 h, (f) 230 h, and (g) 360 h [103].

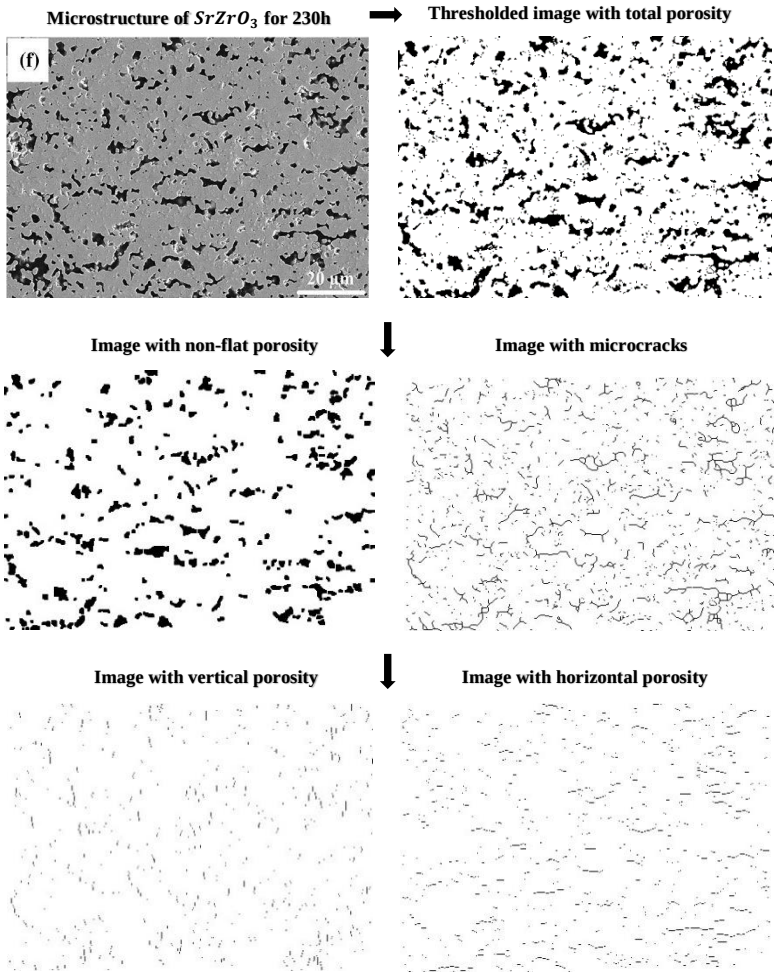


Fig. 5- 3 Sample of (IA) process for segmenting microstructure of defects.

As an example, for the procedure of IA, Figure 5-3 represents an SEM micrograph of $SrZrO_3$ annealed at 1400 °C for 230h. It is evident that the image on the left top corner shows the original greyscale while the top right image represents the binary image with the total porosity. The image located in the left middle is of non-flat porosity, while the image located in the right

middle displays microcrack content. The images positioned in the left and right bottom depict vertical (penny-shaped) and horizontal (interlamellar) porosity, respectively.

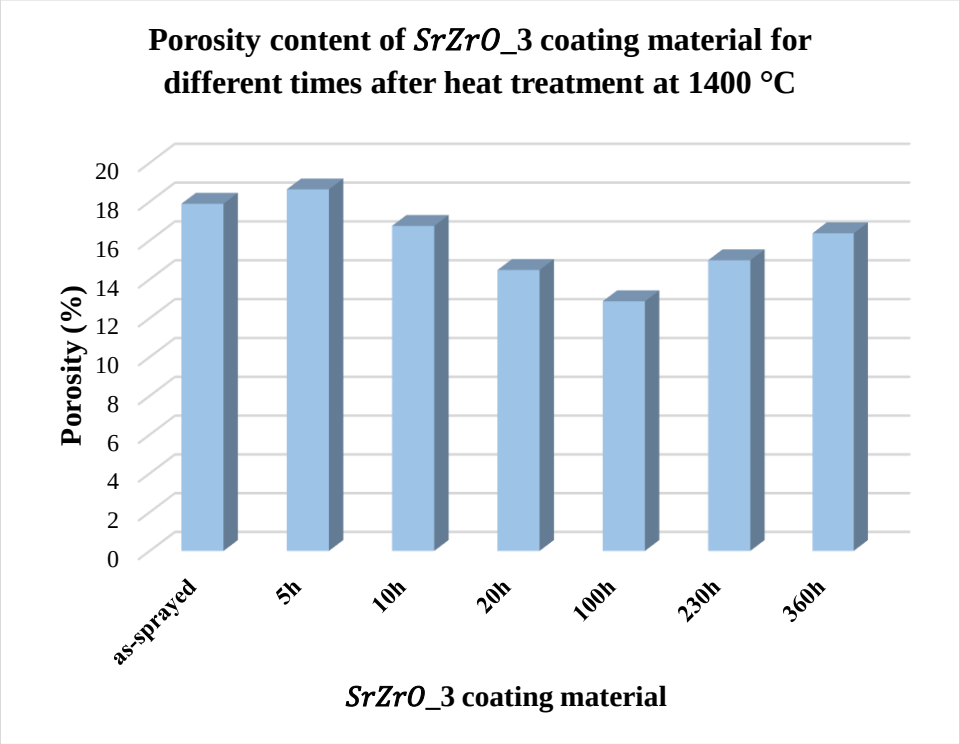


Fig. 5- 4 Porosity of $SrZrO_3$ for different times after heat treatment at 1400 °C performed by (IA).

The total porosity present in $SrZrO_3$ coating sample for several times 0h, 5h, 10h, 20h, 100h, 230h, and 360h of annealing is plotted in Figure 5-4. In general, it can be clearly seen from Figure 5-4 that there was an initial reduction in the total porosity followed by an increase for a long time (i.e. 230h and 360h) of annealing. Further, the total porosity of the as-sprayed coating sample was approximately 17.89% and was then raised moderately to approximately 18.63% for 5h of annealing. Additionally, there was a gradual drop in the overall porosity up to 100h of annealing. In contrast, the observed increase in the total porosity of the annealed coating sample for 230h and 360h may be ascribed to grain pull-out [103].

Table 5-1 demonstrates the total porosity content and its components present in $SrZrO_3$ for several times of annealing. The image results showed that the non-flat porosity was dominated in all the various times of annealing with the highest value of 14.07% in the case of 5h, whereas the content of open randomly oriented porosity seemed to have the minimum values for all of the analyses with the exception of the as-sprayed coating which was higher (2%) in comparison to penny-shaped porosity (1.71%). Also, the content of microcracks was slightly higher than the content of penny-shaped and interlamellar porosity over the annealing times.

Table 5- 1 Porosity content of $SrZrO_3$ coating sample annealed at 1400 °C for different times performed by (IA).

| **Time of heat treatment(h) for $SrZrO_3$ Coating material** | **As-sprayed** | **5** | **10** | **20** | **100** | **230** | **360** |
|---|---|---|---|---|---|---|---|
| **Total porosity (%)** | 17.89 | 18.63 | 16.75 | 14.49 | 12.87 | 14.98 | 16.37 |
| **Open randomly oriented porosity (%)** | 2 | 0.17 | 0.70 | 0.76 | 0.46 | 0.39 | 0.43 |
| **Microcracks (%)** | 2.78 | 1.91 | 2.05 | 1.95 | 1.87 | 1.86 | 2.13 |
| **Non-flat porosity (%)** | 9.4 | 14.07 | 11.18 | 9.02 | 8.64 | 10.44 | 11.05 |
| **Penny-shaped porosity (%)** | 1.71 | 1.09 | 1.12 | 1.15 | 0.83 | 0.93 | 1.23 |
| **Interlamellar porosity (%)** | 2 | 1.73 | 1.70 | 1.61 | 1.07 | 1.36 | 1.53 |

Optical micrographs of various as-sprayed coating samples (i.e. 8YPSZ, 25CSZ, and 22MSZ) are shown in Figure 5-5 and used here for reference.

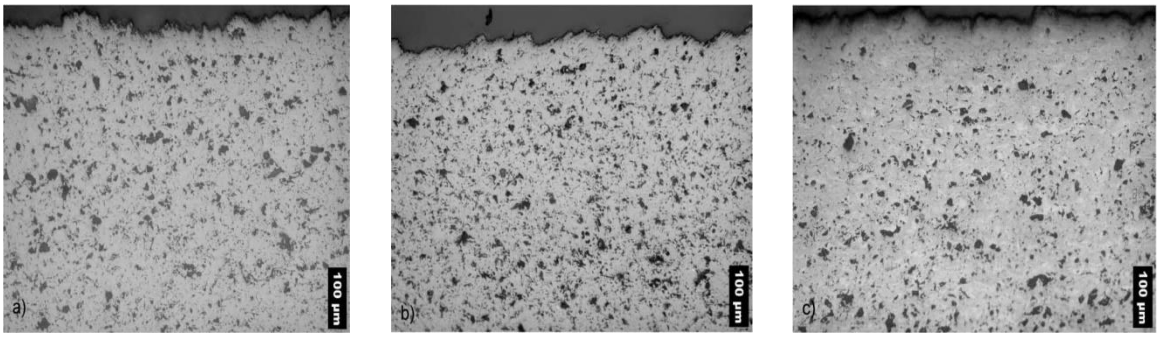


Fig. 5- 5 Optical images of different as-sprayed coating materials: (a) 8YPSZ, (b) 25CSZ and (c) 22MSZ [104].

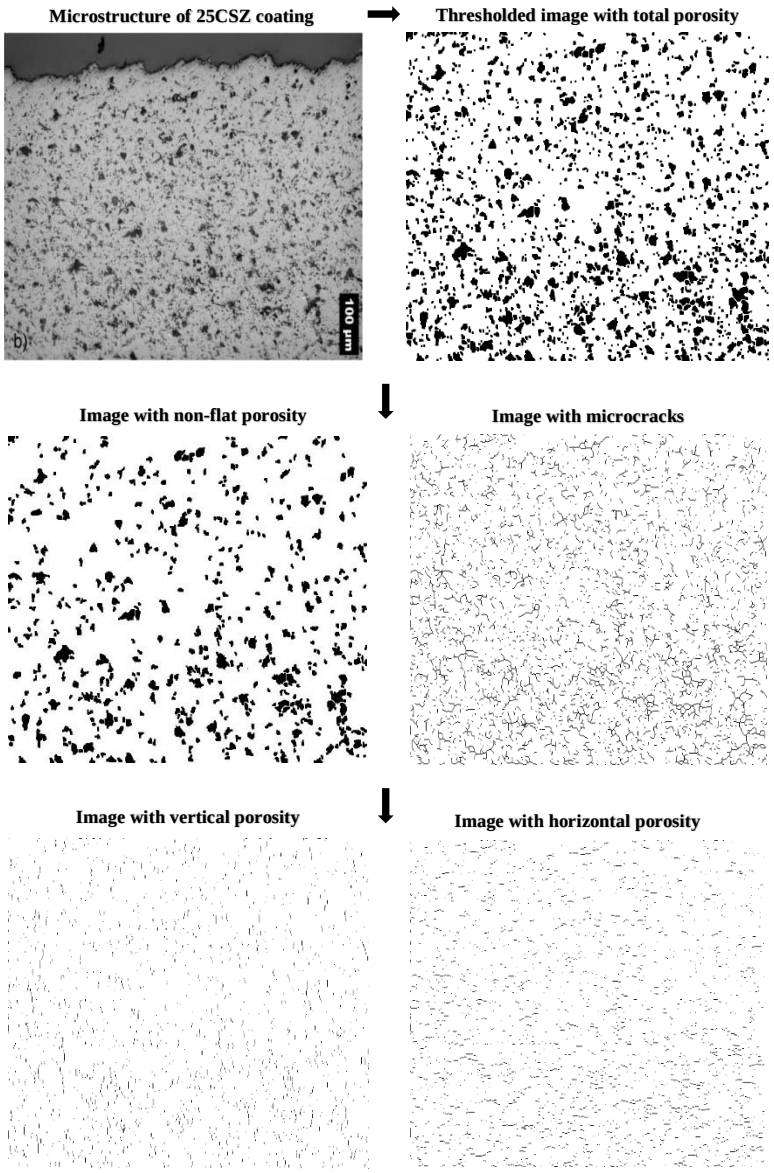


Fig. 5- 6 Sample of (IA) process for segmenting microstructure of defects.

Figure 5-6 displays, as an example, the microstructure of the as-sprayed 25CSZ coating sample with the production of IA process for the different shapes of defects. Signs indicating each type of defect can also be seen in Figure 5-6.

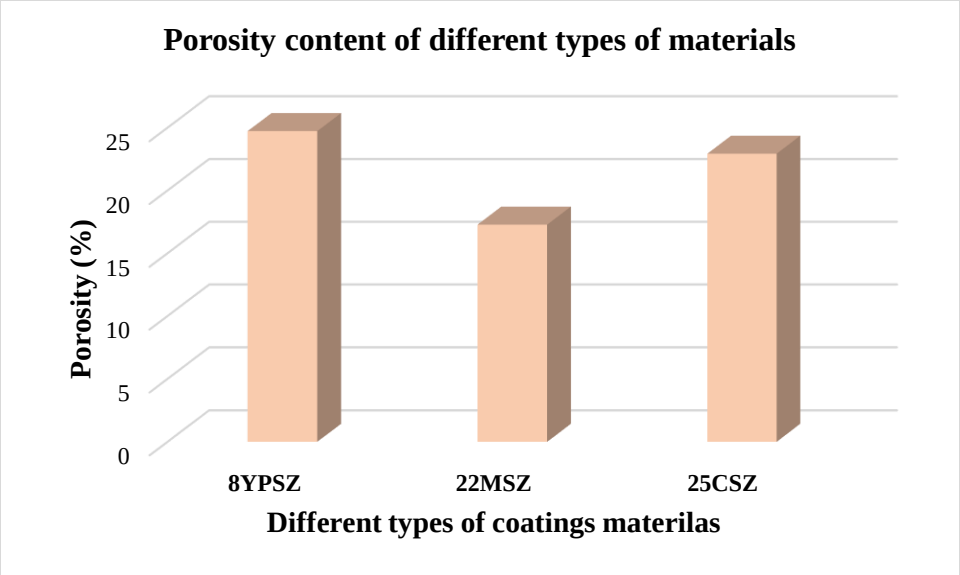


Fig. 5- 7 Porosity measurements of different as-sprayed coating materials performed by (IA).

The overall porosity of several as-sprayed coating samples, namely 8YPSZ, 22MSZ, and 25CSZ, is plotted in Figure 5-7. There was a variation in the overall porosity among the three different types of coating samples. For instance, the porosity percentage appeared to be higher in the case of the 8YPSZ sample with a value of approximately 24.73%. A closer value was obtained for the 25CSZ sample with almost 22.93% of the total porosity, while the obtained porosity value of 22MSZ was the least in comparison to the other coating samples.

Table 5-2 and Figure 5-8 compare the overall porosity and its components of the different as-sprayed coating samples, i.e. 8YPSZ, 22MSZ, and 25CSZ. As stated in the above paragraph, the total porosity of 8YPSZ was the highest with a significant content of non-flat porosity of nearly 18.88% in comparison to the other two coating samples. Microcracks content in both 22MSZ and 25CSZ was observed to have greater values than in the case of 8YPSZ with approximately 4.35% and 4.18%, respectively. Indeed, this study found that these values of microcracks played a crucial

role in the reduction of the thermal conductivity of coating samples. Thermal conductivity evaluations are discussed in the next section.

Table 5- 2 Porosity measurements and its components of as-sprayed 8YPSZ, 22MSZ and 25CSZ coating samples performed by (IA).

| **Sample name** | **8YPSZ** | **22MSZ** | **25CSZ** |
|---|---|---|---|
| **Total porosity (%)** | 24.73 | 17.28 | 22.93 |
| **Open randomly oriented porosity (%)** | 0.28 | 1.27 | 2.58 |
| **Microcracks (%)** | 2.14 | 4.35 | 4.18 |
| **Non-flat porosity (%)** | 18.88 | 9.78 | 12.87 |
| **Penny-shaped porosity (%)** | 1.55 | 0.75 | 1.37 |
| **Interlamellar porosity (%)** | 1.88 | 1.13 | 1.93 |

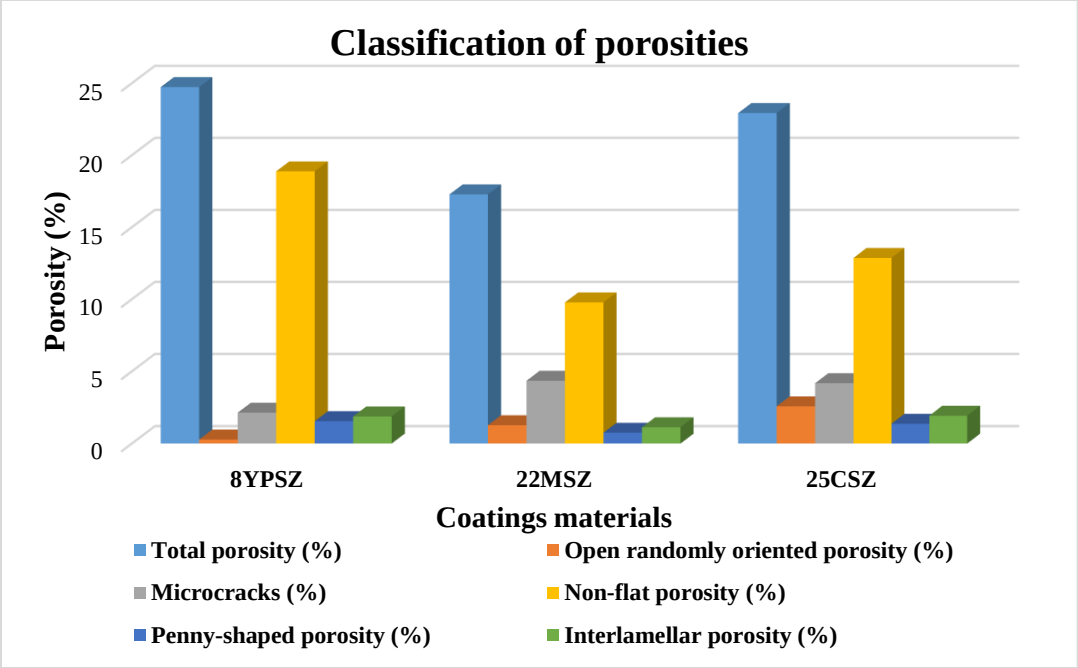


Fig. 5- 8 Classification of porosities present in coating materials.

It is essential to investigate the microstructure and thermal conductivity of a porous TBCs system before and after the heat treatment process. Hence, extensive microstructure analyses and thermal conductivity evaluations of several powder ceramic materials of YSZ (i.e. F&C, A&S, and HOSP) have been carried out. SEM images of the morphology of the as-sprayed and after heat treatment at 1200 °C for 225h are shown in Figure 5-9 and presented here for reference. Figure 5-10 depicts the process employed by IA for segmenting the different classes of defects of F&C powder.

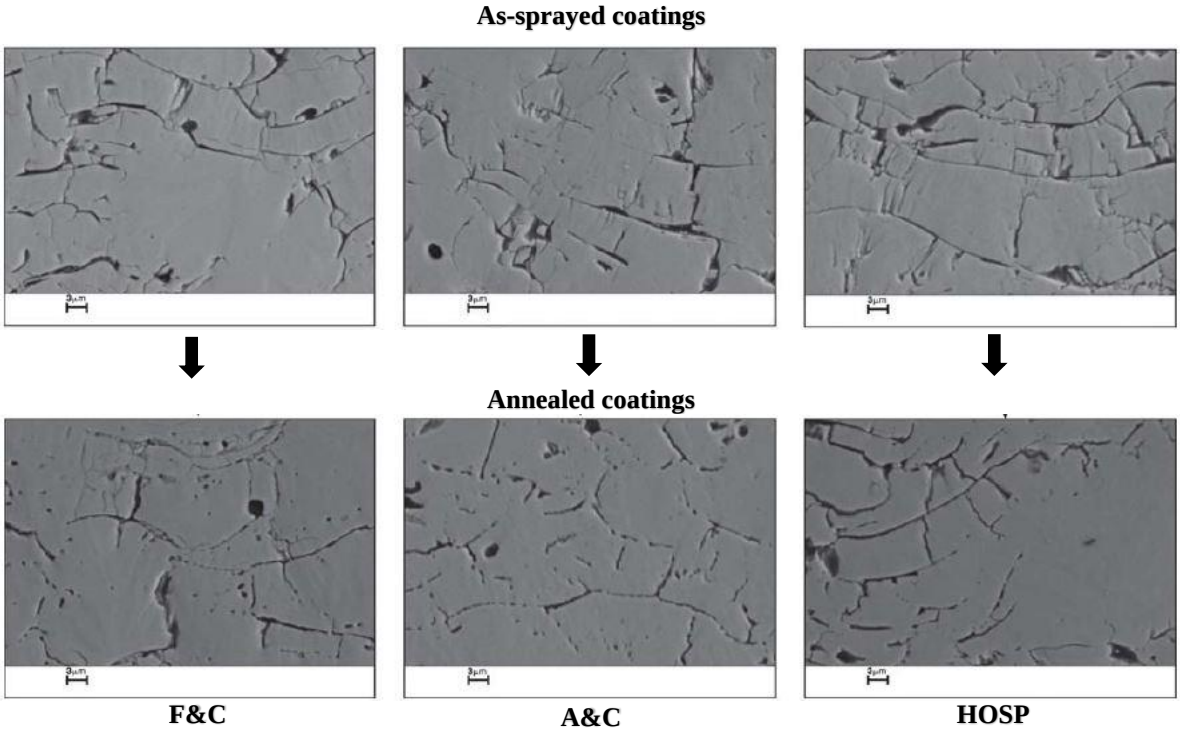

Fig. 5- 9 SEM images of various as-sprayed powder coating materials and annealed at 1200 °C for 225 h [67].

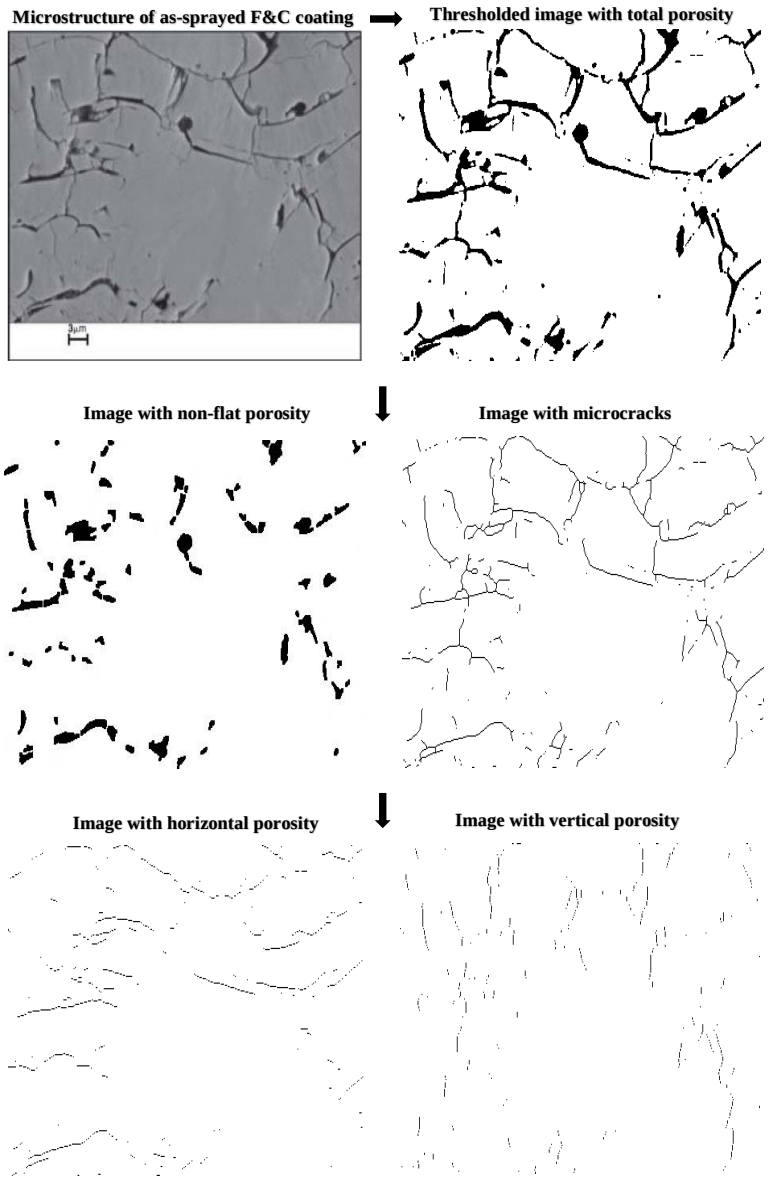


Fig. 5- 10 Sample of (IA) process for segmenting microstructure of defects.

Figure 5-11 shows the plotted results of the overall porosity present in the as-sprayed and heat-treated powder ceramic samples HOSP, F&C, and A&S. For example, the as-sprayed coating HOSP yielded the greatest content of the total porosity in correlation to the other two powder samples. Also, all of the heat-treated samples showed a lower value of porosity in comparison to the as-sprayed samples affecting the thermal properties of the coating materials, as discussed in Section 5.2.2. Changes in microstructure occurred due to the sintering effect taking place during

the annealing process [118]. It is interesting to compare the results of total porosity of heat treated to the as-sprayed materials which were found to range between 4% and 23%.

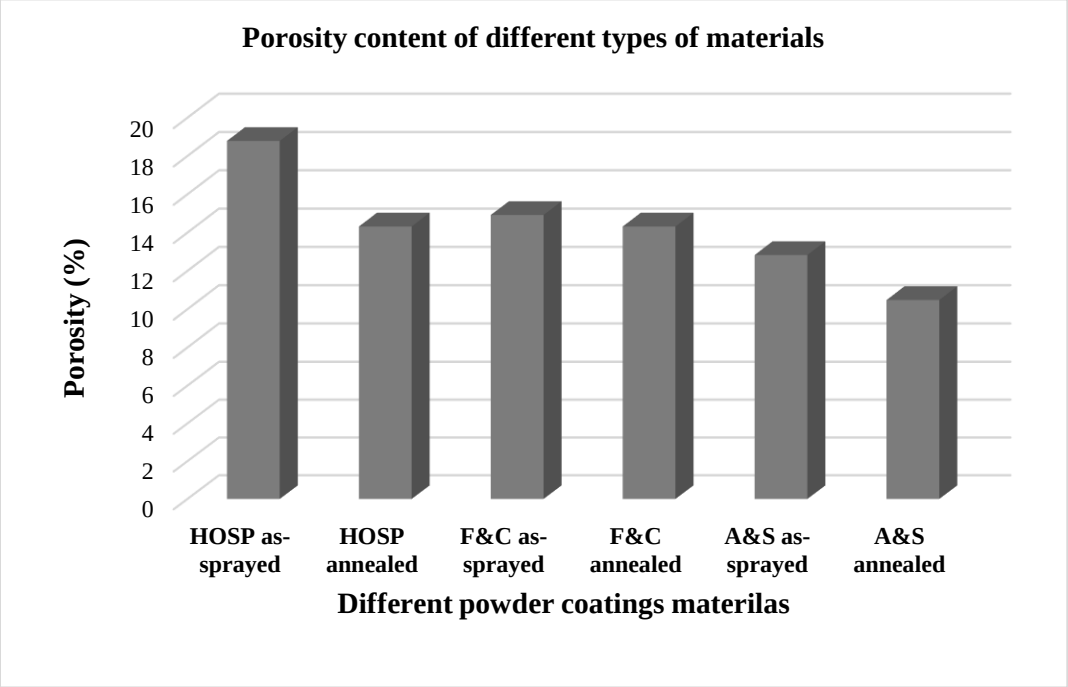


Fig. 5- 11 Porosity measurements of various as sprayed and annealed powder coating materials performed by (IA).

Table 5-3 and Figure 5-12 summarize the results of the different categories of porosity observed in the three powder coating materials. It can be seen from these data that the content of non-flat porosity was not very affected by the annealing process; furthermore, some of the values remained almost stable. On the other hand, tiny defects such as open randomly-oriented, penny-shaped porosity, and microcracks were enormously influenced by the annealing process. In particular, the annealing process was shown to have a huge impact on the content of microcracks in the case of HOSP powder coating material with a reduction from 4.76% to 3.01%. It can be concluded that these tiny defects seemed to shrink as a result of the annealing phenomenon.

Table 5- 3 Porosity evaluations of the three as-sprayed and annealed powder coating materials performed by (IA).

| Sample name | HOSP as-sprayed | HOSP annealed | F&C as-sprayed | F&C annealed | A&S as-sprayed | A&S annealed |
|---|---|---|---|---|---|---|
| **Total porosity (%)** | 18.79 | 14.32 | 14.92 | 14.32 | 12.83 | 10.48 |
| **Open randomly oriented porosity (%)** | 1.38 | 0.07 | 0.91 | 1.64 | 1.03 | 0.21 |
| **Microcracks (%)** | 4.76 | 3.01 | 2.97 | 1.25 | 3.31 | 2.82 |
| **Non-flat porosity (%)** | 8.14 | 8.60 | 8.51 | 9.46 | 6.32 | 6.02 |
| **Penny-shaped porosity (%)** | 1.72 | 1.13 | 1.12 | 0.94 | 1.20 | 0.68 |
| **Interlamellar porosity (%)** | 1.79 | 1.51 | 1.41 | 1.03 | 0.97 | 0.75 |

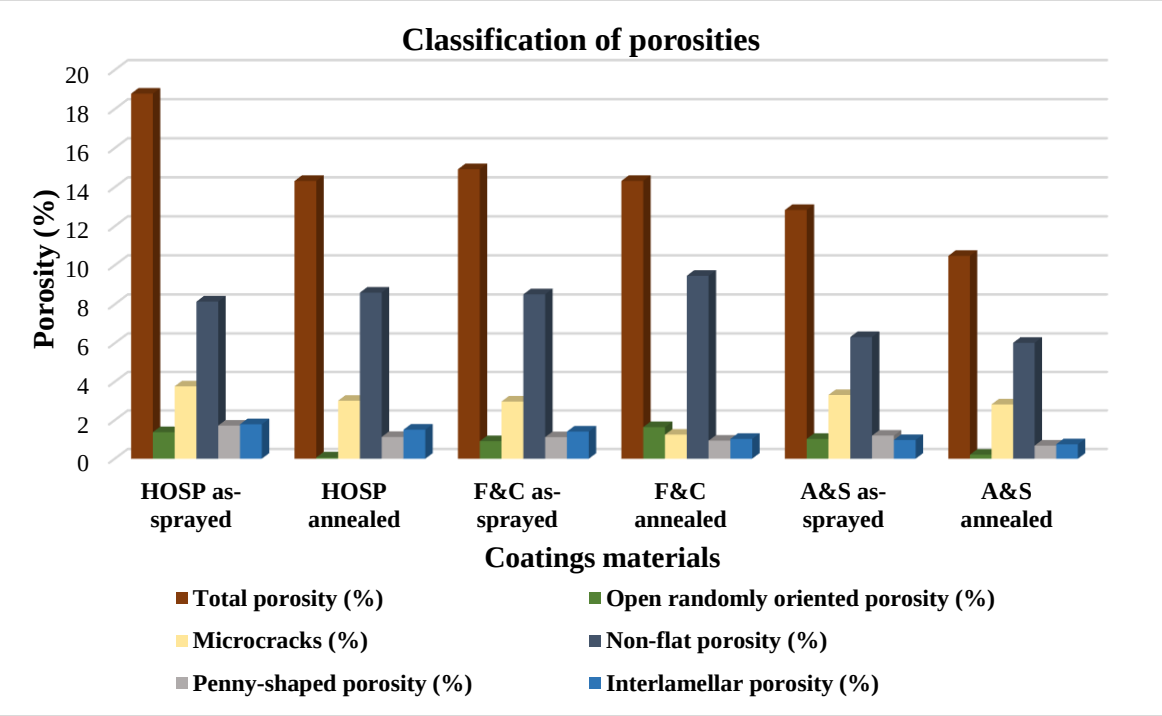


Fig. 5- 12 Classification of porosities present in various powder coating materials.

Further investigations have studied agglomerated and sintered (A&S) powder coating annealed at 1250 °C for various times 5h, 15h, 50h, and 200h. The morphology of this type of powder coating sample is provided in Figure 5-13 and used here for reference. IA outputs for separating the different porosity components of A&S for 200h of the annealing time is shown as an example in Figure 5-14.

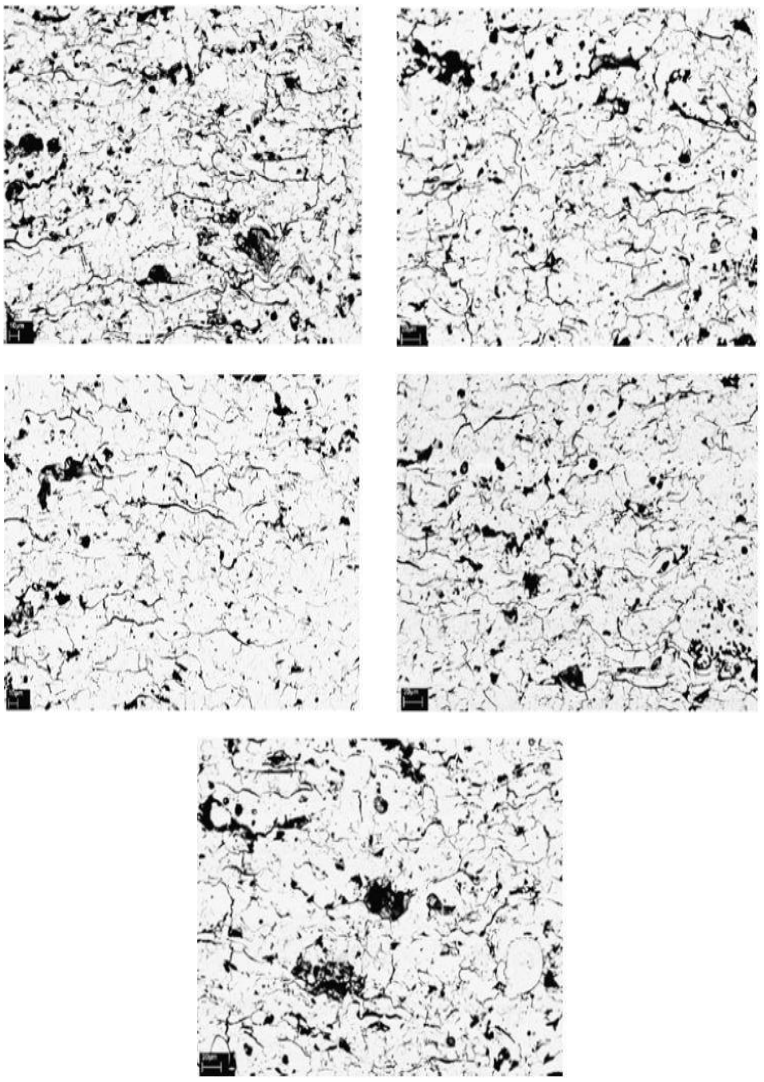

Fig. 5- 13 SEM micrographs of agglomerated and sintered powder annealed at 1250 °C for different times: (a) 0h, (b) 5h, (c) 15h, (d) 50h and (e) 200h [105].

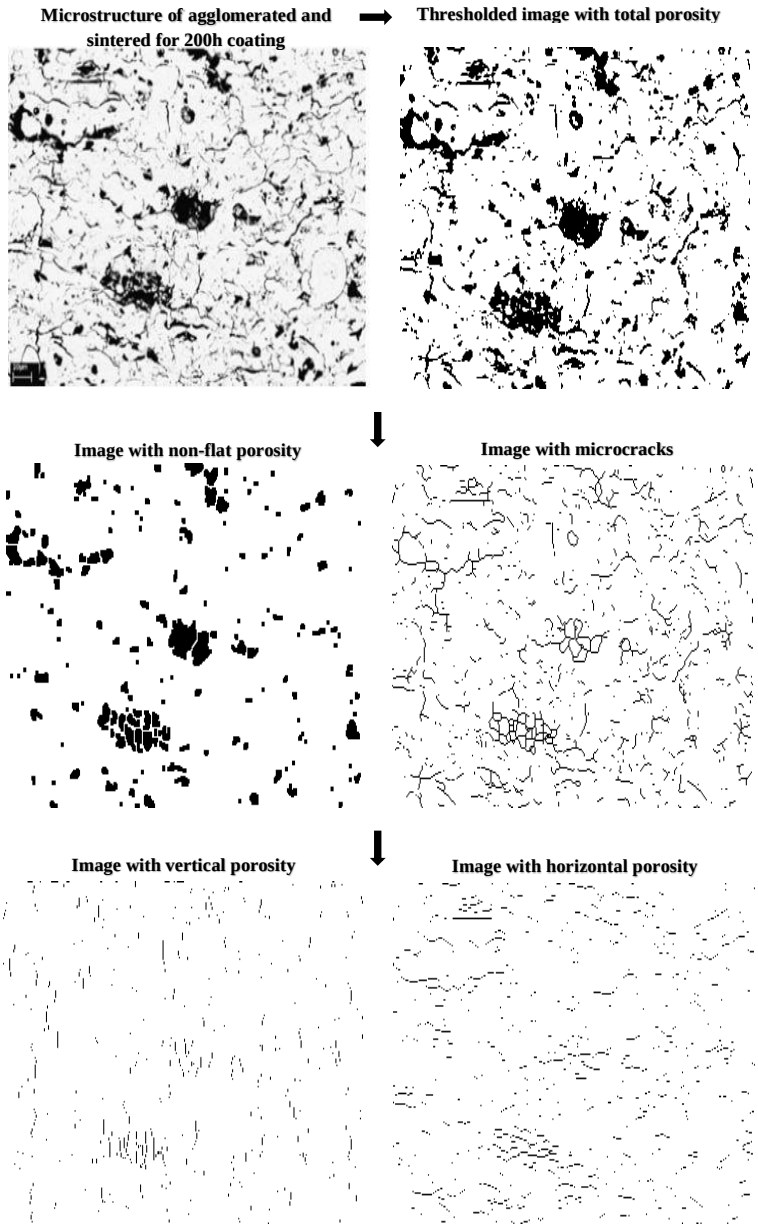


Fig. 5- 14 Sample of (IA) process for segmenting microstruure of defects.

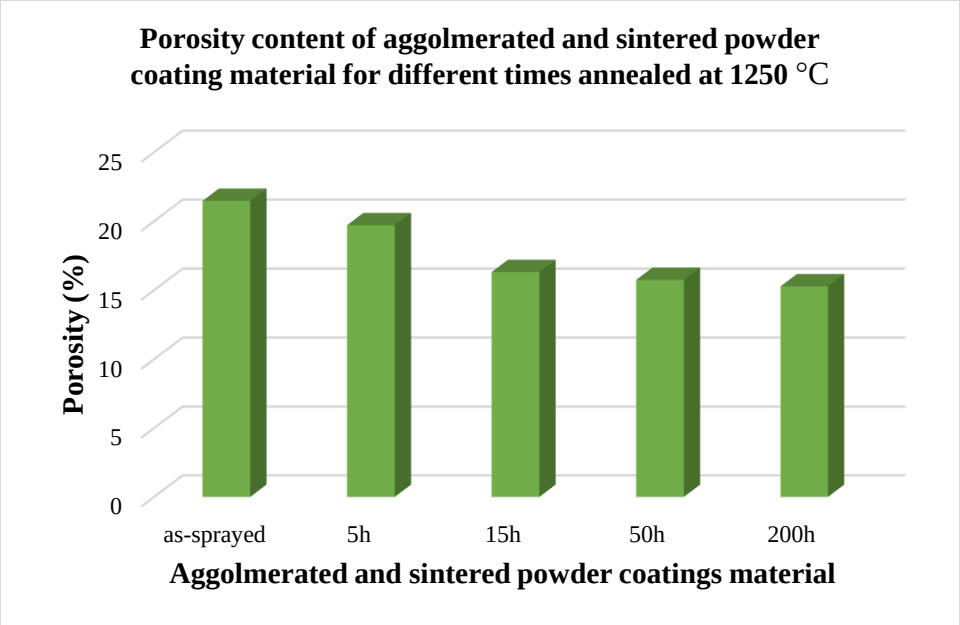


Fig. 5- 15 Porosity measurements of agglomerated and sintered powder coating material annealed at 1250 °C for different times performed by (IA).

Figure 5-15 shows the results calculated for the total porosity of the A&S powder coating sample annealed at 1250 °C for different times. A significant drop in the total porosity was observed after heat treating the sample for 5h to 15h. This was followed by a gradual decrease in the overall porosity up to 200h. It is worth noting that as the annealing time was more prolonged, the total porosity of the coating was slightly reduced.

Table 5- 4 Porosity measurements of agglomerated and sintered powder coating material annealed at 1250 °C performed by (IA).

| **Time of heat treatment(h) for agglomerated and sintered coating material** | **As-sprayed** | **5** | **15** | **50** | **200** |
|---|---|---|---|---|---|
| **Total porosity (%)** | 21.47 | 19.71 | 16.31 | 15.75 | 15.28 |
| **Open randomly oriented porosity (%)** | 3.03 | 4.21 | 3.62 | 3.64 | 1.35 |
| **Microcracks (%)** | 2.52 | 2.79 | 2.67 | 2.64 | 2.12 |
| **Non-flat porosity (%)** | 11.57 | 8.25 | 6.40 | 6.03 | 8.54 |
| **Penny-shaped porosity (%)** | 1.53 | 1.58 | 1.18 | 1.11 | 1.17 |
| **Interlamellar porosity (%)** | 2.82 | 2.88 | 2.44 | 2.33 | 2.10 |

The results obtained for the overall porosity and its constituents of A&S powder coating sample are given on Table 5-4 and in Figure 5-16. As expected, during the annealing time, the value of overall porosity diminished up to 15.28%. This variation was mainly due to the decrease in the content of non-flat porosity with a lesser impact on the other types of porosity. As an exception, the volumetric fraction of open randomly-oriented porosity was greatly influenced for 200h of annealing time. It can be concluded that no remarkable variations were observed in the case of microcracks, penny-shaped, and interlamellar porosity.

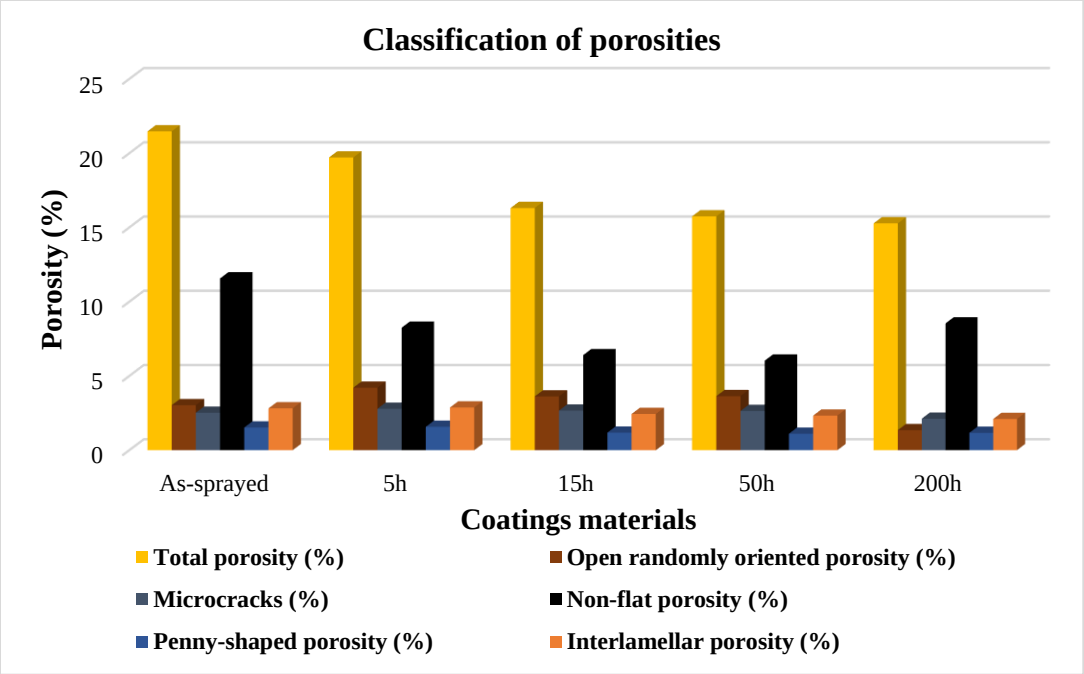


Fig. 5- 16 Classification of porosities present in agglomerated and sintered powder coatings material annealed at 1250 °C for different times performed by (IA).

## 5.2.2 Thermal conductivity evaluations and heat treatment effect

The thermal conductivity of porous TBCs was calculated by the six-phase model (i.e. Equation 4.7). This equation was performed by MATLAB software. MATLAB codes can be found in the Appendix. As previously stated in Section 5.2.1.1, the thermal conductivity of porous TBCs is enormously influenced by the presence of defects in coatings. Thus, the six-phase model has been used to predict the thermal conductivity of porous TBCs based on the microstructure of coating materials.

Moreover, the presence of defects in coatings plays a major role in optimizing the thermal resistance of coating samples. Different shapes and orientation of porosity have various impacts on reducing the thermal conductivity of TBCs [119]. The heat treatment process, considered in this model, is another factor which can affect the thermal conductivity of the TBC systems. The

predicted values are discussed and shown in this section. Furthermore, this section also compares the predicted values of thermal conductivity with earlier published experimental values and FEA model in an attempt to validate the results of the six-phase model. To clarify, the experimental and FEA model's thermal conductivity values were acquired from different references [103], [104], [67], [105].

The predicted and experimental results of the overall thermal conductivity of the as-sprayed and heat-treated $SrZrO_3$ coating material at 1400°C for 5h, 10h, 20, 100, 230h, and 360h are displayed in Table 5-5. The bulk thermal conductivity value of $SrZrO_3$ the sample is 2.08 [W/m K] at 1000°C.

Table 5- 5 Comparison between experimental and predicted thermal conductivity values of $SrZrO_3$ sample (bulk value = 2.08 [W/m K]).

| **$SrZrO_3$ coating material for different times of heat treatment** | **Experimental thermal conductivity [W/m K]** | **Predicted thermal conductivity [W/m K]** |
|---|---|---|
| **As-sprayed** | 1.25 | 1.2 |
| **5h** | 1.2 | 1.235 |
| **10h** | 1.28 | 1.287 |
| **20h** | 1.29 | 1.36 |
| **100h** | 1.31 | 1.43 |
| **230h** | 1.2 | 1.36 |
| **360h** | 1.27 | 1.29 |

These predicted and experimental values of thermal conductivity of $SrZrO_3$ are plotted in Figure 5-17. The blue bars represent the predicted values and the orange bars represent the experimental values. As shown, both the predicted value and the experimental thermal conductivity value increased with further increase in heat treatment time. Although the time of heat treatment was increased to 230h and 360h, both the predicted and experimental thermal conductivity values were reduced. This reduction can be explained by the increase in total porosity

content, which was more likely a result of grain pull-out, as mentioned in Section 5.2.1.1. In general, all results for predicted thermal conductivity were slightly higher than those observed experimentally except the result of the as-sprayed coating, which was lower than the experimental result. To conclude, the obtained modelled results showed good agreement to the experimental results.

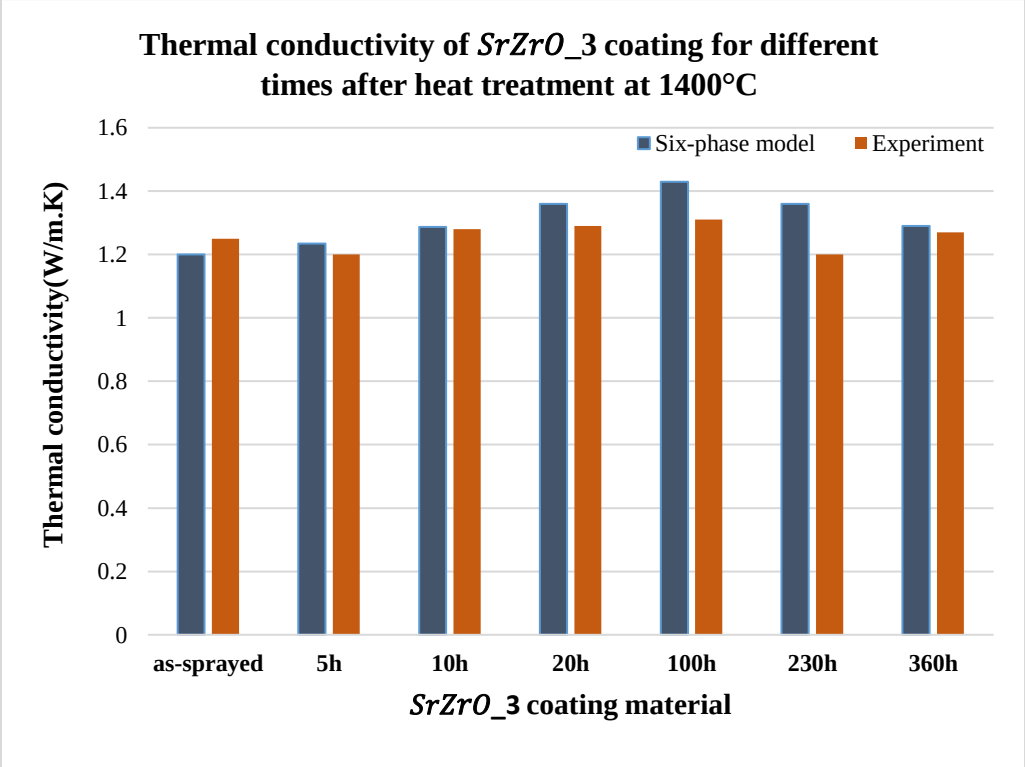


Fig. 5- 17 Comparison of predicted and experimental thermal conductivity of $SrZrO_3$ coating.

The differences between the predicted and experimental values of thermal conductivity of $SrZrO_3$, presented in Table 5-6, ranged between 0.54%-13.3%. The most considerable difference in thermal conductivity was approximately 13.3% for the case of 230h. In contrast, the smallest difference in thermal conductivity was nearly 0.54% for the case of 10h. The negative sign

indicates that the predicted value was less than the experimental value. Overall, the percentage of errors were in an acceptable range of error.

Table 5- 6 Thermal conductivity differences between predicted and experimental values.

| $SrZO\_3$ coating material for different times of heat treatment | Difference between predicted and experimental values of thermal conductivity |
|---|---|
| **As-sprayed** | -4% |
| **5h** | 2.9% |
| **10h** | 0.54% |
| **20h** | 5.4% |
| **100h** | 9.16% |
| **230h** | 13.3% |
| **360h** | 1.57% |

Another comparison was implemented for the results of the calculated and measured the thermal conductivity of three various coating materials: 8YPSZ, 22MSZ, and 25CSZ. This comparison is presented in Table 5-7 and Figure 5-18. The bulk thermal conductivity of 8YPSZ and 25CSZ is 2.8 [W/m K], and the bulk thermal conductivity of 22MSZ is 2.2 [W/m K].

Table 5- 7 Comparison between the experimental and calculated thermal conductivity of three different as-sprayed coating samples 8YPSZ, 22MSZ and 25CSZ (bulk value of 8YPSZ and 25CSZ=2.8 [W/m K] and bulk value of 22MSZ=2.2 [W/m K]).

| Material name | Experimental thermal conductivity [W/m K] | Calculated thermal conductivity [W/m K] |
|---|---|---|
| **8YPSZ** | 1.2 | 1.42 |
| **22MSZ** | 1.1 | 1.19 |
| **25CSZ** | 1.19 | 1.3 |

The calculated thermal conductivity data for the three different coating samples were relatively higher than those experimentally measured. Specifically, the calculated values for coating samples 22MSZ and 25CSZ were closer to the measured values in comparison to the 8YPSZ coating sample. Even though 8YPSZ coating sample yielded a higher content of overall porosity than the two other coating samples, the calculated thermal conductivity data was higher. This higher thermal conductivity may be attributed to the lower content of microcracks as

previously discussed in Section 5.2.1.1. The variation between the calculated and measured data of thermal conductivity may have been caused by imprecise evaluations of microstructural properties due to a software limitation.

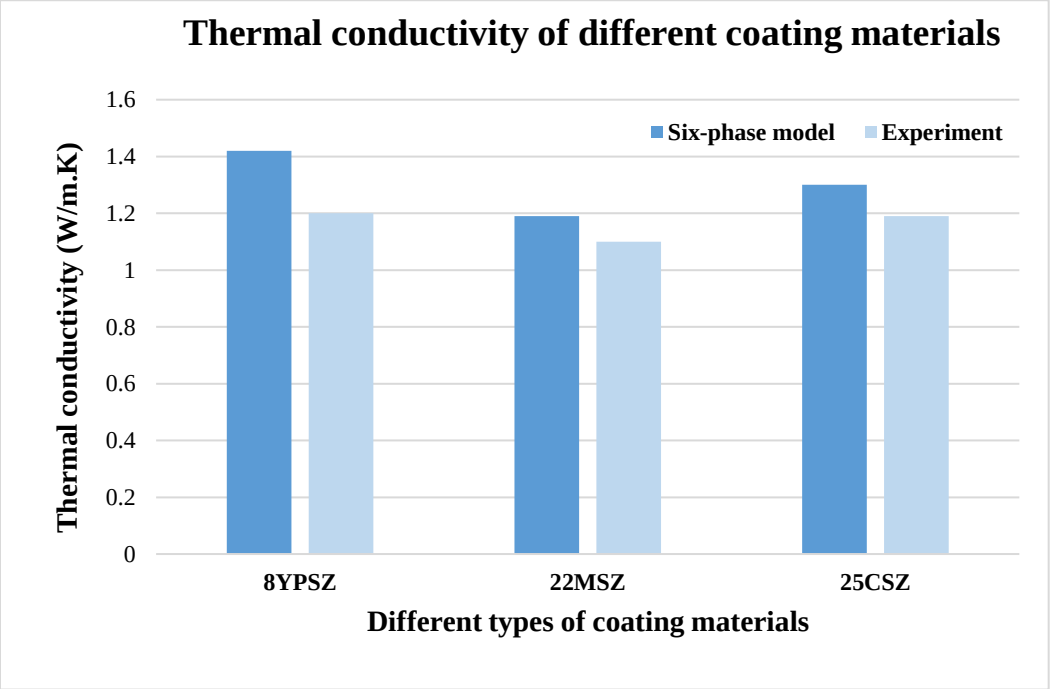


Fig. 5- 18 Comparison of calculated six-phase model and measured thermal conductivity of different coating materials.

A summary of the differences between the calculated and measured values of the thermal conductivity of 8YPSZ, 22MSZ, and 25CSZ is given in Table 5-8. As shown in the table, the most significant difference between the calculated and measured values of thermal conductivity is in the case of 8YPSZ coating sample with a percentage error of approximately 16.6%. The calculated value for 22MSZ coating sample was the lowest with a percentage error of 8%. In general, the modelled results predicted values of thermal conductivity, which are close to the measured values.

Table 5- 8 Thermal conductivity difference between calculated six-phase model and experimental values.

| Sample name | Difference between calculated and measured values of thermal conductivity |
|---|---|
| **8YPSZ** | 16.6% |
| **22MSZ** | 8% |
| **25CSZ** | 9.2% |

Further comparison of the thermal conductivity measurements of three as-sprayed and heat-treated various powder coatings of YSZ, namely HOSP, A&S, and F&C, was made between the computed (six-phase model), experimental, and FEA model results. This comparison is shown in Table 5-9 and Figure 5-19. The bulk value is 2.5 [W/m K].

Table 5- 9 Comparison between experimental, calculated six-phase, and FEA model thermal conductivity values (bulk value = 2.5 [W/m K]).

| Sample name | Experimental thermal conductivity [W/m K] | Six-phase thermal conductivity [W/m K] | FEA thermal conductivity [W/m K] |
|---|---|---|---|
| **HOSP as-sprayed** | 1.1 | 1.28 | 1.32 |
| **HOSP annealed** | 1.3 | 1.54 | 1.44 |
| **F&C as-sprayed** | 1.23 | 1.53 | 1.56 |
| **F&C annealed** | 1.85 | 1.73 | 1.78 |
| **A&S as-sprayed** | 1.12 | 1.59 | 1.75 |
| **A&S annealed** | 1.43 | 1.73 | 1.77 |

The thermal conductivity for the experimental, six-phase model and FEA model were raised after the heat treatment process. As previously stated in Section 5.2.1.1, this increase in thermal conductivity resulted from changes in microstructure due to the sintering effect. It is evident that as the overall porosity content decreased, the thermal conductivity data increased. The thermal conductivity of both the as-sprayed and heat-treated HOSP coating were lower than the other two powder coatings. This result could be ascribed to the hollow spherical structure of this type of powder coating [85]. The predictions for the six-phase model yielded values of thermal

conductivity which were closer than the FEA model results to the experimental values except for the case of heat-treated HOSP and F&C coatings which exhibited higher values than the FEA model.

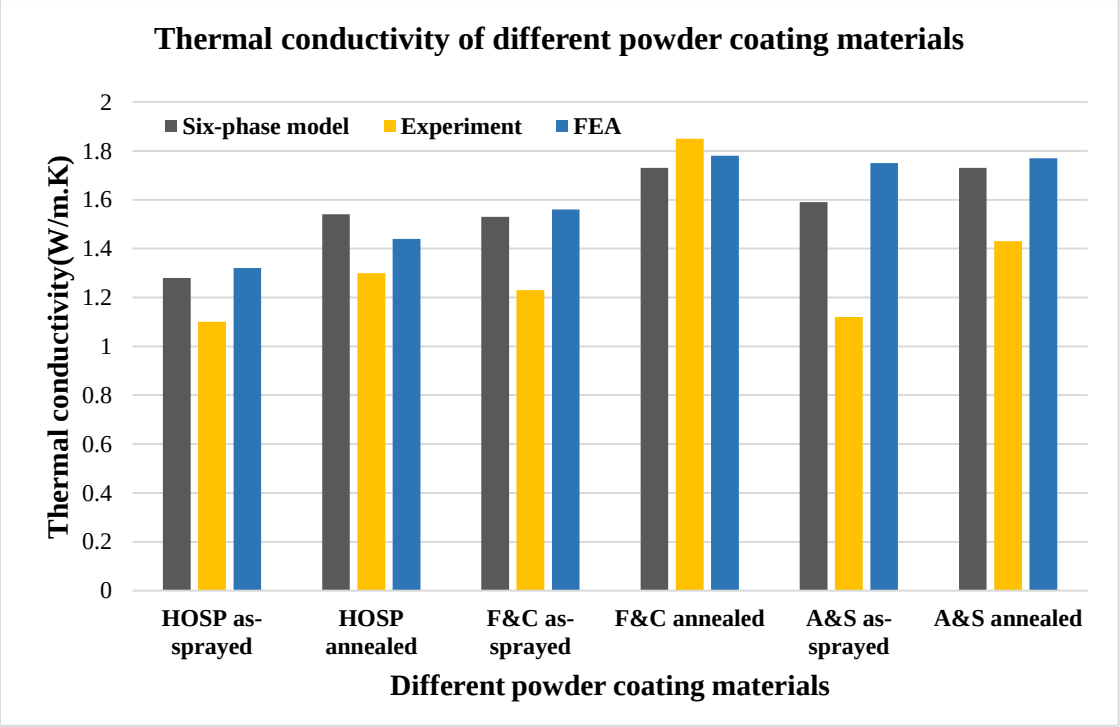


Fig. 5- 19 Comparison of simulated six-phase, FEA models, and experimental thermal conductivity of various powder coating materials.

Table 5-10 illustrates the differences in thermal conductivity values between experimental, six-phase model, and FEA model in the form of percentage error. The maximum difference between experimental and six-phase value was obtained for the as-sprayed A&S sample with 42%. On the other hand, -6% was the minimum difference in the case of heat-treated F&C sample. Further, by comparing the predicted results of the two models, six-phase and FEA, it was found that the maximum difference value was -9%. The negative sign indicates a decrease in the compared values.

Table 5- 10 Thermal conductivity difference between calculated six-phase model, FEA model, and experimental values.

| Sample name | Difference between calculated and experimental values of thermal conductivity | Difference between six-phase and FEA models of thermal conductivity |
|---|---|---|
| **HOSP as-sprayed** | 16% | -3% |
| **HOSP annealed** | 18% | 8% |
| **F&C as-sprayed** | 24% | -2% |
| **F&C annealed** | -6% | -3% |
| **A&S as-sprayed** | 42% | -9% |
| **A&S annealed** | 21% | -2% |

A similar comparison between the computed and measured thermal conductivity of agglomerated and sintered coating material was performed. As mentioned in Section 5.2.1, this powder coating sample was evaluated at a different annealing temperature of 1250°C for 0h, 5h, 15h, 50h, and 200h. The computed results of thermal conductivity, along with the measured data, are reported in Table 5-11 and Figure 5-20.

Table 5- 11 Comparison between the experimental and computed thermal conductivity of agglomerated and sintered sample annealed at 1250 °C for different times.

| Agglomerated and sintered powder coatings | Experimental thermal conductivity [W/m K] | Computed thermal conductivity [W/m K] |
|---|---|---|
| **As-sprayed** | 0.67 | 1.31 |
| **5h** | 1.04 | 1.34 |
| **15h** | 1.16 | 1.47 |
| **50h** | 1.35 | 1.50 |
| **200h** | 1.53 | 1.57 |

The computed results reveal a gradual increase in the thermal conductivity with a further increase in the annealing time as expected because of the decrease in the overall porosity content due to the sintering effect. Similar trends were observed for the measured data. The significant overestimation of the computed results in the case of the as-sprayed coating may have been triggered by the following factors: (1) the connected porosity was not considered; (2) the 2D

microstructure image only provided an approximation of the real 3D microstructure of a coating, as the thermal conductivity is a 3D property; and (3) a software limitation in characterizing the porosity of the material.

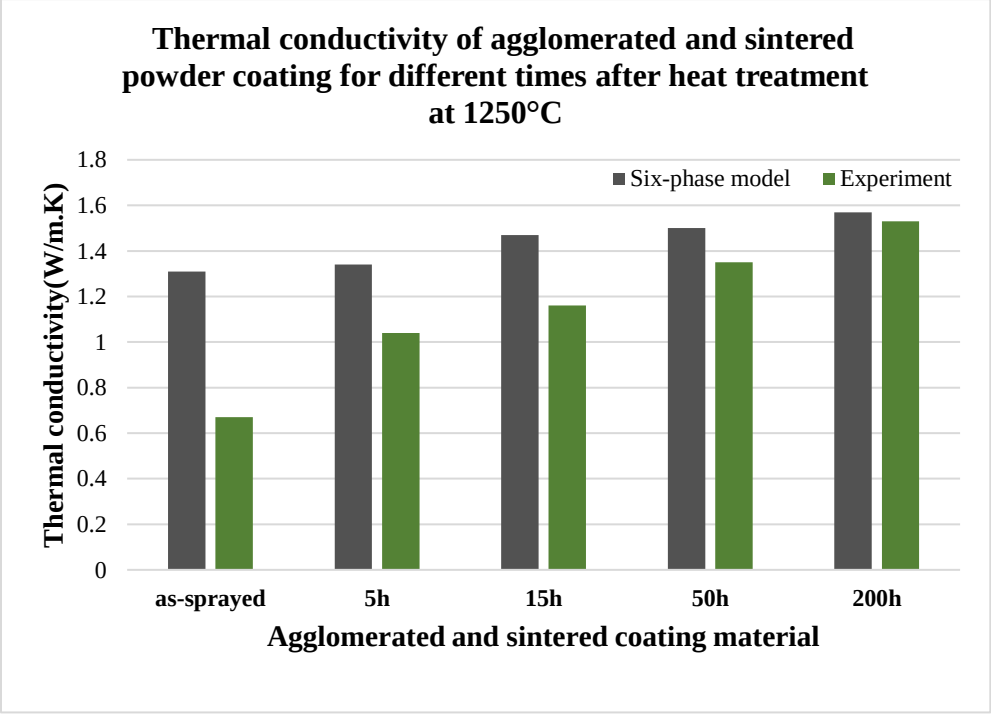


Fig. 5- 20 Comparison of computed six-phase model and measured thermal conductivity of agglomerated and sintered powder coating material annealed at 1250 °C for different times.

The differences in the computed and experimental values of the thermal conductivity of agglomerated and sintered coating annealed at 1250°C for 5h, 15h, 50h, and 200h are reported in Table 5-12. As evident in the table, the computed results show a closer value to the experiment in the case of 200h, which was reported to be approximately 2.6%. In contrast, an enormous difference in the data was recorded in the case of the as-sprayed coating, with approximately 95%. Again, this enormous difference could be due to the factors mentioned in the previous paragraph.

Table 5- 12 Thermal conductivity differences between the computed six-phase model and experimental values.

| Agglomerated and sintered coating material for different times of heat treatment | Difference between computed and experimental values of thermal conductivity |
|---|---|
| **As-sprayed** | 95% |
| **5h** | 28% |
| **15h** | 26% |
| **50h** | 11% |
| **200h** | 2.6% |

# Chapter 6 Conclusion

This thesis work has extended Bruggeman's two-phase model to a six-phase model using an iterative technique to identify the different types of defects (open randomly oriented, non-flat, penny-shaped, interlamellar porosity, and microcracks) present within a TBC. In this thesis, the characterization of the microstructural attributes for various TBC systems has been quantitively investigated using IA approach (i.e. [Fiji is Just] ImageJ). This approach identifies the impact of the various types of porosity on the thermal conductivity of different TBC systems. For example, it has been shown that the presence of microcracks is a prominent factor in optimizing the thermal resistance for all of the TBC materials examined in this thesis.

The drastic increase in thermal conductivity after heating TBCs to high temperatures is based on alterations in the microstructural properties due to the sintering effect. Small defects are greatly influenced by the heat treatment process and tend to vanish, particularly interlamellar, penny-shaped, and non-flat porosity and microcracks.

The predicted results of the six-phase model were compared to experimental and FEA values and showed a good agreement in the obtained data. However, some of the modelled values exhibited a difference in comparison to experimental values. This difference is likely due to (a) a software limitation, or (b) lack of information about the exact microstructure.

To conclude, the modelling approach used in this thesis can reasonably predict values of TBCs' thermal conductivity relatively close to real measured values and FEA data. As a consequence, the proposed six-phase model may be utilized as an effective tool to assess the thermal conductivity of TBCs and manufacture enhanced TBC systems. However, it must be noted that the radiation effect and the effect of connected pores on the thermal conductivity of TBCs

were not included in this model. Thus, this model can be improved by considering these effects. Further, to improve the accuracy and quality of this model, additional investigations of TBCs' microstructure are needed. Such investigations can be achieved by combining the IA technique with other microstructural characterization techniques.

# References


[1] R. C. Reed, *The superalloys fundamentals and applications*. Cambridge University Press, 1742.

[2] A. K. Ray and R. W. Steinbrech, "Crack propagation studies of thermal barrier coatings under bending," *J. Eur. Ceram. Soc.*, vol. 19, no. 12, pp. 2097–2109, 1999.

[3] N. Roy, K. M. Godiwalla, E. S. Dwarakadasa, and A. K. Ray, "Elasto-plastic deformation in thermal barrier coated superalloys," *Scr. Mater.*, vol. 51, no. 7, pp. 739–743, 2004.

[4] A. K. Ray *et al.*, "Fatigue behavior of a thermal barrier coated superalloy at 800 °C," *Mater. Sci. Eng. A*, vol. 448, no. 1–2, pp. 294–298, 2007.

[5] D. R. Clarke and C. G. Levi, "Materials Design for the Next Generation Thermal Barrier Coatings," *Annu. Rev. Mater. Res.*, vol. 33, no. 1, pp. 383–417, 2003.

[6] D. R. Clarke, M. Oechsner, and N. P. Padture, "Thermal-barrier coatings for more efficient gas-turbine engines," *MRS Bull.*, vol. 37, no. 10, pp. 891–898, 2012.

[7] S. Dutta, "Fracture toughness and reliability in high-temperature structural ceramics and composites: Prospects and challenges for the 21st century," *Bull. Mater. Sci.*, vol. 24, no. 2, pp. 117–120, 2001.

[8] R. A. Miller, "Thermal barrier coatings for aircraft engines: History and directions," *J. Therm. Spray Technol.*, vol. 6, no. 1, pp. 35–42, 1997.

[9] J. R. Brandon and R. Taylor, "Thermal properties of ceria and yttria partially stabilized zirconia thermal barrier coatings," *Mater. Sci.*, vol. 40, pp. 143–151, 1989.

[10] Q. M. Yu and Q. He, "Effect of material properties on residual stress distribution in thermal barrier coatings," *Ceram. Int.*, vol. 44, no. 3, pp. 3371–3380, 2018.

[11] L. Wang, Y. Wang, X. G. Sun, J. Q. He, Z. Y. Pan, and C. H. Wang, "A novel structure design towards extremely low thermal conductivity for thermal barrier coatings - Experimental and mathematical study," *Mater. Des.*, 2012.

[12] H. M. Tawancy, A. I. Mohammad, L. M. Al-Hadhrami, H. Dafalla, and F. K. Alyousf, "On the performance and failure mechanism of thermal barrier coating systems used in gas turbine blade applications: Influence of bond coat/superalloy combination," *Eng. Fail. Anal.*, vol. 57, pp. 1–20, 2015.

[13] R. A. Miller, "Current status of thermal barrier coatings - An overview," *Surf. Coatings Technol.*, vol. 30, no. 1, pp. 1–11, 1987.

[14] X. F. Zhang *et al.*, “Enhanced properties of Al-modified EB-PVD 7YSZ thermal barrier coatings,” *Ceram. Int.*, vol. 42, no. 12, pp. 13969–13975, 2016.

[15] N. P. Padture, “Thermal Barrier Coatings for Gas-Turbine Engine Applications,” *Science (80-. ).*, vol. 296, no. 5566, pp. 280–284, 2002.

[16] J. Zhang and V. Desai, “Evaluation of thickness, porosity and pore shape of plasma sprayed TBC by electrochemical impedance spectroscopy,” *Surf. Coatings Technol.*, vol. 190, no. 1, pp. 98–109, 2005.

[17] J. Wang *et al.*, “Effect of spraying power on microstructure and property of nanostructured YSZ thermal barrier coatings,” *J. Alloys Compd.*, vol. 730, pp. 471–482, 2018.

[18] G. R. Li, G. J. Yang, C. X. Li, and C. J. Li, “A comprehensive mechanism for the sintering of plasma-sprayed nanostructured thermal barrier coatings,” *Ceram. Int.*, vol. 43, no. 13, pp. 9600–9615, 2017.

[19] L. Wang *et al.*, “Influence of pores on the thermal insulation behavior of thermal barrier coatings prepared by atmospheric plasma spray,” *Mater. Des.*, vol. 32, no. 1, pp. 36–47, 2011.

[20] J.B Wahl and K. Harris, “Advanced Ni-base superalloys for small gas turbines,” p. 43, 2001.

[21] M. Y. Ali, S. Q. Nusier, and G. M. Newaz, “Creep effects on early damage initiation in a TBC system,” *J. Mater. Sci.*, vol. 39, no. 10, pp. 3383–3390, 2004.

[22] L. Xu, W. Wang, T. Gao, X. Shi, J. Gao, and W. Liang, “Experimental study on cooling performance of a steam-cooled turbine blade with five internal cooling smooth channels,” *Exp. Therm. Fluid Sci.*, vol. 58, pp. 180–187, 2014.

[23] S. Stecura, “Advanced thermal barrier system bond coatings for use on nickel-, cobalt-, and iron-base alloy substrates,” *Thin Solid Films*, vol. 136, pp. 241–256, 1986.

[24] F. Moukalled and R. Y. Nuwayhid, “The Efficiency at Maximum Power Output of a Carnot Engine with Heat Leak,” *Int. J. Mech. Eng. Educ.*, vol. 23, no. 2, pp. 157–165, 2015.

[25] M. Arai, H. Ochiai, and T. Suidzu, “A novel low-thermal-conductivity plasma-sprayed thermal barrier coating controlled by large pores,” *Surf. Coatings Technol.*, vol. 285, pp. 120–127, 2016.

[26] U. Schulz, “Phase Transformation in EB-PVD Yttria Partially Stabilized Zirconia Thermal Barrier Coatings during Annealing,” *J. Am. Ceram. Soc.*, vol. 83, no. 4, pp. 904–910, 2000.

[27] E. International, “Jörn and Roy , Rajkumar ( 2017 ) A study of pulsed thermography for life assessment of thin EB-PVD TBCs undergoing oxidation ageing . NDT and This version is available at https://strathprints.strath.ac.uk/61727/ Strathprints is designed to allow users to ,” pp. 67–74, 2017.

[28] A. C. Fox and T. W. Clyne, “Oxygen transport by gas permeation through the zirconia layer in plasma sprayed thermal barrier coatings,” *Surf. Coatings Technol.*, vol. 184, no. 2–3, pp. 311–321, 2004.

[29] R. Streiff, O. Cerclier, and D. H. Boone, “Structure and hot corrosion behavior of platinum-modified aluminide coatings,” *Surf. Coatings Technol.*, vol. 32, no. 1–4, pp. 111–126, 1987.

[30] K. Ma and J. M. Schoenung, “Isothermal oxidation behavior of cryomilled NiCrAlY bond coat: Homogeneity and growth rate of TGO,” *Surf. Coatings Technol.*, vol. 205, no. 21–22, pp. 5178–5185, 2011.

[31] X. Fang, G. Zhang, and X. Feng, “Performance of TBCs system due to the different thicknesses of top ceramic layer,” *Ceram. Int.*, vol. 41, no. 2, pp. 2840–2846, 2015.

[32] R. G. Wellman, J. R. Nicholls, and K. Murphy, “Effect of microstructure and temperature on the erosion rates and mechanisms of modified EB PVD TBCs,” *Wear*, vol. 267, no. 11, pp. 1927–1934, 2009.

[33] V. Lughi, V. K. Tolpygo, and D. R. Clarke, “Microstructural aspects of the sintering of thermal barrier coatings,” *Mater. Sci. Eng. A*, vol. 368, no. 1–2, pp. 212–221, 2004.

[34] D. R. Mumm and A. G. Evans, “Mechanisms Controlling the Performance and Durability of Thermal Barrier Coatings,” *Key Eng. Mater.*, vol. 197, pp. 199–0, 2009.

[35] A. G. Evans, D. R. Clarke, and C. G. Levi, “The influence of oxides on the performance of advanced gas turbines,” *J. Eur. Ceram. Soc.*, vol. 28, no. 7, pp. 1405–1419, 2008.

[36] V. K. Tolpygo and D. R. Clarke, “Microstructural study of the thêta-alpha transformation in alumina scales formed on nickel-aluminides,” *Mater. High Temp.*, vol. 17, no. 1, pp. 59–70, 2000.

[37] E. Reinhold, P. Botzler, and C. Deus, “EB-PVD process management for highly productive zirconia thermal barrier coating of turbine blades,” *Surf. Coatings Technol.*, vol. 120–121, pp. 77–83, 1999.

[38] D. Zhang, “Thermal barrier coatings prepared by electron beam physical vapor deposition (EB-PVD),” *Therm. Barrier Coatings*, pp. 3–24, 2011.

[39] U. Schulz and M. Schmücker, “Microstructure of ZrO2 thermal barrier coatings applied by EB-PVD,” *Mater. Sci. Eng. A*, vol. 276, no. 1–2, pp. 1–8, 2000.

[40] A. A. Tchizhik, A. I. Rybnikov, I. S. Malashenko, S. A. Leontiev, and A. S. Osyka, “The effect of EB PVD coatings on structure and properties of nickel-base superalloy for gas turbine blades,” *Surf. Coatings Technol.*, vol. 78, no. 1–3, pp. 113–123, 1996.

[41] U. Schulz *et al.*, “Some recent trends in research and technology of advanced thermal barrier coatings,” *Aerosp. Sci. Technol.*, vol. 7, no. 1, pp. 73–80, 2003.

[42] P. Mechnich, W. Braue, and U. Schulz, “High-temperature corrosion of EB-PVD yttria partially stabilized zirconia thermal barrier coatings with an artificial volcanic ash overlay,” *J. Am. Ceram. Soc.*, vol. 94, no. 3, pp. 925–931, 2011.

[43] U. Saral and N. Toplan, “ Thermal cycle properties of plasma sprayed YSZ/Al 2 O 3 thermal barrier coatings ,” *Surf. Eng.*, vol. 25, no. 7, pp. 541–547, 2008.

[44] K. Matsumoto, Y. Itoh, and T. Kameda, “EB-PVD process and thermal properties of hafnia-based thermal barrier coating,” *Sci. Technol. Adv. Mater.*, vol. 4, no. 2, pp. 153–158, 2003.

[45] R. V Hillery, “Thermal Barrier Coating Model Development Final Report,” 2018.

[46] M. Zimbru, M. D’Aniello, A. De Martino, M. Latour, G. Rizzano, and V. Piluso, “Investigation on Friction Features of Dissipative Lap Shear Connections by Means of Experimental and Numerical Tests,” *Open Constr. Build. Technol. J.*, vol. 12, no. 1, pp. 154–169, 2018.

[47] R. McPherson, “A review of microstructure and properties of plasma sprayed ceramic coatings,” *Surf. Coatings Technol.*, vol. 39–40, no. C, pp. 173–181, 1989.

[48] D. Li *et al.*, “Microstructure formed by suspension plasma spraying: From YSZ splat to coating,” *Ceram. Int.*, vol. 43, no. 10, pp. 7488–7496, 2017.

[49] F. Zhang *et al.*, “Application of zirconia thermal barrier coating on the surface of pulling-straightening roller,” *Int. J. Heat Technol.*, vol. 35, no. 4, pp. 765–772, 2017.

[50] H. Berndt, A. Q. Zeng, H. R. Stock, and P. Mayr, “Zirconium carbonitride films produced by plasma-assisted metal organic chemical vapour deposition,” *Surf. Coatings Technol.*, vol. 74–75, no. PART 1, pp. 369–374, 1995.

[51] P. C. Patnaik, X. Huang, and J. Singh, “State of the art and future trends in the development of thermal barrier coating systems,” *Innov. Missile Syst.*, no. May, pp. 38-1-38–20, 2006.

[52] L. Wang *et al.*, “Effect of interface on the thermal conductivity of thermal barrier coatings: A numerical simulation study,” *Int. J. Heat Mass Transf.*, vol. 79, pp. 954–967, 2014.

[53] O. Altun and Y. E. Böke, “The Effect of Pore Shape to the Effective Thermal Conductivity of Thermal Barrier Coatings,” no. January, pp. 449–457, 2009.

[54] R. Vaßen, F. Traeger, and D. Stöver, “Correlation between spraying conditions and microcrack density and their influence on thermal cycling life of thermal barrier coatings,” *J. Therm. Spray Technol.*, vol. 13, no. 3, pp. 396–404, 2004.

[55] R. a Miller and M. A. Kuczmarski, “Method for Measuring Thermal Conductivity of Small Samples Having Very Low Thermal Conductivity,” *Nasa/Tm-2009-215460, E-16681*, vol. Glenn Rese, no. Cleveland, p. Ohio, 2009.

[56] W. Chi, S. Sampath, and H. Wang, “Comparison of the thermal transport property measurements of thermally sprayed coatings by the laser and xenon flash techniques,” *J. Therm. Spray Technol.*, vol. 16, no. 3, pp. 444–448, 2007.

[57] S. R. Casolco, J. Xu, and J. E. Garay, “Transparent/translucent polycrystalline nanostructured yttria stabilized zirconia with varying colors,” *Scr. Mater.*, vol. 58, no. 6, pp. 516–519, 2008.

[58] M. Gupta, N. Curry, P. Nylén, N. Markocsan, and R. Vaßen, “Design of next generation thermal barrier coatings - Experiments and modelling,” *Surf. Coatings Technol.*, vol. 220, pp. 20–26, 2013.

[59] and I. N. U. E. Ya. Litovskii, I. D. Zborovskii, “On the temperature dependence of the thermal conductivity of ceramic materials with rarefraction of the gas medium,” vol. 27, no. 4, pp. 1225–1230, 1974.

[60] W. Chi, “Thermal trnsport properties of thermally sprayed coatings: An integrated study of materials, processing and microstructural effects,” Stony Brook, 2007.

[61] W. Chi, S. Sampath, and H. Wang, “Ambient and high-temperature thermal conductivity of thermal sprayed coatings,” *Proc. Int. Therm. Spray Conf.*, vol. 15, no. December, pp. 773–778, 2006.

[62] K. W. Schlichting, N. P. Padture, and P. G. Klemens, “Thermal conductivity of dense and porous yttria-stabilized zirconia,” *J. Mater. Sci.*, vol. 36, no. 12, pp. 3003–3010, 2001.

[63] P. Pawlowski, L. and Fauchais, “Thermal transport properties of thermally sprayed coatings,” *Int. Mater. Rev.*, vol. 37, no. 1, pp. 271–289, 1992.

[64] I. O. Golosnoy, A. Cipitria, and T. W. Clyne, “Heat transfer through plasma-sprayed thermal barrier coatings in gas turbines: A review of recent work,” *J. Therm. Spray Technol.*, vol. 18, no. 5–6, pp. 809–821, 2009.

[65] S. Gu, T. J. Lu, D. D. Hass, and H. N. G. Wadley, “Thermal conductivity of zirconia coatings with zig-zag pore microstructures,” *Acta Mater.*, vol. 49, no. 13, pp. 2539–2547, 2001.

[66] J. R. Nicholls, K. J. Lawson, A. Johnstone, and D. S. Rickerby, “Methods to reduce the thermal conductivity of EB-PVD TBCs,” *Surf. Coatings Technol.*, vol. 151–152, pp. 383–391, 2002.

[67] Y. Tan, J. P. Longtin, and S. Sampath, “Modeling thermal conductivity of thermal spray coatings: Comparing predictions to experiments,” *Proc. Int. Therm. Spray Conf.*, vol. 15, no. December, pp. 545–552, 2006.

[68] D. S. Almeida, C. R. M. Silva, M. do C. de A. Nono, and C. A. A. Cairo, “Electron Beam-

Physical Vapour Deposition of Zirconia Co-Doped with Yttria and Niobia," *Mater. Sci. Forum*, vol. 498–499, no. c, pp. 453–458, 2005.

[69] S. Raghavan, H. Wang, R. B. Dinwiddie, W. D. Porter, and M. J. Mayo, "The effect of grain size, porosity and yttria content on the thermal conductivity of nanocrystalline zirconia," vol. 39, no. 8, pp. 1119–1125, 1998.

[70] X. Song, M. Xie, F. Zhou, G. Jia, X. Hao, and S. An, "High-temperature thermal properties of yttria fully stabilized zirconia ceramics," *J. Rare Earths*, vol. 29, no. 2, pp. 155–159, 2011.

[71] S. Alprine, M. Derrien, Y. Jaslier, and R. Mavrel, "Thermal barrier coatings: the thermal conductivity challenge," pp. 1–10, 1997.

[72] S. Fabris, A. T. Paxton, and M. W. Finnis, "A stabilization mechanism of zirconia based on oxygen vacancies only," *Acta Mater.*, vol. 50, no. 20, pp. 5171–5178, 2002.

[73] G. Pezzotti, M. C. Munisso, A. A. Porporati, and K. Lessnau, "On the role of oxygen vacancies and lattice strain in the tetragonal to monoclinic transformation in alumina/zirconia composites and improved environmental stability," *Biomaterials*, vol. 31, no. 27, pp. 6901–6908, 2010.

[74] M. Zhao, W. Pan, C. Wan, Z. Qu, Z. Li, and J. Yang, "Defect engineering in development of low thermal conductivity materials: A review," *J. Eur. Ceram. Soc.*, vol. 37, no. 1, pp. 1–13, 2017.

[75] Y. Kobayashi, S. Takahashi, and M. Akoshima, *Microstructure and Thermal Conductivity of Thermal Barrier Coatings*, vol. 29, no. 1. 2015.

[76] H. S. Zhang, S. R. Liao, Y. Wei, and S. K. Guan, "Methods to Reduce Thermal Conductivity Further of Plasma Sprayed Thermal Barrier Coatings," *Adv. Mater. Res.*, vol. 230–232, pp. 49–53, 2011.

[77] Y. A. Tamarin, E. B. Kachanov, and S. V. Zherzdev, "Thermophysical Properties of Ceramic Layers in TBC-EB," *Mater. Sci. Forum*, vol. 251–254, pp. 949–956, 1997.

[78] S. Stecura, "Effects of compositional changes on the performance of a thermal barrier coating system," *3rd Annu. Conf. Coposite Adv. Mater.*, vol. 78976, pp. 1–26, 1979.

[79] J. Singh, D. E. Wolfe, R. A. Miller, J. I. Eldridge, and D. M. Zhu, "Tailored microstructure of zirconia and hafnia-based thermal barrier coatings with low thermal conductivity and high hemispherical reflectance by EB-PVD," *J. Mater. Sci.*, vol. 39, no. 6, pp. 1975–1985, 2004.

[80] P. L. Kapitza , "Heat transfer and superfluidity of helium II," *Phys. Rev.*, vol. 60, pp. 354–355, 1941.

[81] M. Gupta, K. Skogsberg, and P. Nylén, “Influence of topcoat-bondcoat interface roughness on stresses and lifetime in thermal barrier coatings,” *J. Therm. Spray Technol.*, vol. 23, no. 1–2, pp. 170–181, 2014.

[82] L. Liu, H. Zhang, X. Lei, and Y. Zheng, “Dependence of microstructure and thermal conductivity of EB-PVD thermal barrier coatings on the substrate rotation speed,” *Phys. Procedia*, vol. 18, pp. 206–210, 2011.

[83] J. C. Y. Koh and A. Fortini, “Prediction of thermal conductivity and electrical resistivity of porous metalic materials,” *Int. J. Heat Mass Transf.*, vol. 16, pp. 2013–2022, 1973.

[84] R. Gaumé, B. Viana, D. Vivien, J.-P. Roger, and D. Fournier, “A simple model for the prediction of thermal conductivity in pure and doped insulating crystals,” *Appl. Phys. Lett.*, vol. 83, no. 7, pp. 1355–1357, 2003.

[85] A. Kulkarni *et al.*, “Comprehensive microstructural characterization and predictive property modeling of plasma-sprayed zirconia coatings,” *Acta Mater.*, vol. 51, no. 9, pp. 2457–2475, 2003.

[86] and S. A. L. M. Bartsch, U. Schulz, J.-M. Dorvaux, O. Lavigne, E. R. Fuller, “Simulating thermal response of EB-PVD thermal barrier coating microstructures,” *Ceram. Eng. Sci. Proc. 24/3*, pp. 549–554, 2003.

[87] Z. Xu, X. Zhou, R. Mu, and L. He, “Structure, phase stability and thermophysical properties of (Yb 0.1La0.9)2(Zr0.7Ce 0.3)2O7 ceramics,” *Mater. Lett.*, vol. 135, pp. 162–164, 2014.

[88] B. K. Jang, “Thermal conductivity of nanoporous ZrO2-4 mol% Y2O3 multilayer coatings fabricated by EB-PVD,” *Surf. Coatings Technol.*, vol. 202, no. 8, pp. 1568–1573, 2008.

[89] J. C. Maxwell, *A treatise on electricity and magnetism*, 3rd ed. New York: Dover Publications, 1954.

[90] P. G. Klemens, “Effective thermal conductivity of a matrix with two kinds of inclusions,” *Int. J. Thermophys.*, vol. 17, no. 4, pp. 979–981, 1996.

[91] D. P. H. Hasselman, “Effect of cracks on thermal conductivity,” *J. Compos. Mater.*, vol. 12, pp. 403–407, 1978.

[92] D. L. Buchanan and M. H. A. Davis, “Electrical conductivity of dispersion: A review,” *Met. Energy Financ.*, vol. 6, no. 4, pp. 369–385, 1993.

[93] D. A. G. Bruggeman, “Berechnung verschiedener physykalischer Knostanten von heterogenen Substanzen,” *Ann. Phys.*, vol. 24, no. 2, pp. 636–679, 1935.

[94] R. McPherson, “A model for the thermal conductivity of plasma-sprayed ceramic coatings,” *Thin Solid Films*, vol. 112, no. 1, pp. 89–95, 1984.

[95] I. Sevostianov and M. Kachanov, “Anisotropic thermal conductivities of plasma-sprayed thermal barrier coatings in relation to the microstructure,” *J. Therm. Spray Technol.*, vol. 9, no. 4, pp. 478–482, 2000.

[96] T. J. Lu, C. G. Levi, H. N. G. Wadley, and A. G. Evans, “Distributed porosity as a control parameter for oxide thermal barriers made by physical vapor deposition,” *J. Am. Ceram. Soc.*, vol. 84, no. 12, pp. 2937–2946, 2001.

[97] S. Wei, W. Fu-chi, F. Qun-Bo, and M. Zhuang, “Effects of defects on the effective thermal conductivity of thermal barrier coatings,” *Appl. Math. Model.*, vol. 36, no. 5, pp. 1995–2002, 2012.

[98] Y. Dong, C. A. Wang, J. Zhou, and Z. Hong, “A novel way to fabricate highly porous fibrous YSZ ceramics with improved thermal and mechanical properties,” *J. Eur. Ceram. Soc.*, vol. 32, no. 10, pp. 2213–2218, 2012.

[99] L. Wang *et al.*, “Design and optimization of coating structure for the thermal barrier coatings fabricated by atmospheric plasma spraying via finite element method,” *J. Asian Ceram. Soc.*, vol. 2, no. 2, pp. 102–116, 2014.

[100] H. Guo, R. Yao, and L. Zhou, “Plasma-sprayed thermal barrier coatings with segmentation cracks,” *Woodhead Publ.*, pp. 161–174, 2011.

[101] M. Kachanov and I. Sevostianov, “On quantitative characterization of microstructures and effective properties,” *Int. J. Solids Struct.*, vol. 42, no. 2, pp. 309–336, 2005.

[102] F. Cernuschi, S. Ahmaniemi, P. Vuoristo, and T. Mäntylä, “Modelling of thermal conductivity of porous materials: Application to thick thermal barrier coatings,” *J. Eur. Ceram. Soc.*, vol. 24, no. 9, pp. 2657–2667, 2004.

[103] W. Ma *et al.*, “Microstructure and Thermophysical Properties of SrZrO3 Thermal Barrier Coating Prepared by Solution Precursor Plasma Spray,” *J. Therm. Spray Technol.*, vol. 27, no. 7, pp. 1056–1063, 2018.

[104] S. Ahmaniemi, M. Vippola, P. Vuoristo, T. Mäntylä, F. Cernuschi, and L. Lutterotti, “Modified thick thermal barrier coatings: Microstructural characterization,” *J. Eur. Ceram. Soc.*, vol. 24, no. 8, pp. 2247–2258, 2004.

[105] F. Cernuschi, P. G. Bison, S. Marinetti, and P. Scardi, “Thermophysical, mechanical and microstructural characterization of aged free-standing plasma-sprayed zirconia coatings,” *Acta Mater.*, vol. 56, no. 16, pp. 4477–4488, 2008.

[106] P. Scardi, M. Leoni, F. Cernuschi, and A. Figari, “Microstructure and heat transfer phenomena in ceramic thermal barrier coatings,” *J. Am. Ceram. Soc.*, vol. 84, no. 4, pp. 827–835, 2001.

[107] S. Boire-Lavigne, C. Moreau, and R. G. Saint-Jacques, “The relationship between the microstructure and thermal diffusivity of plasma-sprayed tungsten coatings,” *J. Therm. Spray Technol.*, vol. 4, no. 3, pp. 261–267, 1995.

[108] and S. S. S. Rangaswamy, H. Herman, “Thermal expansion study of plasma-sprayed oxide coatings,” *Thin Solid Films*, vol. 73, pp. 43–52, 1980.

[109] R. S. Ghai, K. Chen, and N. Baddour, “Modelling Thermal Conductivity of Porous Thermal Barrier Coatings,” *Coatings*, vol. 9, no. 2, p. 101, 2019.

[110] C.-J. Li and A. Ohmori, “Relationships between the microstructure and properties of thermally sprayed deposits,” *J. Therm. Spray Technol.*, vol. 11, no. 3, pp. 365–374, 2002.

[111] A. B. Abell, K. L. Willis, and D. A. Lange, “Mercury intrusion porosimetry and image analysis of cement-based materials,” *J. Colloid Interface Sci.*, vol. 44, no. 211, pp. 39–44, 1999.

[112] and B. J. G. Zaccai, “Small angle neutron scattering,” *Annu. Rev. Inc*, vol. 12, no. 1, pp. 139–157, 1983.

[113] C. A. Schneider, W. S. Rasband, and K. W. Eliceiri, “NIH Image to ImageJ: 25 years of image analysis.,” *Nat. Methods*, vol. 9, no. 7, pp. 671–5, 2012.

[114] Z. Wang, A. Kulkarni, S. Deshpande, T. Nakamura, and H. Herman, “Effects of pores and interfaces on effective properties of plasma sprayed zirconia coatings,” *Acta Mater.*, vol. 51, no. 18, pp. 5319–5334, 2003.

[115] S. Deshpande, A. Kulkarni, S. Sampath, and H. Herman, “Application of image analysis for characterization of porosity in thermal spray coatings and correlation with small angle neutron scattering,” *Surf. Coatings Technol.*, vol. 187, no. 1, pp. 6–16, 2004.

[116] J. M. Pardal, S. S. M. Tavares, M. da P. C. Fonseca, J. A. de Souza, L. M. Vieira, and H. F. G. de Abreu, “Deleterious phases precipitation on superduplex stainless steel UNS S32750: characterization by light optical and scanning electron microscopy,” *Mater. Res.*, vol. 13, no. 3, pp. 401–407, 2010.

[117] N. M. Yanar, F. S. Pettit, and G. H. Meier, “Failure characteristics during cyclic oxidation of Yttria stabilized zirconia thermal barrier coatings deposited via electron beam physical vapor deposition on platinum aluminide and on NiCoCrAlY bond coats with processing modifications for improved perfo,” *Metall. Mater. Trans. A Phys. Metall. Mater. Sci.*, vol. 37, no. 5, pp. 1563–1580, 2006.

[118] H. J. Rätzer-Scheibe and U. Schulz, “The effects of heat treatment and gas atmosphere on the thermal conductivity of APS and EB-PVD PYSZ thermal barrier coatings,” *Surf. Coatings Technol.*, vol. 201, no. 18, pp. 7880–7888, 2007.

[119] Y. Huang *et al.*, “Effect of different types of pores on thermal conductivity of YSZ thermal barrier coatings,” *Coatings*, vol. 9, no. 2, p. 138, 2019.

# Appendix

The MATLAB codes that have been used for the six-phase model (i.e. Equation 4.7) are provided below:

It should be mentioned that the values given below for `k_o, alfa, F, f_1, f_2, f_3, f_4, and f_5` are changed for each material studied in this thesis and are given here as an example.

```
%% Codes for the six-phase model:
k_o=2.2; % Bulk value of thermal conductivity [W/m.K].
% Equation for X factor at different values of shape factor (F) and angle of
revolution axes:
alfa=90; % Angle of revolution axes.
F=0.496; % Shape factor (calculated from the figure).
X=(1-cos(alfa).^2)./(1-F) + (cos(alfa).^2)./(2.*F);
% Volumetric fraction of defects:
f_1=0.0127;  % open randomly oriented porosity.  f_2=0.0435;  % microcracks.
f_3=0.0978;  % non-flat porosity.                f_4=0.0075;  % penny-shaped porosity.
f_5=0.0113;  % interlamellar porosity.
% X factor values:
X1=1.66;
X2=7;
X3=1.7;
X4=2;
X5=4.16;
% Functions representing the impact of different types of defects:
sai_1=f_1/(1-(f_2+f_3+f_4+f_5));     fai_1=f_2/(1-(f_3+f_4+f_5));
thita_1=f_3/(1-(f_4+f_5));           beta_1=f_4/(1-f_5);
xai_1=f_5;                           xai_2=f_5/(1-f_4);
beta_2=f_4;                          beta_3=f_4/(1-(f_3+f_5));
thita_3=f_3/(1-f_5);                 xai_3=xai_1;
xai_4=f_5/(1-f_3);                   thita_4=f_3;
xai_5=f_5/(1-(f_3+f_4));             thita_5=f_3/(1-f_4);
beta_5=beta_2;                       beta_6=f_4/(1-f_3);
thita_6=thita_4;                     thita_7=f_3/(1-(f_2+f_4+f_5));
fai_7=f_2/(1-(f_4+f_5));             beta_7=beta_1;
xai_7=xai_1;                         xai_8=xai_2;
beta_8=beta_2;                       beta_9=f_4/(1-(f_2+f_5));
fai_9=f_2/(1-f_5);                   xai_9=xai_1;
xai_10=f_5/(1-f_2);                  fai_10=f_2;
xai_11=f_5/(1-(f_2+f_4));            fai_11=f_2/(1-f_4);
beta_11=beta_2;                      beta_12=f_4/(1-f_2);
fai_12=fai_10;                       beta_13=f_4/(1-(f_2+f_3+f_5));
fai_13=f_2/(1-(f_3+f_5));            thita_13=f_3/(1-f_5);
xai_13=xai_1;                        xai_14=f_5/(1-f_3);
thita_14=thita_4;                    thita_15=f_3/(1-(f_2+f_5));
fai_15=fai_9;                        xai_15=xai_1;
xai_16=xai_10;                       fai_16=fai_10;
xai_17=f_5/(1-(f_2+f_3));            fai_17=f_2/(1-f_3);
thita_17=thita_4;                    thita_18=f_3/(1-f_2);
```

```
fai_18=fai_10;
fai_19=f_2/(1-(f_3+f_4));
beta_19=beta_2;
thita_20=thita_4;
fai_21=fai_11;
beta_22=beta_12;
beta_23=f_4/(1-(f_2+f_3));
thita_23=thita_4;
fai_24=fai_10;
sai_25=f_1/(1-(f_3+f_4+f_5));
beta_25=beta_1;
xai_26=xai_2;
beta_27=beta_3;
xai_27=xai_3;
thita_28=thita_4;
thita_29=thita_5;
beta_30=beta_6;
thita_31=f_3/(1-(f_1+f_4+f_5));
beta_31=beta_7;
xai_32=xai_8;
beta_33=f_4/(1-(f_1+f_5));
xai_33=xai_1;
sai_34=f_1;
sai_35=f_1/(1-f_4);
beta_36=f_4/(1-f_1);
beta_37=f_4/(1-(f_1+f_3+f_5));
thita_37=thita_13;
xai_38=xai_14;
thita_39=f_3/(1-(f_1+f_5));
xai_39=xai_33;
sai_40=sai_34;
sai_41=f_1/(1-f_3);
thita_42=f_3/(1-f_1);
xai_43=f_5/(1-(f_1+f_3+f_4));
thita_43=thita_19;
beta_44=beta_20;
thita_45=f_3/(1-(f_1+f_4));
beta_45=beta_43;
sai_46=sai_41;
sai_47=sai_41;
thita_48=thita_42;
thita_49=f_3/(1-(f_1+f_2+f_4+f_5));
fai_49=f_2/(1-(f_4+f_5));
xai_49=xai_25;
beta_50=beta_26;
fai_51=f_2/(1-f_5);
xai_52=f_5/(1-f_2);
xai_53=f_5/(1-(f_2+f_4));
beta_53=beta_50;
fai_54=fai_22;
sai_55=sai_31;
xai_55=xai_31;
beta_56=beta_32;
sai_57=sai_33;
xai_58=xai_34;
xai_59=xai_35;
beta_59=beta_35;
sai_60=sai_36;
sai_61=f_1/(1-(f_2+f_5));
xai_61=xai_15;
fai_62=fai_16;
sai_63=sai_33;
xai_64=xai_34;
xai_19=f_5/(1-(f_2+f_3+f_4));
thita_19=thita_5;
beta_20=beta_6;
thita_21=f_3/(1-(f_2+f_4));
beta_21=beta_2;
fai_22=fai_10;
fai_23=fai_17;
thita_24=thita_18;
fai_25=f_2/(1-(f_1+f_3+f_4+f_5));
thita_25=thita_1;
xai_25=xai_1;
beta_26=beta_2;
thita_27=thita_3;
xai_28=xai_4;
xai_29=xai_5;
beta_29=beta_5;
thita_30=thita_6;
sai_31=f_1/(1-(f_4+f_5));
xai_31=xai_7;
beta_32=beta_8;
sai_33=f_1/(1-f_5);
xai_34=f_5/(1-f_1);
xai_35=f_5/(1-(f_1+f_4));
beta_35=beta_2;
sai_36=sai_34;
sai_37=f_1/(1-(f_3+f_5));
xai_37=xai_13;
thita_38=thita_14;
sai_39=sai_33;
xai_40=xai_34;
xai_41=f_5/(1-(f_1+f_3));
thita_41=thita_38;
sai_42=sai_34;
sai_43=f_1/(1-(f_3+f_4));
beta_43=beta_19;
thita_44=thita_20;
sai_45=f_1/(1-f_4);
beta_46=f_4/(1-f_1);
beta_47=f_4/(1-(f_1+f_3));
thita_47=thita_44;
sai_48=sai_34;
sai_49=f_1/(1-(f_2+f_4+f_5));
beta_49=beta_25;
xai_50=xai_26;
beta_51=f_4/(1-(f_2+f_5));
xai_51=xai_49;
fai_52=fai_18;
fai_53=f_2/(1-f_4);
beta_54=beta_22;
fai_55=f_2/(1-(f_1+f_4+f_5));
beta_55=beta_31;
xai_56=xai_32;
beta_57=beta_33;
xai_57=xai_33;
sai_58=sai_34;
sai_59=sai_35;
beta_60=beta_36;
beta_61=f_4/(1-(f_1+f_2+f_5));
fai_61=fai_15;
xai_62=xai_16;
fai_63=f_2/(1-(f_1+f_5));
xai_63=xai_33;
sai_64=sai_34;
```

```
xai_65=f_5/(1-(f_1+f_2));
fai_65=fai_16;
sai_66=sai_64;
sai_67=f_1/(1-(f_2+f_4));
beta_67=beta_21;
fai_68=fai_22;
sai_69=sai_45;
beta_70=beta_46;
beta_71=f_4/(1-(f_1+f_2));
fai_71=fai_65;
sai_72=sai_66;
sai_73=f_1/(1-(f_2+f_3+f_5));
thita_73=thita_13;
xai_74=xai_14;
thita_75=thita_15;
xai_75=xai_15;
fai_76=fai_16;
fai_77=fai_17;
thita_78=thita_18;
fai_79=f_2/(1-(f_1+f_3+f_5));
thita_79=thita_37;
xai_80=xai_38;
thita_81=thita_39;
xai_81=xai_39;
sai_82=sai_40;
sai_83=sai_41;
thita_84=thita_42;
thita_85=f_3/(1-(f_1+f_2+f_5));
fai_85=fai_15;
xai_86=xai_16;
fai_87=f_2/(1-(f_1+f_5));
xai_87=xai_33;
sai_88=sai_34;
sai_89=f_1/(1-f_2);
fai_90=fai_66;
xai_91=f_5/(1-(f_1+f_2+f_3));
fai_91=fai_17;
thita_92=thita_18;
fai_93=f_2/(1-(f_1+f_3));
thita_93=thita_41;
sai_94=sai_42;
sai_95=sai_65;
fai_96=fai_66;
xai_97=f_5/(1-(f_1+f_2+f_3+f_4));
fai_97=fai_19;
beta_97=beta_19;
thita_98=thita_20;
fai_99=fai_21;
beta_100=beta_22;
beta_101=beta_23;
thita_101=thita_23;
fai_102=fai_18;
sai_103=sai_43;
beta_103=beta_43;
thita_104=thita_44;
sai_105=sai_45;
beta_106=beta_46;
beta_107=beta_47;
thita_107=thita_47;
sai_108=sai_48;
sai_109=sai_67;
beta_109=beta_67;
fai_110=fai_68;
```

```
sai_65=f_1/(1-f_2);
fai_66=f_2/(1-f_1);
xai_67=f_5/(1-(f_1+f_2+f_4));
fai_67=fai_21;
beta_68=beta_22;
fai_69=f_2/(1-(f_1+f_4));
beta_69=beta_45;
sai_70=sai_46;
sai_71=f_1/(1-f_2);
fai_72=fai_66;
beta_73=f_4/(1-(f_1+f_2+f_3+f_5));
fai_73=fai_13;
xai_73=xai_13;
thita_74=thita_14;
fai_75=fai_15;
xai_76=xai_16;
xai_77=xai_17;
thita_77=thita_17;
fai_78=fai_18;
sai_79=sai_37;
xai_79=xai_37;
thita_80=thita_38;
sai_81=sai_39;
xai_82=xai_40;
xai_83=xai_41;
thita_83=thita_41;
sai_84=sai_42;
sai_85=f_1/(1-(f_2+f_5));
xai_85=xai_15;
fai_86=fai_16;
sai_87=sai_33;
xai_88=xai_34;
xai_89=f_5/(1-(f_1+f_2));
fai_89=fai_16;
sai_90=sai_66;
sai_91=f_1/(1-(f_2+f_3));
thita_91=thita_17;
fai_92=fai_18;
sai_93=sai_41;
thita_94=thita_42;
thita_95=f_3/(1-(f_1+f_2));
fai_95=fai_65;
sai_96=sai_66;
sai_97=f_1/(1-(f_2+f_3+f_4));
thita_97=thita_19;
beta_98=beta_20;
thita_99=thita_21;
beta_99=beta_21;
fai_100=fai_22;
fai_101=fai_23;
thita_102=thita_18;
fai_103=f_2/(1-(f_1+f_3+f_4));
thita_103=thita_43;
beta_104=beta_44;
thita_105=thita_45;
beta_105=beta_45;
sai_106=sai_46;
sai_107=sai_47;
thita_108=thita_48;
thita_109=f_3/(1-(f_1+f_2+f_4));
fai_109=fai_67;
beta_110=beta_68;
fai_111=fai_69;
```

```
sai_111=sai_69;                    beta_111=beta_69;
beta_112=beta_70;                  sai_112=sai_70;
beta_113=beta_71;                  sai_113=sai_71;
fai_113=fai_71;                    fai_114=fai_72;
sai_114=sai_72;                    beta_115=f_4/(1-(f_1+f_2+f_3));
sai_115=sai_91;                    fai_115=fai_91;
thita_115=thita_91;                thita_116=thita_92;
fai_116=fai_92;                    fai_117=fai_93;
sai_117=sai_93;                    thita_117=thita_93;
thita_118=thita_94;                sai_118=sai_94;
thita_119=thita_95;                sai_119=sai_95;
fai_119=fai_95;                    fai_120=fai_96;          sai_120=sai_96;

A=((1-sai_1)^X1*((1-fai_1)^X2*((1-thita_1)^X3*((1-beta_1)^X4*(1-xai_1)^X5+(1-
xai_2)^X5*(1-beta_2)^X4)+(1-beta_3)^X4*((1-thita_3)^X3*(1-xai_3)^X5+(1-xai_4)^X5*(1-
thita_4)^X3)+(1-xai_5)^X5*((1-thita_5)^X3*(1-beta_5)^X4+(1-beta_6)^X4*(1-
thita_6)^X3))+(1-thita_7)^X3*((1-fai_7)^X2*((1-beta_7)^X4*(1-xai_7)^X5+(1-
xai_8)^X5*(1-beta_8)^X4)+(1-beta_9)^X4*((1-fai_9)^X2*(1-xai_9)^X5+(1-xai_10)^X5*(1-
fai_10)^X2)+(1-xai_11)^X5*((1-fai_11)^X2*(1-beta_11)^X4+(1-beta_12)^X4*(1-
fai_12)^X2))+(1-beta_13)^X4*((1-fai_13)^X2*((1-thita_13)^X3*(1-xai_13)^X5+(1-
xai_14)^X5*(1-thita_14)^X3)+(1-thita_15)^X3*((1-fai_15)^X2*(1-xai_15)^X5+(1-
xai_16)^X5*(1-fai_16)^X2)+(1-xai_17)^X5*((1-fai_17)^X2*(1-thita_17)^X3+(1-
thita_18)^X3*(1-fai_18)^X2))+(1-xai_19)^X5*((1-fai_19)^X2*((1-thita_19)^X3*(1-
beta_19)^X4+(1-beta_20)^X4*(1-thita_20)^X3)+(1-thita_21)^X3*((1-fai_21)^X2*(1-
beta_21)^X4+(1-beta_22)^X4*(1-fai_22)^X2)+(1-beta_23)^X4*((1-fai_23)^X2*(1-
thita_23)^X3+(1-thita_24)^X3*(1-fai_24)^X2))));

B=((1-fai_25)^X2*((1-sai_25)^X1*((1-thita_25)^X3*((1-beta_25)^X4*(1-xai_25)^X5+(1-
xai_26)^X5*(1-beta_26)^X4)+(1-beta_27)^X4*((1-thita_27)^X3*(1-xai_27)^X5+(1-
xai_28)^X5*(1-thita_28)^X3)+(1-xai_29)^X5*((1-thita_29)^X3*(1-beta_29)^X4+(1-
beta_30)^X4*(1-thita_30)^X3))+(1-thita_31)^X3*((1-sai_31)^X1*((1-beta_31)^X4*(1-
xai_31)^X5+(1-xai_32)^X5*(1-beta_32)^X4)+(1-beta_33)^X4*((1-sai_33)^X1*(1-
xai_33)^X5+(1-xai_34)^X5*(1-sai_34)^X1)+(1-xai_35)^X5*((1-sai_35)^X1*(1-
beta_35)^X4+(1-beta_36)^X4*(1-sai_36)^X1))+(1-beta_37)^X4*((1-sai_37)^X1*((1-
thita_37)^X3*(1-xai_37)^X5+(1-xai_38)^X5*(1-thita_38)^X3)+(1-thita_39)^X3*((1-
sai_39)^X1*(1-xai_39)^X5+(1-xai_40)^X5*(1-sai_40)^X1)+(1-xai_41)^X5*((1-sai_41)^X1*(1-
thita_41)^X3+(1-thita_42)^X3*(1-sai_42)^X1))+(1-xai_43)^X5*((1-sai_43)^X1*((1-
thita_43)^X3*(1-beta_43)^X4+(1-beta_44)^X4*(1-thita_44)^X3)+(1-thita_45)^X3*((1-
sai_45)^X1*(1-beta_45)^X4+(1-beta_46)^X4*(1-sai_46)^X1)+(1-beta_47)^X4*((1-
sai_47)^X1*(1-thita_47)^X3+(1-thita_48)^X3*(1-sai_48)^X1))));

C=((1-thita_49)^X3*((1-sai_49)^X1*((1-fai_49)^X2*((1-beta_49)^X4*(1-xai_49)^X5+(1-
xai_50)^X5*(1-beta_50)^X4)+(1-beta_51)^X4*((1-fai_51)^X2*(1-xai_51)^X5+(1-
xai_52)^X5*(1-fai_52)^X2)+(1-xai_53)^X5*((1-fai_53)^X2*(1-beta_53)^X4+(1-
beta_54)^X4*(1-fai_54)^X2))+(1-fai_55)^X2*((1-sai_55)^X1*((1-beta_55)^X4*(1-
xai_55)^X5+(1-xai_56)^X5*(1-beta_56)^X4)+(1-beta_57)^X4*((1-sai_57)^X1*(1-
xai_57)^X5+(1-xai_58)^X5*(1-sai_58)^X1)+(1-xai_59)^X5*((1-sai_59)^X1*(1-
beta_59)^X4+(1-beta_60)^X4*(1-sai_60)^X1))+(1-beta_61)^X4*((1-sai_61)^X1*((1-
fai_61)^X2*(1-xai_61)^X5+(1-xai_62)^X5*(1-fai_62)^X2)+(1-fai_63)^X2*((1-sai_63)^X1*(1-
xai_63)^X5+(1-xai_64)^X5*(1-sai_64)^X1)+(1-xai_65)^X5*((1-sai_65)^X1*(1-fai_65)^X2+(1-
fai_66)^X2*(1-sai_66)^X1))+(1-xai_67)^X5*((1-sai_67)^X1*((1-fai_67)^X2*(1-
beta_67)^X4+(1-beta_68)^X4*(1-fai_68)^X2)+(1-fai_69)^X2*((1-sai_69)^X1*(1-
beta_69)^X4+(1-beta_70)^X4*(1-sai_70)^X1)+(1-beta_71)^X4*((1-sai_71)^X1*(1-
fai_71)^X2+(1-fai_72)^X2*(1-sai_72)^X1))));

D=((1-beta_73)^X4*((1-sai_73)^X1*((1-fai_73)^X2*((1-thita_73)^X3*(1-xai_73)^X5+(1-
xai_74)^X5*(1-thita_74)^X3)+(1-thita_75)^X3*((1-fai_75)^X2*(1-xai_75)^X5+(1-
xai_76)^X5*(1-fai_76)^X2)+(1-xai_77)^X5*((1-fai_77)^X2*(1-thita_77)^X3+(1-
thita_78)^X3*(1-fai_78)^X2))+(1-fai_79)^X2*((1-sai_79)^X1*((1-thita_79)^X3*(1-
xai_79)^X5+(1-xai_80)^X5*(1-thita_80)^X3)+(1-thita_81)^X3*((1-sai_81)^X1*(1-
xai_81)^X5+(1-xai_82)^X5*(1-sai_82)^X1)+(1-xai_83)^X5*((1-sai_83)^X1*(1-
thita_83)^X3+(1-thita_84)^X3*(1-sai_84)^X1))+(1-thita_85)^X3*((1-sai_85)^X1*((1-
fai_85)^X2*(1-xai_85)^X5+(1-xai_86)^X5*(1-fai_86)^X2)+(1-fai_87)^X2*((1-sai_87)^X1*(1-
```

```
xai_87)^X5+(1-xai_88)^X5*(1-sai_88)^X1)+(1-xai_89)^X5*((1-sai_89)^X1*(1-fai_89)^X2+(1-
fai_90)^X2*(1-sai_90)^X1))+(1-xai_91)^X5*((1-sai_91)^X1*((1-fai_91)^X2*(1-
thita_91)^X3+(1-thita_92)^X3*(1-fai_92)^X2)+(1-fai_93)^X2*((1-sai_93)^X1*(1-
thita_93)^X3+(1-thita_94)^X3*(1-sai_94)^X1)+(1-thita_95)^X3*((1-sai_95)^X1*(1-
fai_95)^X2+(1-fai_96)^X2*(1-sai_96)^X1))));

E=((1-xai_97)^X5*((1-sai_97)^X1*((1-fai_97)^X2*((1-thita_97)^X3*(1-beta_97)^X4+(1-
beta_98)^X4*(1-thita_98)^X3)+(1-thita_99)^X3*((1-fai_99)^X2*(1-beta_99)^X4+(1-
beta_100)^X4*(1-fai_100)^X2)+(1-beta_101)^X4*((1-fai_101)^X2*(1-thita_101)^X3+(1-
thita_102)^X3*(1-fai_102)^X2))+(1-fai_103)^X2*((1-sai_103)^X1*((1-thita_103)^X3*(1-
beta_103)^X4+(1-beta_104)^X4*(1-thita_104)^X3)+(1-thita_105)^X3*((1-sai_105)^X1*(1-
beta_105)^X4+(1-beta_106)^X4*(1-sai_106)^X1)+(1-beta_107)^X4*((1-sai_107)^X1*(1-
thita_107)^X3+(1-thita_108)^X3*(1-sai_108)^X1))+(1-thita_109)^X3*((1-sai_109)^X1*((1-
fai_109)^X2*(1-beta_109)^X4+(1-beta_110)^X4*(1-fai_110)^X2)+(1-fai_111)^X2*((1-
sai_111)^X1*(1-beta_111)^X4+(1-beta_112)^X4*(1-sai_112)^X1)+(1-beta_113)^X4*((1-
sai_113)^X1*(1-fai_113)^X2+(1-fai_114)^X2*(1-sai_114)^X1))+(1-beta_115)^X4*((1-
sai_115)^X1*((1-fai_115)^X2*(1-thita_115)^X3+(1-thita_116)^X3*(1-fai_116)^X2)+(1-
fai_117)^X2*((1-sai_117)^X1*(1-thita_117)^X3+(1-thita_118)^X3*(1-sai_118)^X1)+(1-
thita_119)^X3*((1-sai_119)^X1*(1-fai_119)^X2+(1-fai_120)^X2*(1-sai_120)^X1))));

k=(k_o./120).*(A+B+C+D+E);
```